MICROFLUIDIC CHIP CALORIMETERS FOR BIOLOGICAL APPLICATIONS

Thesis by

Wonhee Lee

In Partial Fulfillment of the Requirements

for the Degree of

Doctor of Philosophy

California Institute of Technology

Pasadena, California

2008

(Defended May 19, 2008)

Acknowledgement

“The truth will set you free” John 8:32

Since I have entered an elementary school, it took 20 yeas to get my Ph.D.! While I was preparing the thesis, I could not help asking myself what I have learned in these so many years. After I spent some time recalling the past years, I realized that all the experience I went through have their meanings more than a doctor degree and I am under the process of learning. The life itself is indeed a school to find the truth.

One of the lessons, I have learned during my graduate school time is that the most important asset in life is people. I had so many people supporting me all the time. I would like to acknowledge all the people helping me in many ways.

First of all, I thank my advisor, Dr. Michael Roukes, for all the support and guide throughout the years. I thank to the committee members, Dr. Chin-Lin Guo, Dr. Michael Elowitz, and Dr. Rob Phillips. Also, I want to thank Dr. Fon and other group members for the helps and advices.

Words cannot describe my appreciation to my wife, Jina. Without her support I would not be able to go through all the hardships. I thank my beloved parents, family and relatives for all the support and prayers. Lastly, I want to thank all my friends for their help and encouragement.

Abstract

The usage of calorimeters is limited due to its long measurement time and large sample consumption, despite its many advantages including universal applicability and simple sample preparation. Miniaturization of calorimeters not only resolves these problems, it also enables high-throughput measurements with array operations. We have developed microfluidic chip calorimeters with high sensitivity and reliable microfluidics-based sample handling. Immense sensitivity improvements are attained through reduction of the thermal conductance via on-chip vacuum insulation. This is enabled by Parylene thin film microfluidic systems. Polydimethylsiloxane microfluidic systems, combined with the Parylene microfluidic system, gives easy and accurate control of picoliter-scale sample volume in a manner that is easily scalable to large, complex systems. Two device classes have been realized.

Heat conduction calorimeters for biochemical reactions with 3.5 nL sample volume were built and validated by measurements of the heat of mixing and of enzyme activity. The thermal conductance of these devices was 15.5 μW/K and their power sensitivity was 4.2 nW. These devices can be built as calorimetric arrays to enable high-throughput heat of reaction measurements upon libraries of biomolecular interactions.

Flow calorimeters were designed for sensor applications and measurements of cellular metabolism. The thermal conductance of these devices was 4.7 μW/K and their power sensitivity was 1.5 nW. Further reduction of thermal conductance and optimal thermocouple materials will deliver sensitivity of order ~1 pW, which will enable real time measurement of single cell metabolism.

Table of Contents

List of Figures

Chapter 1

Chapter 2

Chapter 3

Chapter 4

List of Tables

Chapter 1

Chapter 2

Chapter 3

Chapter 4

Chapter 1

Introduction

1.1 Introduction

In last two decades there has been remarkable growth in biosensor research. Thousands of research papers related to biosensors are published every year and the number of patents is increasing rapidly. Even faster growth of the field is envisaged, yet there are many scientific challenges and practical issues for biosensor development. This fast growth has been accelerated by several driving forces, especially by the adoption of microfabrication technology to miniaturize biosensors. This delivers many benefits such as high-throughput measurement, integration of multiple-step analysis, improved sensitivity, and low product cost.

In this work we focused our attention upon calorimetric biosensors because they have a number of advantages over other types of biosensors; including universal applicability, complete thermodynamic characterization of reaction, and sample

preparation without labeling or immobilization. Miniaturization of calorimeter can resolve the main drawbacks of conventional calorimetric biosensors which include long measurement time and large sample consumption. Furthermore, miniaturized calorimeters have great potential for analysis of single cell metabolism in real-time. The object of this research project is to develop miniaturized calorimeters with improved sensitivity and precise fluidic control so as to overcome the limitations of macroscale calorimetry.

1.2 Biosensors

A biosensor is an analytical device that combines a biological component with a physicochemical detector component (Figure 1-1).

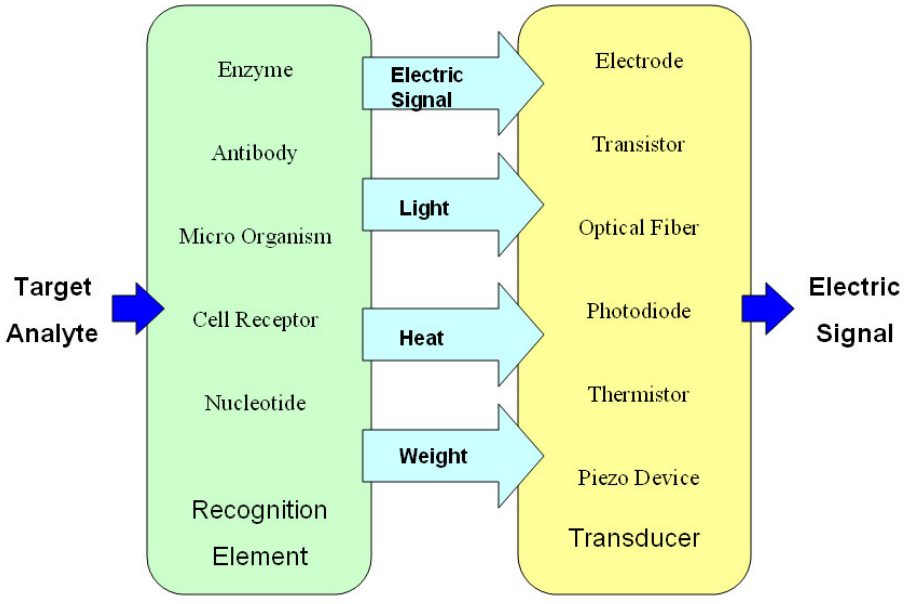

Figure 1-1. Principle of biosensors.

Biosensors consist of two components; “recognition elements” respond to the target analyte selectively to generate physical signal and “transducers” transform the signal to electric signal for readout.

1.2.1 Recognition Elements

The recognition elements of biosensors are a very important component because they determine the selectivity of the biosensors. The selectivity is realized by specific binding of biomolecules (e.g., antibody to antigen and between DNA base pairs) and enzymes that are typically immobilized on the sensor surface. Recognition elements should respond to the target analyte without interference with the other analyte and should be compatible with the selected modes of transduction.

Recognition elements can be used to provide a classification scheme for biosensors [1]. Figure 1-2 shows the major categories of recognition elements.

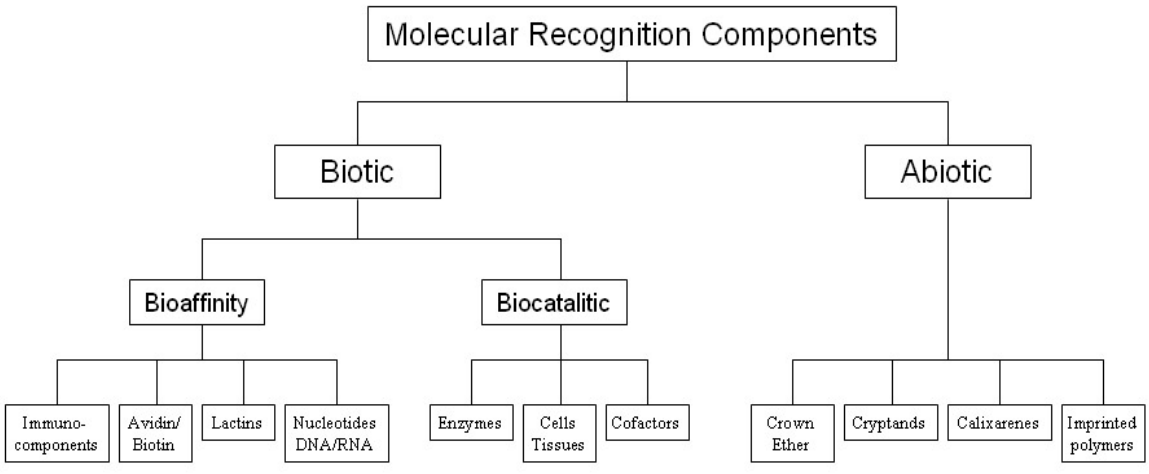

Figure 1-2. Approaches to molecular recognition [1].

According to the definition, biosensors do not involve abiotic recognition elements. However, in broader sense, sensors with abiotic materials (biomimics) designed for biomolecular recognition can be put in the biosensor category.

1.2.2 Transducers

Transducer and sensor are sometimes used as synonyms. In this thesis, we make careful distinction between the two. By *transducers* we refer to devices that convert one form of energy into another, thus providing the user with usable energy output in response to specific measurable input. For example, a thermistor is a transducer that converts thermal energy to electrical energy. On the other hand, by *sensors* we refer to a combination of recognition elements *and* transducers. For example, a calorimeter is a sensor with a thermal mass (recognition element) and a thermometer (transducer). The enzyme thermistor is a good example of a calorimetric biosensor; it uses an enzyme as a biocatalitic recognition element [2].

Transducers can be classified into four categories according to the energy transduction mode: electrochemical transducers, optical transducers, thermal transducers, and mass sensitive transducers. Detailed descriptions of these transduction modes can be found in many books and reviews [1, 3-12]. Extended categories within the each major category are listed in Table 1-1 [1]. These many, yet not complete, categories illustrate the diversity of the transduction modes.

Table 1-1. Extended categories of transduction modes [1]

Eletrochemical	**Thermal**
Amperometric	Adiabatic
Conductimetric	Heat conduction
Impedimetric	
Potentiometric	**Mass sensitive**
	Acoustic plate mode
Optical	Flexural plate mode
Absorbance	Surface acoustic wave
Chemiluminescence	Surface transverse wave
Electro generated chemiluminiscence	Thickness shear mode
Fluorescence	
Fluorescence lifetime	**Other**
Fiber optic waveguide	Biomagnetic
Near-fild microscopy and spectroscopy	Light addressable potentiometric
Near-infrared	Scanning electrochemical microscopy
Planar wave guide	Separation/detection system
Surface enhanced Raman	
Surface plasmon resonance	

The advantages and disadvantages of the four major transduction modes are summarized in Table 1-2. Some transduction modes are more sensitive than others and some modes have better selectivity than others. No transduction mode is superior in every point of view. The design of the biosensors is necessarily based upon its purpose; among critical points to be considered are target analyte, environment, sensitivity, selectivity, dynamic range, etc.

Table 1-2. Comparison of transduction modes

	Advantages	Disadvantages
Electrochemical	Easy to fabricate	Potentiometric: pH sensitive Amperometric: requires reference Screening in conducting solutions
Optical	Diversity on detection mode In vivo application High sensitivity	Problems from ambient light and scattering Limited dynamic range
Thermal	General applicability Simple procedure	Low sensitivity Slow response
Mass sensitive	High sensitivity	Large damping in liquid

The technology for engineering recognition elements and transducers encompasses a very diverse realm of science and engineering. Accordingly, successful development of biosensors requires broad knowledge of interdisciplinary subjects and cooperation between specialists in many different fields.

1.2.3 Miniaturization of Biosensors

Miniaturization is one of the important directions in biosensor research. Miniaturized biosensors have many advantages over conventional biosensors. First of all, miniaturized biosensors can be built as sensor arrays to improve the sensor performance. Array operation can give enhanced selectivity through: “orthogonal” sensing for the same analyte, expanded dynamic range by combining sensors working in different sensitivity

regimes, and improved signal-to-noise (S/N) ratio ideally $\sim\sqrt{n}$ times improvement in S/N with n identical sensors [13]. Most importantly, array operation enables high-throughput measurements by fast response and massively parallel measurements. Second, miniaturization of biosensors reduces the consumption of sample and production of waste. High-throughput and low consumption of sample are crucial factors to reduces the time and cost of assays, especially for the pharmaceutical industry [8, 14]. Third, the cost of sensor manufacturing can be reduced dramatically. Because miniaturized sensors have similar fabrication processes as microelectronic devices, mass production becomes possible. In many cases, the final sensor products can be disposable, which is especially attractive for clinical use. Mass production also gives fast design cycles. Fourth, miniaturized sensors can be built as hand-held devices, thus they can be used in environments where larger equipment cannot be used. Finally, miniaturization extends the opportunity for integration of diverse sensors onto a single chip to build what have been called “lab-on-a-chip” or “micro- Total Analysis Systems” (μ-TAS) [15-17].

Miniaturization does have some disadvantages, however, not to mention technical challenges. First of all, miniaturized biosensors will not work as well as conventional biosensors if the sensitivity does not scale upward as sample volume. To have benefit from reduced sample volume, miniaturized biosensors must detect the analyte with the same level of concentration as the conventional biosensors. However, sensor response usually decreases with smaller sample volume and the response time increases with smaller sensing area. In some cases, scarcity of sample simply will not allow the scaling downward of volume past certain volume. For example, numerous biomolecules are present at concentration of less than 100 copies/mL in blood sample [18]. At this

concentration, the sample of 1 µL has ~10% chance of containing a single target. (Figure 1-3). Beyond the associated sensitivity and detectability issues, when the sample size is small, obtaining a representative sample for inhomogeneous media containing diversity of constituents is difficult.

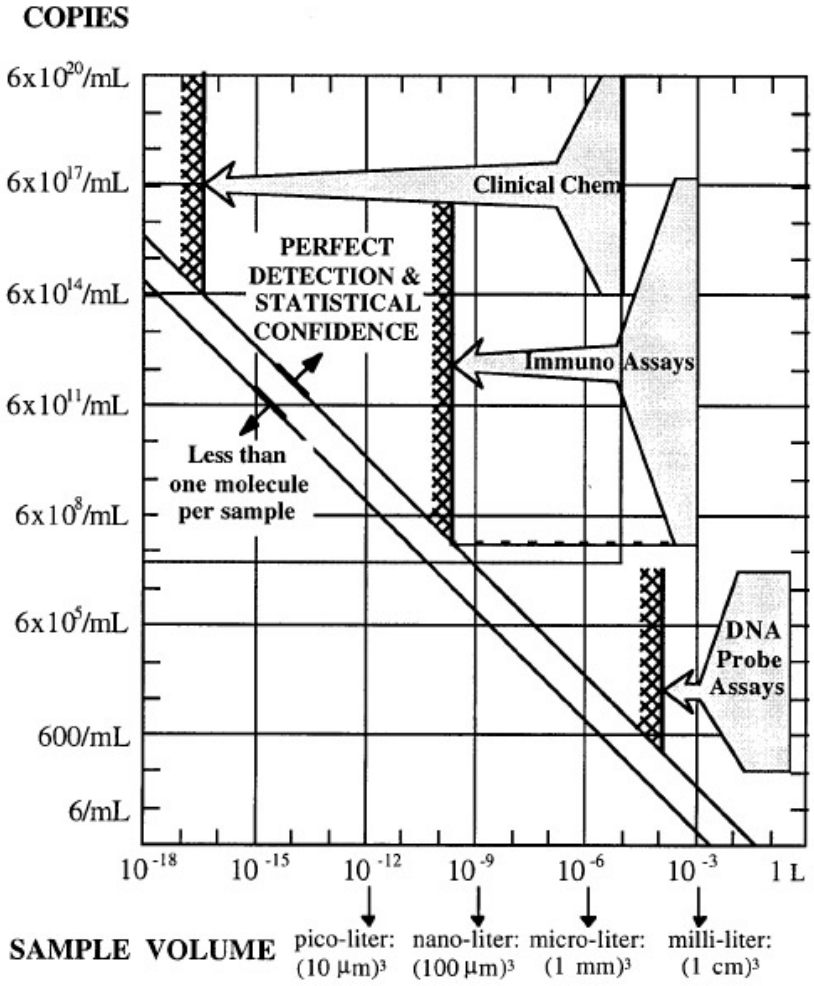

Figure 1-3. Scaling of concentration and sample volume [18].

1.3 Calorimeters

A calorimeter is a device for measuring the heat developed during a mechanical, electrical, or chemical reaction, and for calculating the heat capacity of materials [19]. Calorimeters have a very old history. In 1760 the first calorimeter appeared in the history by Joseph Black. But, his findings were reported only verbally and the first calorimeter reported in the literature was built by Lavoisier and Laplace in 1783. Both calorimeters measured the amount of heat from the amount of melting ice (Figure 1-4). Since then, numerous types of calorimeters are developed and used in various fields to reveal thermodynamic properties of the subject.

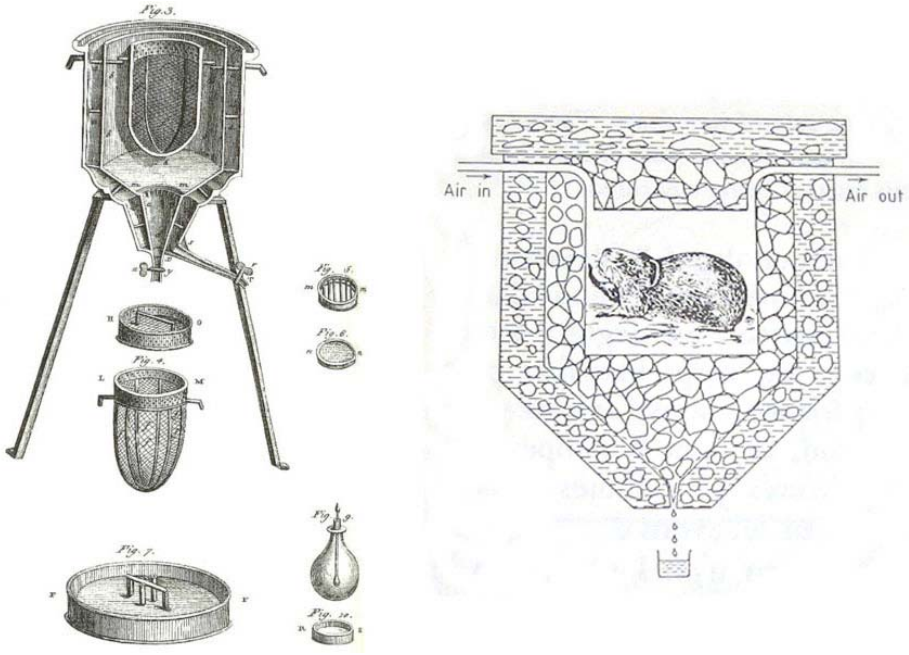

Figure 1-4. Ice calorimeter of Lavoisier and Laplace (left) and the schematic design (right).

A typical calorimeter consists of one (or two) insulated calorimetric chamber(s) and electronics for the thermal sensing. The heat evolved or absorbed in the calorimetric

chamber (also called the cell or vessel) is evaluated by measuring the temperature change or the amount of power to compensate the change. The chamber is isolated from the surroundings (also called the environments) physically and thermally to prevent interference and heat loss. One example of such calorimeter is shown in Figure 1-5.

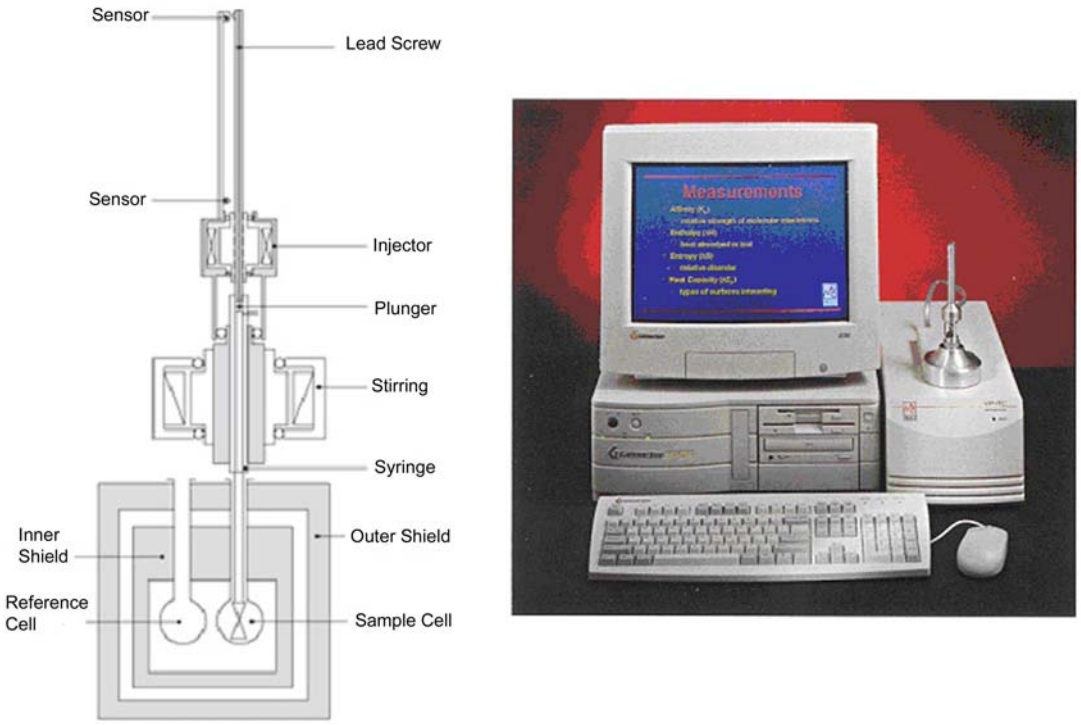

Figure 1-5. Commercial calorimeter. VP-ITC, Microcal.

1.3.1 Theoretical Background

A calorimeter can be described as an object with integral heat sources. To understand the system, we need to understand heat transfer and the theory of calorimetry.

In this section we discuss heat transfer theory and use some of basic equations to derive general equations representing a mathematical model of a calorimeter [20, 21].

There are three important heat transfer phenomena associated with spatiotemporal temperature differences: conduction, convection and radiation. Heat conduction is the exchange of heat by transport of vibrational states (phonon) without any mass flow. Heat conduction can be described by the Fourier Law

$$\vec{q} = -\lambda \nabla T \tag{1.1}$$

where λ is thermal conductivity and $\vec{q}$ is heat flux. This equation basically tells us that the heat flux is proportional to the temperature gradient. With this simple form, we treat the object as homogeneous and isotropic body. More generally, λ depends on direction inside of the solid body and the temperature and, in that case, λ becomes a tensor.

The heat flux is a rate of heat (Q) transferred through unit surface ($d\vec{S}$) per unit time (dt).

$$\vec{q} = \frac{d}{d\vec{S}}\left(\frac{dQ}{dt}\right) \tag{1.2}$$

When heat is generated in a body, two processes occur. Heat can accumulate (dQ_1) or be transferred (dQ_1) to environment.

$$dQ = dQ_1 + dQ_2 \tag{1.3}$$

Considering a surface element S with volume V,

$$dQ_2 = \iint_S \vec{q} \cdot d\vec{S} dt = \iiint_V \nabla \cdot \vec{q} dV dt \tag{1.4}$$

$$dQ = \iiint_V g dV dt \tag{1.5}$$

Here, g is density of the heat source.

Combining Equations (1.3), (1.4), and (1.5) we get

$$dQ_1 = \iiint_V (g - \nabla \cdot \vec{q}) dV dt \tag{1.6}$$

According to the First Law of Thermodynamics,

$$dQ_1 = dh - V dP \tag{1.7}$$

Integrating over V,

$$dQ_1 = \iiint_V dh dV - \iiint_V dp dV \tag{1.8}$$

Comparison of both sides of Equations (1.6) and (1.8) gives,

$$g - \nabla \cdot \vec{q} = \frac{dh}{dt} - \frac{dp}{dt} \tag{1.9}$$

Because,

$$dh = c_P \rho \; dT \tag{1.10}$$

$$c_P \rho \frac{dT}{dt} - \frac{dp}{dt} = g + \nabla \cdot (\lambda \nabla T) \tag{1.11}$$

With introduction of velocity vector $\vec{w}$

$$\vec{w} = \left[\frac{\partial x}{\partial t}, \frac{\partial y}{\partial t}, \frac{\partial z}{\partial t} \right] \tag{1.12}$$

$$dT = \frac{\partial T}{\partial x} dx + \frac{\partial T}{\partial y} dy + \frac{\partial T}{\partial z} dz + \frac{\partial T}{\partial t} dt = \left(\vec{w} \cdot \nabla T + \frac{\partial T}{\partial t} \right) dt \tag{1.13}$$

In the same way,

$$dp = \left(\vec{w} \cdot \nabla p + \frac{\partial p}{\partial t} \right) dt \tag{1.14}$$

Putting Equation (1.13) and (1.14) into Equation (1.11), we get the Fourier-Kirchhoff equation,

$$c_P \rho \left(\vec{w} \cdot \nabla T + \frac{\partial T}{\partial t} \right) = g + \lambda \nabla^2 T + \vec{w} \cdot \nabla p + \frac{\partial p}{\partial t} \tag{1.15}$$

When we have isobaric conditions and the velocity vector is equal to zero, i.e.

$$\frac{\partial p}{\partial t} = 0 \, , \nabla p = 0 \text{ and } \vec{w} = \vec{0} \tag{1.16}$$

Equation becomes the equation of conduction of heat,

$$c_P \rho \frac{\partial T}{\partial t} = g + \lambda \nabla^2 T \tag{1.17}$$

This equation is also called the Fourier equation.

Unlike conduction, convection involves actual flow of mass, along with heat. Heat is transferred by flow of media moving from hotter site to colder site. Convection can be described by the Newton's law of cooling,

$$q_v = b(T_S - T_0) \tag{1.18}$$

where b is coefficient of convection heat transfer, T_S is temperature of a solid and T_S is temperature of a fluid. For a good calorimetric measurement, heat transfer by convection needs to be eliminated, which typically is achieved by evacuation the sample's surroundings.

Radiation is the transfer of heat in the form of electromagnetic waves. All physical objects emit energy through radiation and, at the same time, absorb energy in the form of radiation. Radiation can be described by an equation,

$$q_r = \varepsilon_m \cdot \sigma_B (T_S^4 - T_0^4) \tag{1.19}$$

where ε_m is emmisivity and σ_B is the Stefan-Boltzmann constant.

With this preface we will now construct a mathematical model of a calorimeter. Let us consider a heat transfer process without mass transfer. We will assume an isobaric condition and thermal parameters are constant. Then the Fourier-Kirchhoff equation can be written as

$$\frac{\partial T}{\partial t} = a\nabla^2 T + \frac{g}{c_P \rho} \tag{1.20}$$

where $a = \frac{\lambda}{c_P \rho}$ is thermal diffusivity.

Integrating Equation (1.20) over the body of volume V and surface S,

$$\iiint_V \frac{\partial T}{\partial t} dV = \iiint_V a\nabla^2 T dV + \iiint_V \frac{g}{c_P \rho} dV \tag{1.21}$$

The left-hand side of Equation (1.21) can be rewritten as

$$\iiint_V \frac{\partial T}{\partial t} dV = \frac{d}{dt} \iiint_V T dV = V \frac{dT_V}{dt} \tag{1.22}$$

where

$$T_V = \frac{1}{V} \iiint_V T dV \tag{1.23}$$

is the average temperature of the body.

The first term on right-hand side of Equation (1.21) can be rewritten using Equation (1.1);

$$\iiint_V a\nabla^2 T dV = \frac{\lambda}{c_P \rho} \iint_S \nabla T \cdot d\vec{S} = -\frac{1}{c_P \rho} \iint_S \vec{q} \cdot d\vec{S} = -\frac{1}{c_P \rho} q_S S \tag{1.24}$$

where

$$q_S = \frac{1}{S} \iint_S \vec{q} \cdot d\vec{S} \tag{1.25}$$

is the average heat flux across the surface of the body.

The heat flux, q_S, can be expressed using the Newton's law of cooling:

$$q_S = \alpha[T_S - T_0] \tag{1.26}$$

where T_S is the average temperature of the surface of the body, T_0 is the temperature of the environment and α is the heat transfer coefficient.

The second term on the right-hand side of Equation (1.21) can be integrated to give

$$\iiint_V g dV = \frac{dQ}{dt} \tag{1.27}$$

Substitution of Equation (1.23), (1.24), (1.26) and (1.27) into Equation (1.21) yields

$$c_P \rho V \frac{dT_V}{dt} + S\alpha[T_S - T_0] = \frac{dQ}{dt} \tag{1.28}$$

If we assume the surface and the body has the same temperature,

$$C\frac{dT(t)}{dt} + G[T(t) - T_0(t)] = \frac{dQ(t)}{dt} \tag{1.29}$$

where

$$C = c_P \rho V \tag{1.30}$$

is the total heat capacity of the body and

$$G = \alpha S \tag{1.31}$$

is the heat loss coefficient between the body and the environment. If radiation and convection are ignored, which can be true in many cases, it becomes thermal conductance. Replacement of "*T(t)*" in the places of "*T*" are made to emphasize temperature is a function of time, while *C* and *G* are constant. Equation (1.29) is the heat balance equation of a simple body, and is the equation describing a calorimeter in general.

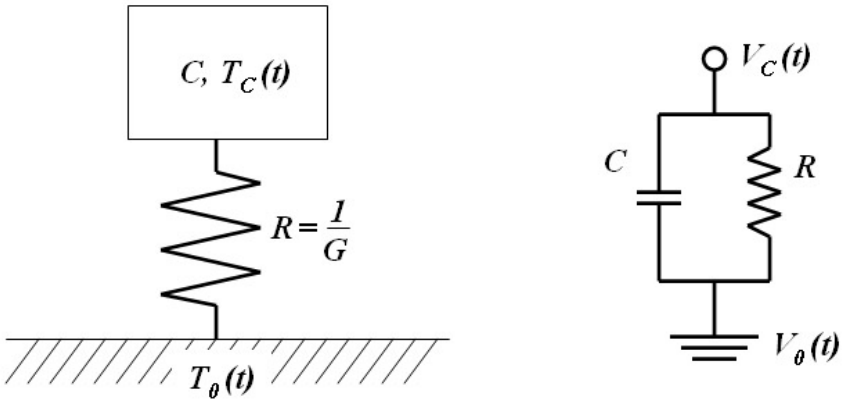

$$C\frac{df_C(t)}{dt} + G\left(f_C(t) - f_0(t)\right) = \frac{dQ}{dt}$$

Figure 1-6. Thermal diagram of a calorimeter (left) and electric circuit equivalent (right).

Heat transfer in a calorimeter can be compared with charge transport in an electric circuit with resistors and capacitors. Figure 1-6 shows the thermal diagram of a calorimeter and the electric circuit equivalent.

1.3.2 Classification of Calorimeters

As there are many types of calorimeters, there are many ways to classify them. Though there may be other criteria, calorimeters can be classified in general (1) by the measuring principle, (2) by mode of operation and (3) by construction principle [21].

According to the measuring principle, calorimeters can be divided into four categories.

i. Compensation of thermal effect by a phase transition: the measurement of the heat introduced into the calorimeter is done by measuring the amount of substance that

undergoes through a phase transition. Examples of this type of calorimeters are Lavoisier's Ice calorimeter and Bunsen's Vapor calorimeter.

ii. Compensation of thermal effect by a thermoelectric effect: the temperature of the calorimetric chamber is maintained at constant temperature by electric heating. Change in the electric power input represents the heat generated inside the calorimeter. Isothermal titration calorimeter (ITC) is one of the examples in this category.

iii. Measurement of a time-dependent temperature difference: the amount of heat is determined by measuring temperature change on calorimeter substance with known heat capacity. Isoperibol Titration Calorimeter is one of the examples.

iv. Measurement of a local temperature difference: the amount of heat is determined by measuring local temperature difference with known calibration factor. Heat conduction calorimeter and flow calorimeter are examples of this approach.

According to the modes of operation, calorimeters can be divided into six categories. The first three involve static operation and the latter three involve dynamic operation.

i. Isothermal operation: the temperature of the chamber and the surrounding are the same and constant.

ii. Adiabatic operation: no heat exchange occurs between the chamber and the surrounding.

iii: Isoperibol operation: the temperature of the surrounding is constant while the chamber temperature changes.

iv: Scanning of surroundings: heat is applied to surroundings to raise the temperature. The chamber temperature will rise with a time lag.

v: Adiabatic scanning: the chamber and the surrounding are heated separately in the manner so that their temperatures are always equal.

vi: Isoperibol scanning: the chamber is heated while the surrounding is maintained at constant temperature.

Classification according to construction principle has two categories.

i: Twin calorimeters: difference measurements are made between two chambers, identical in all respects except that only one contains the analyte.

ii: Single calorimeters: a single chamber is used for the measurement, and the properties of the system are carefully calibrated.

1.3.3 Chip Calorimeters

Development of the high throughput calorimeter will have significant impact beyond basic research. For example, its applications within the pharmaceutical industry will result in reducing costs and the time involved in the drug discovery process [22]. These are among the reasons that motivate the development of chip calorimeters, which can be described as a miniaturized calorimeter with sample volume less than a few microliters. Massively parallel measurements are possible with calorimeter arrays, and the individual measurements themselves take less time because of the reduced sample volume. The sample volume required for a single measurement can be reduced from mililiter range to microliter and nanoliter range. However, there are also problems arising

from miniaturization; for example existing chip calorimeters can be limited by poor sensitivity and awkward sample handling. Chip calorimeters can be classified into two categories according to the reaction chamber type: “open chamber” type [23-27] and “closed chamber” type [28, 29].

1.3.3.1 Open Chamber Chip Calorimeters

Open chamber chip calorimeters are built on thermally isolated wells or flat surfaces onto which samples are spotted as droplet by micropipette or inkjet (Figure 1-7).

Open chamber chip calorimeters have disadvantages due to the fact that the sample is in direct contact with its surroundings. Because measurements, and even the reactions, can be easily influenced by environmental changes such as temperature and humidity, strict control of the external conditions is necessary to obtain measurements with good sensitivity and repeatability. The evaporation of liquid removes heat from the sample, and this gives an offset and drift to the signal. This effect becomes more important in smaller samples because of their bigger surface-to-volume ratio. To suppress these effects, careful differential measurements are required. In addition, evaporation gives limitations on the minimum practical sample volume. One can dispense samples as small as 10 pL with high-accuracy pipetting system. However, sample in this volume regime can evaporate and dry out quickly [13] as to preclude measurement. Another important source of false signal is heating by mechanical energy. When a sample is dropped onto the sensing region, it induces a transient signal due to the mechanical energy of deposition. This has been a major hurdle in development of chip calorimeters. The chip calorimeter developed by Torres et al. [23] employs an electrostatical merging of liquid

sample to avoid this problem. These researchers carry out injection of samples on the sensing region separately, and then merged the samples isothermally.

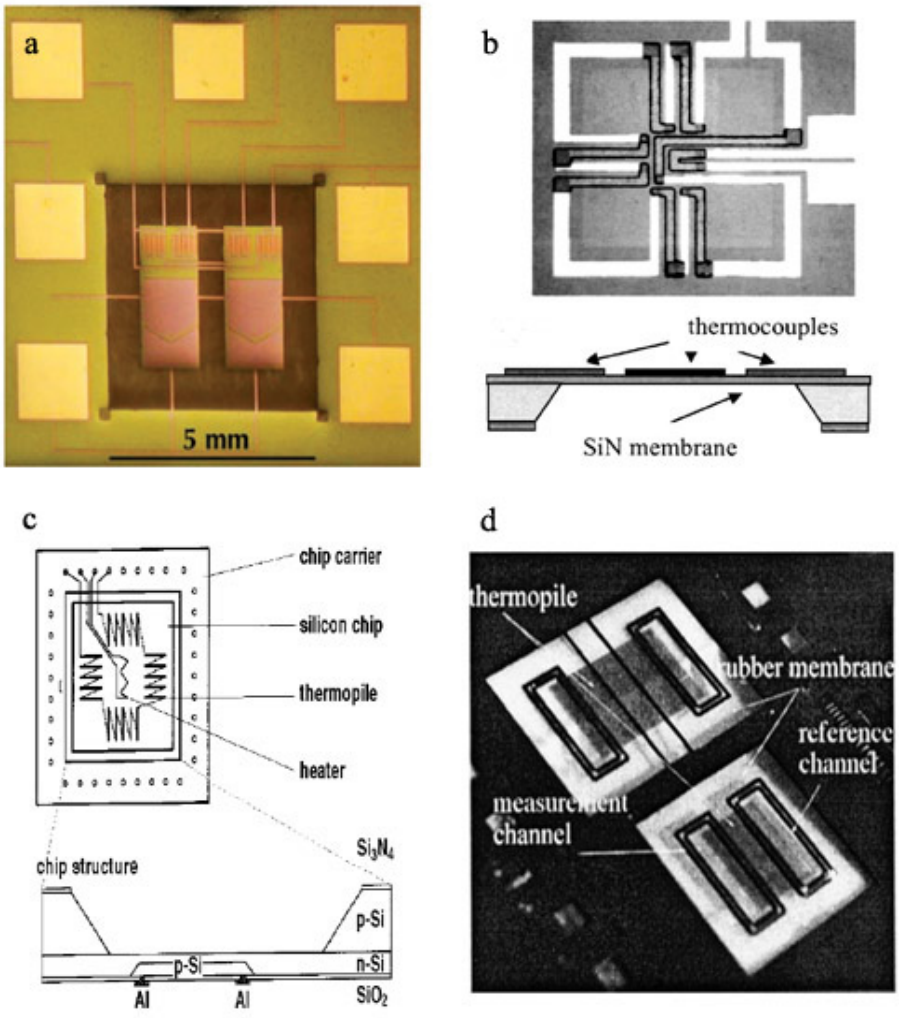

Figure 1-7. Open chamber chip calorimeters, a. liquid merging panel and Si thermistor on SiN membrane [23], b. Bi-Ni thermopile on SiN membrane [24], b. p-Si thermopile with Si well [25], d. Si thermopile on rubber membrane [26].

Though open chamber chip calorimeters have disadvantages in the area of sample handling, this type of calorimeter can provide fairly good sensitivity (1.5 nW [24] and 1

μW [23]). Air and thin membranes give considerably good thermal insulation compared to the materials used for closed chamber chip calorimeters. One can have denser calorimeter array with open chamber chip calorimeters because they do not involve fluidic channels and on-chip control. However, microinjection systems, such as an automated pipetting system or inkjet deposition methods, can be costly and limit the application of the device.

1.3.3.2 Closed Chamber Chip Calorimeters

Closed chamber chip calorimeters contain microfluidic channels and closed reaction chambers in which the samples are mixed and reactions occur (Figure 1-8).

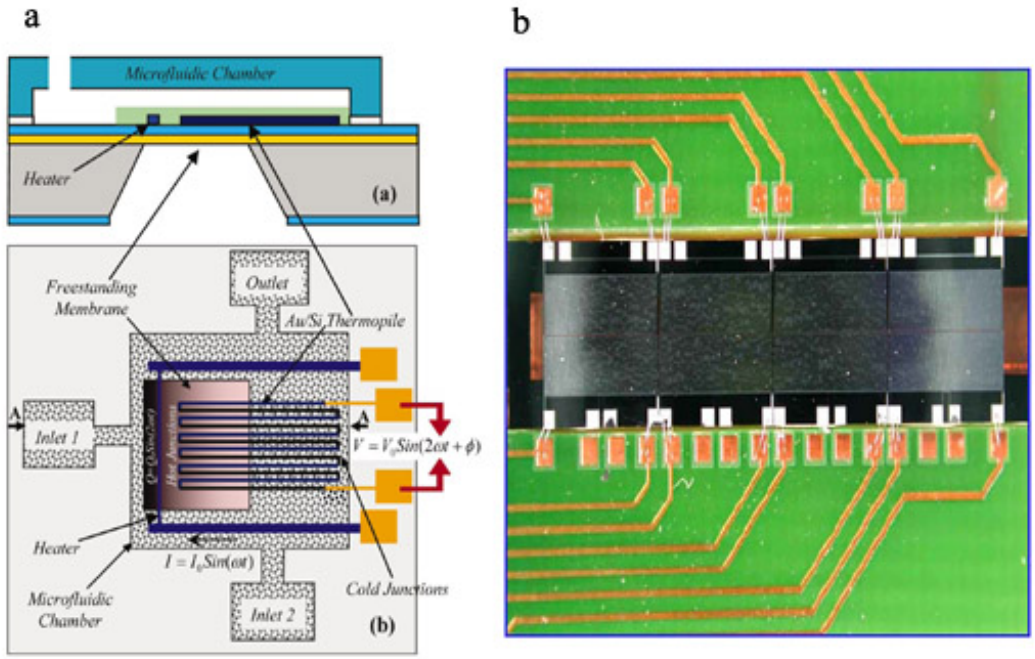

Figure 1-8. Closed chamber chip calorimeters, a. thermopile on SiN with glass microfluidic chamber [28], b. thermopiles on SiN along PMMA microfluidic channel [29].

Because this type of calorimeter is a closed system, the sample is physically isolated from the environment. Microfluidic systems permit careful sample handling, while minimizing issues such as sample evaporation and susceptibility to external noise. PDMS microfluidic systems with pneumatic valves and pumps allows diverse functions and microfluidic control with ease and accuracy [30, 31]. Moreover, integration with other lab-on-a-chip functions offers noble prospects for studies of reaction thermodynamics and mass transport in microfluidic scale [32].

While its microfluidic capability offers significant versatilities, the sensitivity of closed chamber chip calorimeters can be severely degraded by the large device heat capacity and heat loss. Conventional microfluidic devices are built with materials, such as glass and plastic, which are usually patterned by etching or molding. Because the microfluidic channels are usually constructed from the bulk substrate, the device heat capacity (often called the heat capacity of addenda) is inevitably large as is the device thermal conductance. The device heat capacity is one of the important parameters that determine its sensitivity, which, in turn, determines the lower bound of the sample volume that is measurable. Existing closed chamber chip calorimeters have, to date, only operated as flow calorimeters, because the effective sample heat capacity increases with flow and the device heat capacity, accordingly, can become relatively small in proportion. The advantages and disadvantages mentioned above are summarized in Table 1-3.

Table 1-3. Advantages and disadvantages of different types of chip calorimeters

	Advantage	Disadvantage
Open Chamber	Good sensitivity Easier fabrication	Poor sample control Large transient signals Evaporation of sample Requires separate sample dispensing unit
Closed Chamber	Freedom of sample control Good sample isolation Possibility of integration Low noise	Lower sensitivity Large sample volume

1.4 Structure of the Thesis

In Chapter 1, chip calorimeters have been introduced. Biosensors are introduced and categorized according to their recognition elements and transducers. Then, the benefits of miniaturized biosensors are discussed. For background, the basic theory and classification of calorimeter is then provided. The current status of chip calorimeter is surveyed and common problems are discussed. Parylene properties and microfabrication issues are discussed in Chapter 2. Parylene-based microfluidic structures combined with PDMS microfluidic control are used in this work to overcome the limitations of chip calorimeters discussed in Chapter 1. Parylene thin films enable microfluidic systems possessing good thermal and electric isolation with high mechanical strength. In addition Parylene is good for biological and chemical sensor applications due to its

biocompatibility and chemical resistance. Parylene microfabrication techniques providing for better device yield and stability.

In Chapter 3, chip calorimeters integrated with Parylene microfluidic systems are presented. These devices are conduction calorimeters designed to follow for biochemical reactions. These devices provide enhanced isolation and improved fluidic control compared to previous realizations. The design, fabrication and calibration of these devices are described; these chip calorimeters are designed for heat of reaction measurements upon 3.5 nL samples. Their performance is demonstrated by heat of mixing and enzyme activity measurements. The demonstrations show improved sensitivity with reliable microfluidic control.

Chapter 4 describes the chip-based flow calorimeter for sensor applications and measurements of cellular metabolism. Further improvement of sensitivity will enable real-time analysis of the metabolism of individual cells. Finally, Chapter 5 provides the concluding remarks about potential future applications of the chip calorimeter.

References

1. Cunningham, A.J., *Introduction to Bioanalytical Sensors*. 1998, New York: John Wiley & Sons, INC.
2. Mosbach, K. and B. Danielss, *Enzyme Thermistor.* Biochimica et Biophysica Acta, 1974. **364**(1): p. 140-145.
3. Blum, L.J. and P.R. Coulet, *Biosensor Principles and Applications*. 1991, New York: Marcel Dekker.
4. Cheng, J. and L.J. Kricka, *Biochip Technology*. 2001, London: Taylor & Francis.
5. Scheller, F. and F. Schubert, *Biosensor*. Techniques and Instrumentation in Analytical Chemistry. Vol. 11. 1992, Amsterdam: Elsevier.
6. Buck, R.P., et al., *Biosensor Technology- Fundamentals and Application*. 1990, New York: Marcel Dekker.
7. Collings, A.F. and F. Caruso, *Biosensors: Recent advances.* Reports on Progress in Physics, 1997. **60**(11): p. 1397-1445.
8. Keusgen, M., *Biosensors: New approaches in drug discovery.* Naturwissenschaften, 2002. **89**(10): p. 433-444.
9. Nakamura, H. and I. Karube, *Current research activity in biosensors.* Analytical and Bioanalytical Chemistry, 2003. **377**(3): p. 446-468.
10. Vadgama, P. and P.W. Crump, *Biosensors - recent trends - a review.* Analyst, 1992. **117**(11): p. 1657-1670.
11. Ziegler, C., *Cantilever-based biosensors.* Analytical and Bioanalytical Chemistry, 2004. **379**(7-8): p. 946-959.

12. Monk, D.J. and D.R. Walt, *Optical fiber-based biosensors.* Analytical and Bioanalytical Chemistry, 2004. **379**(7-8): p. 931-945.

13. Madou, M.J. and R. Cubicciotti, *Scaling issues in chemical and biological sensors.* Proceedings of the IEEE, 2003. **91**(6): p. 830-838.

14. Weigl, B.H., R.L. Bardell, and C.R. Cabrera, *Lab-on-a-chip for drug development.* Advanced Drug Delivery Reviews, 2003. **55**(3): p. 349-377.

15. Manz, A., N. Graber, and H.M. Widmer, *Miniaturized total themical-analysis aystems - a novel concept for chemical sensing.* Sensors and Actuators B-Chemical, 1990. **1**(1-6): p. 244-248.

16. Reyes, D.R., et al., *Micro total analysis systems. 1. Introduction, theory, and technology.* Analytical Chemistry, 2002. **74**(12): p. 2623-2636.

17. Lee, S.J. and S.Y. Lee, *Micro total analysis system (μ-TAS) in biotechnology.* Applied Microbiology and Biotechnology, 2004. **64**(3): p. 289-299.

18. Petersen, K.E., et al., *Toward next generation clinical diagnostic instruments: Scaling and new processing paradigms.* Biomedical Microdevices, 1998. **1**: p. 71-79.

19. *Calorimeter*, Britanica online, http://www.britannica.com/eb/article-9018727/calorimeter.

20. Zielenkiesicz, W. and E. Margas, *Theory of Calorimetry*. Hot Topics in Thermal Analysis and Calorimetry, ed. J. Simon. Vol. 2. 2002, Dordrecht: Kluwer Academic Publishers.

21. Hemminger, W. and G. Hohne, *Calorimetry- Fundamentals and Practice*. 1984, Veinheim: Verlag Chemie.

22. Weber, P.C. and F.R. Salemme, *Applications of calorimetric methods to drug discovery and the study of protein interactions.* Current Opinion in Structural Biology, 2003. **13**(1): p. 115-121.

23. Torres, F.E., et al., *Enthalpy arrays.* Proceedings of the National Academy of Sciences of the United States of America, 2004. **101**(26): p. 9517-9522.

24. Chancellor, E.B., et al., *Heat conduction calorimeter for massively parallel high throughput measurements with picoliter sample volumes.* Applied Physics Letters, 2004. **85**(12): p. 2408-2410.

25. Lerchner, J., A. Wolf, and G. Wolf, *Recent developments in integrated circuit calorimetry.* Journal of Thermal Analysis and Calorimetry, 1999. **57**(1): p. 241-251.

26. Verhaegen, K., et al., *A high-throughput silicon microphysiometer.* Sensors and Actuators A-Physical, 2000. **82**(1-3): p. 186-190.

27. Johannessen, E.A., et al., *Micromachined nanocalorimetric sensor for ultra-low-volume cell-based assays.* Analytical Chemistry, 2002. **74**(9): p. 2190-2197.

28. Zhang, Y.Y. and S. Tadigadapa, *Calorimetric biosensors with integrated microfluidic channels.* Biosensors & Bioelectronics, 2004. **19**(12): p. 1733-1743.

29. Baier, V., et al., *Highly sensitive thermopile heat power sensor for micro-fluid calorimetry of biochemical processes.* Sensors and Actuators A-Physical, 2005. **123-24**: p. 354-359.

30. Whitesides, G.M., et al., *Soft lithography in biology and biochemistry.* Annual Review of Biomedical Engineering, 2001. **3**: p. 335-373.

31. Quake, S.R. and A. Scherer, *From micro- to nanofabrication with soft materials.* Science, 2000. **290**(5496): p. 1536-1540.

32. Melin, J. and S.R. Quake, *Microfluidic large-scale integration: The evolution of design rules for biological automation.* Annual Review of Biophysics and Biomolecular Structure, 2007. **36**: p. 213-231.

Chapter 2

Parylene for Microfluidic Applications

2.1 Parylene

Parylene is the generic name for an insulating thermoplastic polymer series, poly(p-xylene) [1], which is widely used for various coating applications. The Parylene polymer series was first isolated by Michael M. Szwarc in the late 1940s at the University of Manchester. William Gorham, a Union Carbide Corporation scientist, later developed a deposition process, and Union Carbide commercialized the material and process. Currently three types of Parylene are commercially available: Parylene N, Parylene C, and Parylene D (Figure 2-1).

The basic member of the series is Parylene N. It is a linear, highly crystalline material. Parylene C is produced from the same monomer modified by substitution of a chlorine atom for one of the aromatic hydrogens. Similarly, Parylene D is produced from the same monomer modified by substitution of chlorine atoms for two of the aromatic

hydrogens. The properties of Parylene C are similar to those of Parylene D. We employ Parylene C in our research because it provides the best fluidic barriers and has the best thermal insulation properties. For all the experiment described in this thesis, "Parylene" refers to Parylene C. The properties of Parylene will be discussed further in the following sections.

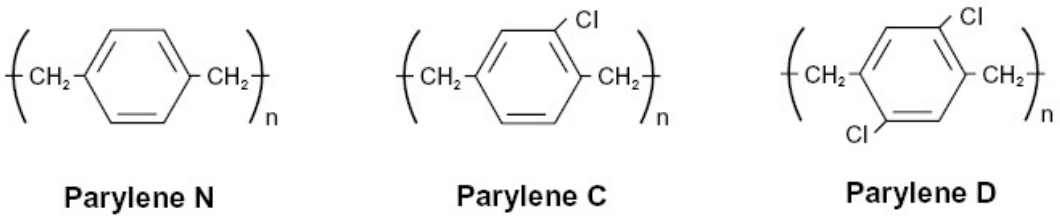

Figure 2-1. Parylene chemical structures.

2.1.1 The Parylene Deposition Process

Unlike the most of other polymers Parylene is deposited on substrate by gas phase polymerization [2] (Figure 2-2). The steps are as follows. First, the commercially available Parylene dimer in solid form (powder) is sublimated by heating (~150 ºC). Then, the dimer is pyrolized into monomers at higher temperature (~680 ºC). The monomer in gas phase then flows into the deposition chamber kept at room temperature, where the pressure is maintained around 0.1 Torr. In the deposition chamber, the monomer gas cools and condenses onto the substrate and polymerizes into long chains. Because the mean free path of gas molecules at this pressure is ~100 μm, the coating is

conformal. This is different from line-of-sight metal deposition (e.g., thermal evaporation), which is typically done below 10^{-5} Torr and is not conformal.

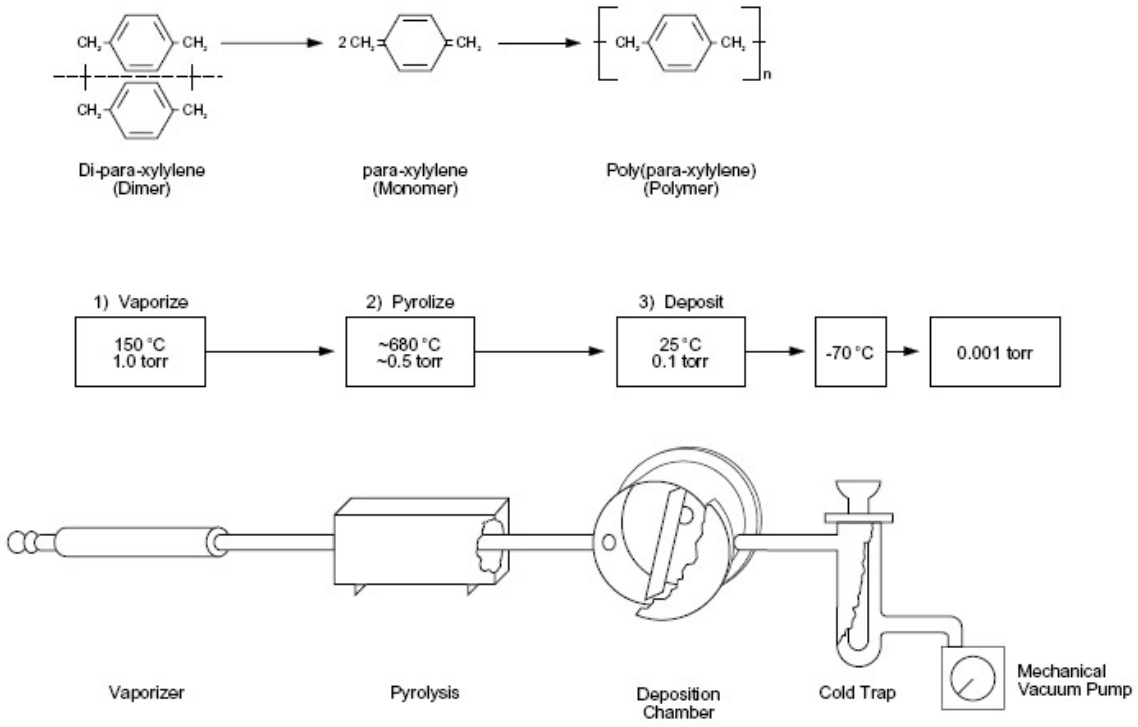

Figure 2-2. The deposition process for Parylene N.

Parylene deposition has many advantages over other material coating processes. Because it is conducted at room temperature, it is ideal for coating the substrate that cannot sustain high temperatures. Furthermore, the coated film has minimal built in stress. Spin coating techniques are widely used for applying polymers on a substrate; however, this approach is often problematic. First, fluidic effects, such as pooling, flowing and bridging, yield non-uniform coverage. While spin coating is very simple, it cannot be applied to complex geometries and large objects. Second, spin coatings always posess pinholes and large intrinsic stress. Finally, the solvents employed can have adverse

effects on the substrate; in extreme case, it may dissolve the substrate or alter its properties. Because Parylene is deposited in gas phase, the process circumvents these problems.

Many Parylene coating systems are commercially available, and the deposition processes are automated. In our work, we used a PDS 2010 Labcoater 2 Parylene deposition system from Specialty Coating systems.

2.1.2 Parylene Properties

Parylene has been used in industry as a coating material for protection, insulation or the deposition of anti-friction layers. It can provide very thin (as thin as ~50 nm) films, yet its protecting ability is superior to other coating materials. Parylene thin-films are very good insulator against both electrical and thermal conduction. Parylene is also very chemically stable and insoluble in all organic solvent. It is resistant to chemical attack at room temperature from most reagents. In addition, it has very low gas permeability. With its conformal coating property and chemical compatibility, it is very well-suited as protective coatings for circuit boards and electronic device packaging.

Another important property of Parylene is its biocompatibility and biostability. Parylene film is formed from a pure molecular precursor (a monomer gas) in modest vacuum. In these deposition conditions there is very low chance for the Parylene coating to be contaminated by any foreign particles or chemical substances. Unlike spin coated polymer films, Parylene films do not suffer from chemical outgasing (e.g solvent, plasticizer, catalyst, or accelerant). In biomedical applications the resulting films have demonstrated very low thrombogenic properties and low potential to trigger immune

response. Parylene's high chemical resistance also ensures its stability in corrosive body fluids, electrolytes, proteins, enzymes, and lipids. Hence, as in the case of electronics coatings, Parylene coating works as very effective barrier in biological settings, not only protecting the substrate form environment but also protecting the biological. In case of the implant coating, the passage of potential contaminants from the are blocked. Several sterilization methods can be applied to Parylene enabling its use for medical applications; these methods include steam autoclaving, gamma and e-beam radiation, and sterilization via hydrogen peroxide plasma or ethylene oxide.

One of drawbacks of Parylene coatings compared to inorganic coating, however, is its low thermal stability. Parylene has meting points (~300 ºC to 400 ºC) and glass transition temperatures (~80 ºC to 150 ºC) that are relatively low. Recently, Parylene HT, with improved thermal properties, was commercialized by Specialty Coating Systems. The basic properties of Parylene are summarized in Table 2-1.

Table 2-1. Parylene properties [1]

Property	***Parylene N***	***Parylene C***	***Parylene D***
Physical			
Density [g/cm^3]	1.110	1.289	1.418
Refractive index	1.661	1.639	1.669
Static Friction Coefficient	0.25	0.29	0.33
Mechanical			
Secant modulus [GPa]	2.4	3.2	2.8
Tensile strength [MPa]	45	70	75
Yield strength [MPa]	42	55	60
Elongation to break [%]	20-250	200	10
Electrical			
Dielectric constant at 1kHz	2.65	3.10	2.82
Dissipation factor at 1kHz	0.0002	0.019	0.003
Dielectric strength at 1mil [V/mil]	7000	5600	6500
Volume resistivity at 23 ºC [Ω·cm]	1.4×10^{17}	8.8×10^{16}	1.2×10^{17}
Surface resistivity at 23 ºC [Ω·cm]	1×10^{13}	1×10^{14}	1×10^{16}
Thermal			
Melting point [ºC]	420	290	380
Linear expansion coefficient at 25 ºC [K^{-1}]	6.9×10^{-5}	3.5×10^{-5}	$3\text{-}8 \times 10^{-5}$
Specific heat at 20ºC [J/(g·K)]	0.84	0.71	-
Thermal conductivity at 25ºC [W/(m·K)]	0.12	0.082	-
Barrier			
Water vapor transmission at 37 ºC [ng/(Pa·s·m)]	0.0012	0.0004	0.0002
Gas permeability at 25 ºC [amol/(Pa·s·m)]			
N_2	15.4	2.0	9.0
O_2	78.4	14.4	64.0
CO_2	429	15.4	26.0

2.2 Parylene for Microfluidic Applications

Parylene has been applied to many industrial applications since its development. However, it has only recently been used for microfluidic applications [3-12]. Parylene can be used to build microfluidic channel and plumbing as well as functional microfluidic units and can also be used as a passivation layer for microfluidic channels and substrates. Parylene microfluidic structures are unique in that they are thin-film structures with uniform thickness. This is in contrast to etched structures patterned from bulk materials.

Chemical resistance and biocompatibility of Parylene makes it a good candidate for microfluidic biosensor applications. However, unlike PDMS which is widely used for multilevel microfluidics, Parylene has much higher modulus of elasticity and there is no easy way to incorporate valves. The properties of Parylene provide both advantages and disadvantages for applications. For example, its low gas permeability is good for high pressure applications but problematic for application that requires gas exchange such as cell culture. To take advantage of Parylene for microfluidic applications, it is important to establish well-developed microfabrication processes. In this section, we discuss some of the Parylene microfabrication issues and tests of the processes developed.

2.2.1 Parylene Adhesion

Parylene coatings are well-wuited to passivation application for miniaturized biosensors [11, 12]. In coating applications, the adhesion of the coating material on the substrate is critical, because the delamination of the layer must be avoided. For a microfluidic structure with integrated sensor, Parylene layers serve not only as a structural material but also as a substrate for microstructured components (e.g.,

electrodes). Therefore, the adhesion of material deposited on Parylene is also important for the overall integrity of the fabricated device. We will discuss effects and results toward enhancing the adhesion of Parylene with various materials.

2.2.1.1 Parylene Adhesion on Substrate

Typically, microelectromechanical systems (MEMS) and microfluidic devices are built on substrates such as silicon wafers or glass slides. Parylene shows excellent adhesion on porous substrates but rather poor adhesion on smooth surfaces. This behavior arises because of its polymerization mechanism [2]. To enhance the adhesion of polymers on inorganic substrates, organic coupling agents employed as adhesion promoters have been extensively studied for a long time and many are now commercially available. For Parylene, the adhesion promoter A-174 Silane (*Gamma*-Methacryloxypropyltrimethoxy Silane) is often used. A-174 Silane is one of several alkoxysilanes that works on wide rage of inorganic materials. The structure of A-174 Silane is shown in Figure 2-3.

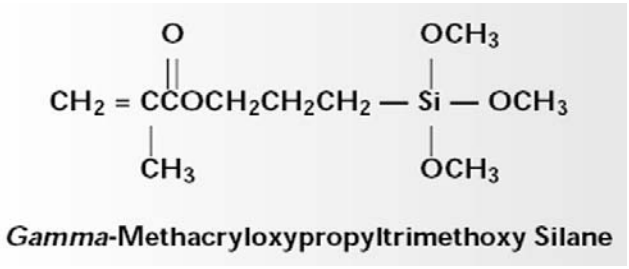

Figure 2-3. Chemical structure of A-174 Silane.

We have tested the strength of Parylene adhesion on various substrates using the simple and conventional “Scotch tape test” (ASTM D3359-97B). The test gives a quick

measure of adhesion strength. The method involves making cuts 1mm apart with razor blade to create 10 by 10 grid on the test area. Adhesive tape is then put on the grid, rubbed down to ensure a good contact, then removed from free end with 180º angle. The test area is then inspected and rated by a standard classification methodology (Table 2-2).

Table 2-2. Classification of adhesion with Scotch tape test

Classification	Description
5B	The edges of the cuts are completely smooth; none of the squares of the lattice is detached.
4B	Small flakes of the coating are detached at intersections; less than 5% of the area is affected.
3B	Small flakes of the coating are detached along edges and at intersections of cuts. The area affected is 5% to 15% of the lattice.
2B	The coating has flaked along the edges and on parts of the squares. The area affected is 15% to 35% of the lattice.
1B	The coating has flaked along the edges of cuts in large ribbons and whole squares have detached. The area affected is 35% to 65% of the lattice.
0B	Flaking and detachment worse than Grade 1.

Substrates tested include silicon wafers, silicon nitride wafers and metal films (gold, nickel, titanium and aluminum). The metal layers are prepared by thermal evaporation of metals on silicon wafers. Titanium or chrome adhesion layer are used for nickel, gold and aluminum to ensure adherence of the metal films to the silicon substrate.

The effect of adhesion promotion with Adhesion promoter (A-174) and annealing is also examined. Annealing of Parylene is carried out at 140 ºC for 2 hours. Because Parylene become damaged if heated above 105 ºC in an oxidizing atmosphere [13], the annealing is done in a vacuum oven. The test results are summarized in Table 2-3.

Table 2-3. Parylene adhesion on substrate

Substrate	No treat	Annealing	A-174
Silicon	0B	1B	5B
Silicon nitride	0B	0B	5B
Au	4B	5B	5B
Ni	0B	0B	5B
Ti	0B	5B	5B
Al	0B	1B	4B

Without any adhesion promotion, Parylene adheres poorly on most smooth surfaces with exception of gold. This poor adhesion can be explained by examining the polymerization mechanism of Parylene [2, 14]. Parylene polymerization is a “rapid step growth polymerization,” which occurs in vacuum through repeated recombination of free radicals. This is contrast with gas phase chain growth that occurs with many other

polymers. The Parylene monomer free radical preferentially react with each other rather than reacting with other species on the substrate because it is relatively stable.

Annealed Parylene shows better adhesion than Parylene that is not annealed for all the substrates investigated. For silicon and silicon nitride, even though annealing does not seem to improve the adhesion sufficiently to be classified within a different category (Table 2.2 and 2.3), some improvement is observed. When not annealed, Parylene film adhesion is so poor that the films delaminate while cutting with razor blade, i.e. prior to the Scotch tape test. After annealing, the films show moderate strength and endure the cutting process. Adhesion promotion by annealing was most effective for the titanium layers.

As expected, A-174 Silane treatment significantly improved Parylene adhesion on all the test substrates. It is found to be desirable to treat the substrate with the adhesion promoter before depositing Parylene, whenever the substrate allows application of adhesion promoter.

Usually A-174 alone provides very good adhesion, however, it is found that surface roughening can be used to further increase adhesion strength by increasing mechanical interlocking. Surface roughening can be achieved in several ways such as plasma etching and chemical vapor etching. For example, bromine trifluride (BrF_3) vapor etching is effective for roughen silicon wafer surfaces [15].

Plasma polymerization has been reported to enhance the adhesion of Parylene on metal surfaces [16]. However this technique requires the system that can perform plasma polymerization followed by Parylene deposition without breaking vacuum.

2.2.1.2 Metal Deposition on Parylene

It is crucial to achieve strong adhesion of metal on Parylene for good integrity of Parylene MEMS devices. There have been several reports on enhancement of metal adhesion on Parylene surfaces through plasma treatments [17-20]. We have tested the effect of plasma treatment on adhesion strength of a several metals on Parylene surface. The materials tested are gold, aluminum, nickel, titanium and chromium.

Samples are prepared as following. Glass slides are coated with 1μm thick Parylene after treatment with adhesion promoter. The samples are then treated with oxygen plasma, carbon tetrafluoride (CF_4), methane (CH_4) or argon plasma (100mTorr, 140W) for 10s. A sample without plasma treatment was also prepared for control experiment. On these samples ~60nm thick metals are deposited by thermal evaporation. Adhesion strength was tested with the Scotch tape test. Results of these tests are shown in Table 2-4.

Table 2-4. Effect of plasma treatment on metal adhesion

Material	No treat	O_2	CF_4	CH_4	Ar
Gold	0B	5B	1B	0B	0B
Aluminum	4B	5B	5B	0B	0B
Nickel	0B	5B	5B	5B	5B
Titanium	5B	5B	5B	0B	0B
Chromium	5B	5B	5B	5B	5B

It is known that oxygen plasma treatment enhances gold adhesion on Parylene by generating carbonyl groups on the surface, and by increasing surface roughness [18]. The

test results show that an oxygen plasma treatment enhances the adhesion for all materials. Titanium and chrome adhere well without treatment, hence the adhesion enhancement after an oxygen plasma couldn't be evaluated. However, we confirmed that it does not have adverse effect, as methane plasma and argon plasma exhibited. Carbon tetrafluoride plasma is also found to enhance the adhesion though it's not as effective as oxygen plasma. Carbon tetrafluoride plasma does not change Parylene surface hydrophobicity very much, while oxygen plasma changes the surface to become hydrophilic.

Without treatment each metal are found to have distinctive adhesion strength on Parylene. Materials having poor adhesion on silicon substrates are found to have poor adhesion on Parylene as well. To achieve good adhesion of these materials on Parylene, titanium or chrome adhesion layers can be applied. If adhesion layers are not allowed due to conflicting fabrication process, oxygen plasma treatment can be a good alternative.

2.2.2 Patterning of Parylene

Patterning of Parylene cannot be achieved with wet etching because of its excellent chemical inertness. Although there are a few chemicals that can dissolve Parylene at elevated temperatures [1], these methods are not compatible with most microfabrication processes. However, several Parylene patterning techniques are reported. Selective deposition has been demonstrated using local heating technique [21] and transition metal patterning [22]. UV laser ablation can be used to etch Parylene [23]. However, the only simple and practical method for patterning Parylene is etching with oxygen plasma [24-31].

2.2.2.1 Etching of Parylene by RIE

Dry etching with an oxygen-containing plasma is effective on many polymers including Parylene. Plasma etching (PE) [24-29] and reactive ion etching (RIE) [30, 31] have been applied to etch Parylene. Callahan et al. [25] hypothesized the etching mechanism of Parylene as comprised of the following steps. Etching is initiated with hydrogen abstraction from the ethyl carbons between the benzene rings. Then, oxygen molecules or atoms are adsorbed on the exposed reactive sites. They subsequently rearrange and volatilize to form carbon monoxide or dioxide. If these steps occur again adjacent to the radical sites, the benzene ring can open. After the opening of the benzene ring, the process is similar to the etching process of saturated carbon compounds.

We have conducted RIE (MicroRIE, PES) on Parylene and measured the etching rate obtained under various conditions. RIE was chosen because the etching rate is relatively high and the side walls obtained are nearly vertical.

Etching tests were conducted in following way. A 2.5 μm thick Parylene layer was deposited on glass slides that has been pre-treated with A-174 Silane adhesion promoter. A 60 nm thick gold layer was then deposited as an etching mask. A 3 nm thick chromium underlayer was used as an adhesion layer for the gold. These metallic layers were patterned using photolithography and wet chemical etching. Using these etch mask, the Parylene layer was then plasma etched. First, the etching rate at constant pressure was measured with varying rf power. The chamber pressure was set to 150 mTorr with continuous oxygen flow. Second, the etching rate at constant rf power was measured with varying pressure. In this set of tests the rf power was set to 150 W. Finally, etching

chemistry was altered by adding CF_4 gas. The ratio of oxygen and CF_4 was varied, and the chamber pressure and rf power was set to 150 mTorr and 150 W, respectively.

During these etching tests the Parylene sample temperature was maintained at room temperature, although the real temperature at the etching surface may be slightly higher than the sample. The control of the temperature is important because it is known that the etching rate increases with temperature. After etching, the mask was removed and the resulting Parylene layer thicknesses are measured with XP2 profilometer (Ambios). The results are shown in Figure 2-4.

An increase in rf power leads to higher oxygen atom density in the plasma, and thus, in turn, seems to give higher etching rate. This trend is evident in Figure 2-4a, which shows that the etching rate is directly proportional to rf power. However, at the highest powers employed the trend deviates from linearity. In this regime, the etching rate is apparently limited by the flow of reactants. At high powers, the amount of reaction products, such as CO_2 and H_2O, also increases and this can also start to limit the etching rate. Yeh et al. [30] show in detail that the etching rate can be limited by the accumulation of reaction products. An increase in rf power can also give stronger physical etching. However, this effect is negligible because physical etching effect is very small compared to the chemical etching.

The dependence of etching rate on pressure is not as significant as the dependence on power. The etching rate first increases with pressure, but decreased beyond certain point. This tendency can be explained by an increased recombination rate of oxygen atoms at high pressure, which results in a decrease in the concentration of the active etchant species.

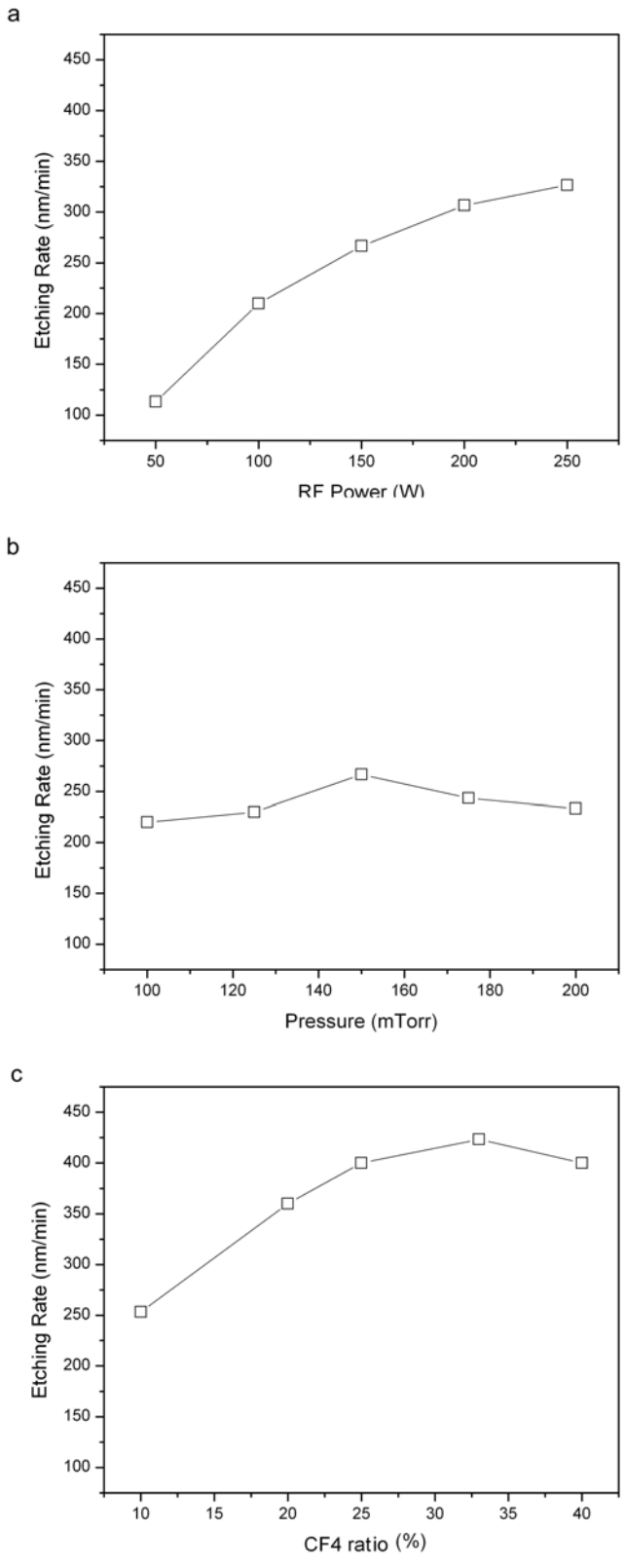

Figure 2-4. Etching rate with a. varying power, b. varying pressure, c. varying CF_4 ratio.

When CF_4 gas was mixed with oxygen, the etching rate was found to increase beyond the rate achievable with a pure oxygen plasma. The presence of CF_4 is known to increase the concentration of oxygen atoms in the plasma. It is believed that the presence of the fluorine species increase the density and energy of electrons in the plasma. Hence, the CF_4 component not only enhance oxygen atom generation but also activates Parylene by generating radical sites. However, the etching of Parylene with fluorine atom is not as effective as etching with oxygen atom. As shown in Figure 2-4c, the etching rate reached maximum with a CF_4 ratio of ~33%. Above this ratio, the decrease in oxygen partial pressure tappears to counteract the etching rate enhancement obtained with CF_4 addition.

2.2.2.2 Etching profiles

Profiles of structures after etching were examined with scanning electron microscopy (SEM) and atomic force microscopy (AFM).

In Figure 2-5, Parylene structures patterned by the RIE process are shown. The etching was conducted with 150 W rf power at 150 mTorr in a 1 : 4 mixture of CF_4 and O_2 gases for 3 minutes. The etching depth obtained was 1.1 μm. A gold layer with a chromium for underlayer adhesion layer was used for the mask. This metallization was removed after the RIE processes. The RIE process was stopped before the Parylene layer was completely etched away in the unmasked region.

As shown in the Figure 2-5, the etching by RIE produces nearly vertical side walls. Yet, there is a limitation on the structural aspect ratio that can be achieved with etching by RIE; structures with aspect ratio up to ~1 : 3 can be achieved routinely. Deep reactive ion etching (DRIE) has been reported for the high aspect ratio polymer structures of ~1 :

20 [32]. Etching by RIE tends to give more vertical side walls by low power and low pressure plasma, but these conditions also yield rough etched surfaces.

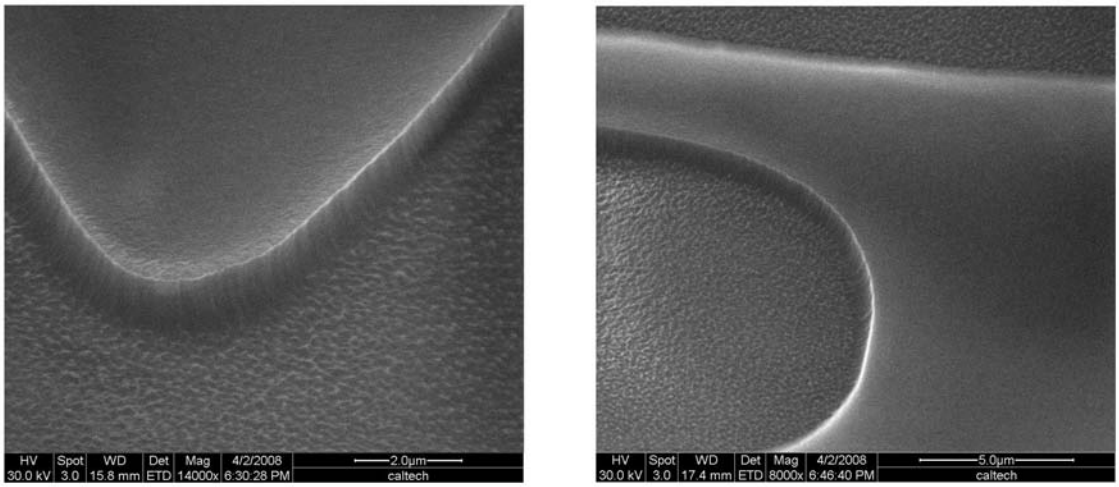

Figure 2-5. SEM images of Parylene patterned via RIE.

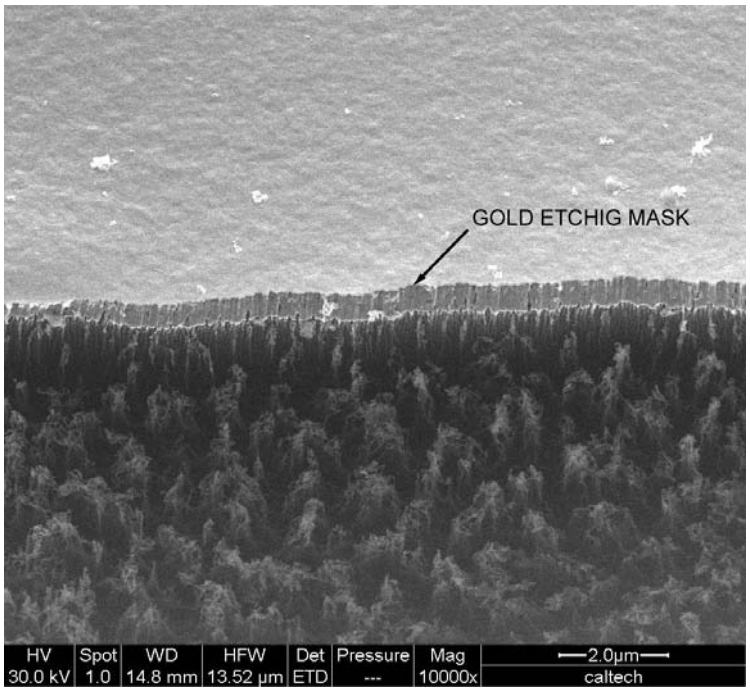

Figure 2-6. Parylene surface morphology after etching by RIE at low pressure.

Figure 2-6 shows a Parylene film etched for 4 minutes at 100 mTorr pressure in pure oxygen plasma generated by 100 W rf power. Almost vertical side walls are achieved with these conditions but micrograss structures are developed on the etched surface. If the etched surface is important in the function of the device, this roughness could be problematic.

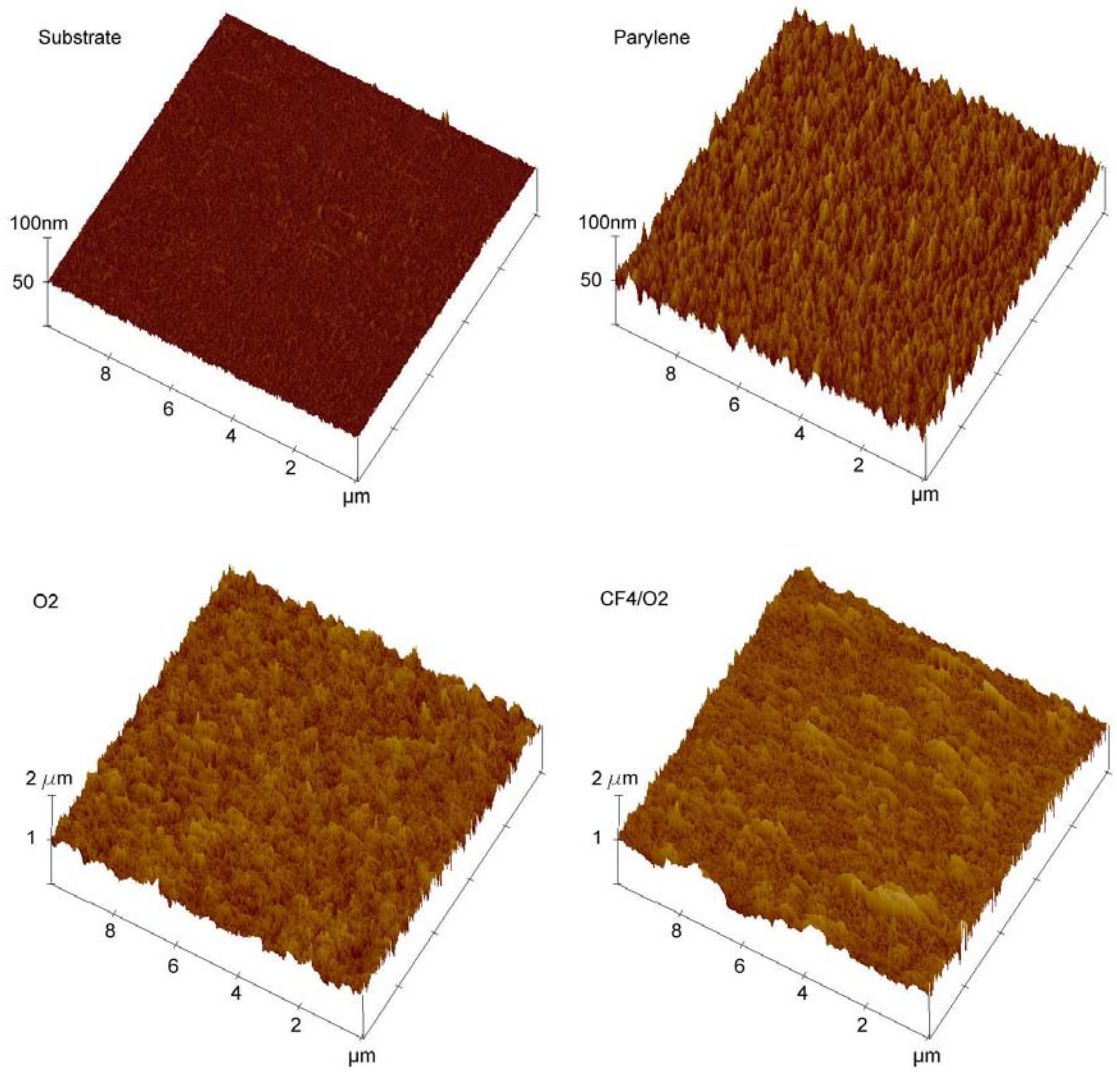

Figure 2-7. Surface roughness of Parylene after etching by RIE under various conditions (see text).

Parylene surface roughness was measured with an AFM. Four samples were prepared to compare the surface roughness resulting from two representative etching conditions. Parylene is deposited on the glass slides. These Parylene surfaces are then etched with a pure oxygen plasma (150 mTorr, 200 W), and with 80% oxygen and 20% CF_4 plasma (150 mTorr, 150 W). A bare glass substrate and an as-deposited Parylene film are also evaluated for comparison.

The Parylene coating is truly conformal; the as-deposited Parylene film shows fine grain structures with ~4.6 nm surface roughness (Figure 2-7) As shown in SEM image the Parylene surface can be considered as fairly smooth but slightly rougher then the uncoated surface. On the other hand, the etched surfaces showed an order of magnitude increase in roughness over that of the pristine film. Oxygen plasma gave the largest roughness with fine spikes.

Table 2-5. Surface roughness of etched Parylene

	Substrate	Parylene as-deposited	Parylene after O_2 RIE	Parylene after O_2/CF_4 RIE
Roughness	1.4 nm	4.6 nm	79 nm	61 nm

2.2.3 Fluidic Channels

Parylene microfluidic channels are fabricated by depositing the polymer on a sacrificial channel structure utilizing its properties of conformal coating. The fabrication steps yielding a simple channel are illustrated in Figure 2-7. First, a base Parylene layer is deposited on the substrate, which has been pre-treated with adhesion promoters. Second,

photoresist that is used as sacrificial layer is spun onto the first Parylene layer, and patterned to form the channel. The height and width of the Parylene channel are determined by the geometry of the patterned sacrificial layer. Once the sacrificial structure is patterned, the second Parylene layer is deposited upon it. Again, because the Parylene deposition is conformal, the photoresist structure is completely encapsulated by the top and base Parylene layers after this step. The wall thickness is determined by the thickness of the second Parylene film. After the structure is built, the channel ends are etched with the RIE process to open the inlet and outlet. This step requires an augment mask layer patterned by e-beam of optical lithography and subsequent lift-off. Finally, the photoresist inside the channel is removed with solvent.

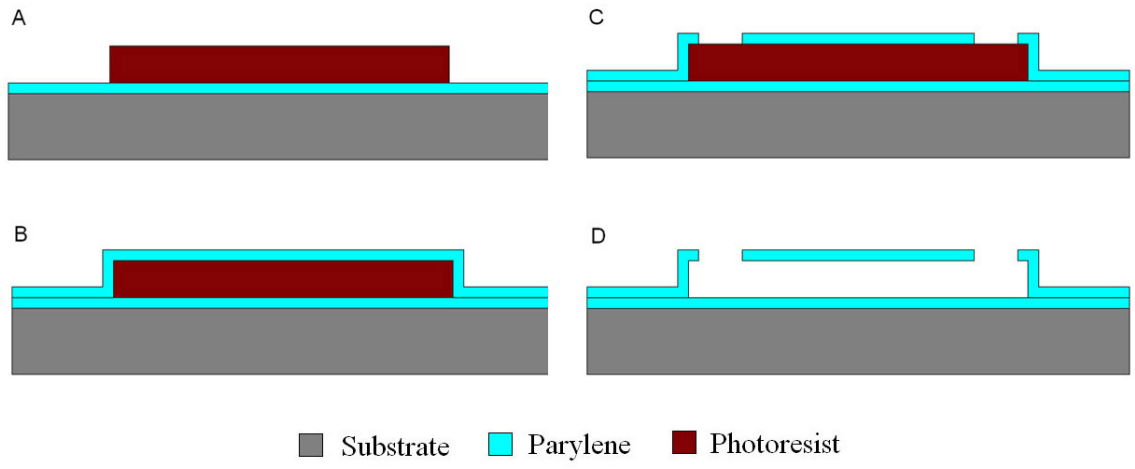

Figure 2-8. Parylene microfluidic channel fabrication.

The problematic aspect of this fabrication technique is that removal of the photoresist sacrificial structure can take long time. Typically, the dissolution speed of the photoresist (DNQ Novolak resist) in the channel is ~2 mm/hour when acetone is used as

solvent. This speed may be acceptable for microfluidic applications requiring channels up to a few centimeter long. However for applications requiring long fluidic channels, such as microfabricated gas chromatography columns, it can take several days to a few weeks to dissolve the photoresist sacrificial layer. To overcome this limitation, a Parylene micromolding technique has been developed by Noh et al [6]. This technique uses an etched silicon wafer as a mold for Parylene. Another layer of Parylene is thermally bonded to the first Parylene layer and completed structure is then released from the mold. This new technique can permit rapid channel fabrication, regardless of the channel length. For our device, described in Chapter 3 and Chapter 4, the channel length is less than a centimeter. Hence, we employed the conventional channel fabrication method.

References

1. *Parylene*, Specialty Coating Systems, http://www.scscoatings.com/parylene_knowledge/index.aspx
2. Yasuda, H.K., Y.S. Yeh, and S. Fusselman, *A Growth-mechanism for the vacuum deposition of polymeric materials.* Pure and Applied Chemistry, 1990. **62**(9): p. 1689-1698.
3. Moon, H., et al., *Low voltage electrowetting-on-dielectric.* Journal of Applied Physics, 2002. **92**(7): p. 4080-4087.
4. Webster, J.R., et al., *Monolithic capillary electrophoresis device with integrated fluorescence detector.* Analytical Chemistry, 2001. **73**(7): p. 1622-1626.
5. Selvaganapathy, P., E.T. Carlen, and C.H. Mastrangelo, *Electrothermally actuated inline microfluidic valve.* Sensors and Actuators A-Physical, 2003. **104**(3): p. 275-282.
6. Noh, H.S., Y. Huang, and P.J. Hesketh, *Parylene micromolding, a rapid and low-cost fabrication method for Parylene microchannel.* Sensors and Actuators B-Chemical, 2004. **102**(1): p. 78-85.
7. Xie, J., et al., *An electrochemical pumping system for on-chip gradient generation.* Analytical Chemistry, 2004. **76**(13): p. 3756-3763.
8. Xie, J., et al., *Microfluidic platform for liquid chromatography-tandem mass spectrometry analyses of complex peptide mixtures.* Analytical Chemistry, 2005. **77**(21): p. 6947-6953.

9. Noh, H.S., P.J. Hesketh, and G.C. Frye-Mason, *Parylene gas chromatographic column for rapid thermal cycling.* Journal of Microelectromechanical Systems, 2002. **11**(6): p. 718-725.

10. Ryu, K.S., et al., *Micro magnetic stir-bar mixer integrated with Parylene microfluidic channels.* Lab on a Chip, 2004. **4**(6): p. 608-613.

11. Shin, Y.S., et al., *PDMS-based micro PCR chip with parylene coating.* Journal of Micromechanics and Microengineering, 2003. **13**(5): p. 768-774.

12. Chang, T.Y., et al., *Cell and protein compatibility of Parylene C surfaces.* Langmuir, 2007. **23**(23): p. 11718-11725.

13. Monk, D.J., H.S. Toh, and J. Wertz, *Oxidative degradation of Parylene C (poly(monochloro-para-xylylene)) thin films on bulk micromachined piezoresistive silicon pressure sensors.* Sensors and Materials, 1997. **9**(5): p. 307-319.

14. Yasuda, H., et al., *Interface-engineered Parylene C coating for corrosion protection of cold-rolled steel.* Corrosion, 1996. **52**(3): p. 169-176.

15. Yao, T.J., X. Yang, and Y.C. Tai, *BrF3 dry release technology for large freestanding parylene microstructures and electrostatic actuators.* Sensors and Actuators A-Physical, 2002. **97-8**: p. 771-775.

16. Sharma, A.K. and H. Yasuda, *Effect of glow-discharge treatment of substrates on Parylene-substrate adhesion.* Journal of Vacuum Science & Technology, 1982. **21**(4): p. 994-998.

17. Gadre, K.S. and T.L. Alford, *Contact angle measurements for adhesion energy evaluation of silver and copper films on Parylene N and SiO_2 substrates.* Journal of Applied Physics, 2003. **93**(2): p. 919-923.

18. Lee, J.H., et al., *Microstructure and adhesion of Au deposited on Parylene C substrate with surface modification for potential immunoassay application.* IEEE Transactions on Plasma Science, 2004. **32**(2): p. 505-509.

19. Seong, J.W., et al., *Effects of ion bombardment with reactive gas environment on adhesion of Au films to Parylene C film.* Thin Solid Films, 2005. **476**(2): p. 386-390.

20. Wu, P.K., et al., *Metal/polymer interface adhesion by partially ionized beam deposition.* Journal of Applied Physics, 1996. **80**(10): p. 5759-5764.

21. Charlson, E.M., E.J. Charlson, and R. Sabeti, *Temperature selective deposition of Parylene C.* IEEE Transactions on Biomedical Engineering, 1992. **39**(2): p. 202-206.

22. Vaeth, K.M. and K.F. Jensen, *Transition metals for selective chemical vapor deposition of Parylene-based polymers.* Chemistry of Materials, 2000. **12**(5): p. 1305-1313.

23. Mariella, R.P., S.W. Steinhauser, and A.C. Diebold, *Dry process ultraviolet patterning of paracyclophane to polyparaxylylene.* Journal of Vacuum Science & Technology B, 1987. **5**(5): p. 1360-1363.

24. Callahan, R., G. Raupp, and S. Beaudoin, *Etching Parylene-N using a remote oxygen microwave plasma.* Journal of Vacuum Science & Technology B, 2002. **20**(5): p. 1870-1877.

25. Callahan, R.R.A., et al., *Downstream oxygen etching characteristics of polymers from the Parylene family.* Journal of Vacuum Science & Technology B, 2003. **21**(4): p. 1496-1500.

26. Callahan, R.R.A., G.B. Raupp, and S.P. Beaudoin, *Effects of gas pressure and substrate temperature on the etching of Parylene-N using a remote microwave oxygen plasma.* Journal of Vacuum Science & Technology B, 2001. **19**(3): p. 725-731.

27. Nowlin, T.E. and D.F. Smith, *Surface characterization of plasma-preated poly-p-xylylene films.* Journal of Applied Polymer Science, 1980. **25**(8): p. 1619-1632.

28. Egitto, F.D., *Plasma-etching and modification of organic polymers.* Pure and Applied Chemistry, 1990. **62**(9): p. 1699-1708.

29. Standaert, T., et al., *High-density plasma patterning of low dielectric constant polymers: A comparison between polytetrafluoroethylene, Parylene-N, and poly(arylene ether).* Journal of Vacuum Science & Technology A-Vacuum Surfaces and Films, 2001. **19**(2): p. 435-446.

30. Yeh, J.T.C. and K.R. Grebe, *Patterning of poly-para-xylylenes by reactive ion etching.* Journal of Vacuum Science & Technology A-Vacuum Surfaces and Films, 1983. **1**(2): p. 604-608.

31. Majid, N., S. Dabral, and J.F. McDonald, *The Parylene-aluminum multilayer interconnection system for wafer scale integration and wafer scale hybrid packaging.* Journal of Electronic Materials, 1989. **18**(2): p. 301-311.

32. Zahn, J.D., Gabriel, K.J. and Fedder, G.K. *A direct plasma etch approach to high aspect ratio polymer micromachining with applications in bioMEMS and CMOS-MEMS*. in *MEMS 2002*. Las Vegas, Nevada.

Chapter 3

Microfluidic Chip Calorimeters for Biochemical Reactions

3.1 Introduction

Calorimeters have been very popular tools for the study of biomolecular interactions, intermolecular structure and enzyme kinetics [1-3]. These three topics are essential to understand biological systems. Specifically, virtually all biological processes depend on the biomolecular interactions and measuring their thermodynamic characteristics in of central importance in biochemistry. Figure 3-1 shows the biomolecules and the interactions between them that can be investigated with calorimeters. Only calorimetry can give direct and complete measurement of the thermodynamic characteristics of these interactions; such characteristics include enthalpy, entropy, free energy, binding constant and stoichiometry. Calorimetry does not require any sample preparation such as labeling or immobilization of sample; thus, measurement is easy and direct. Fundamentally, calorimetry measures the heat evolution which is ubiquitous in biochemical reactions. Therefore, calorimetry can be a universal tool for analyzing biological interactions.

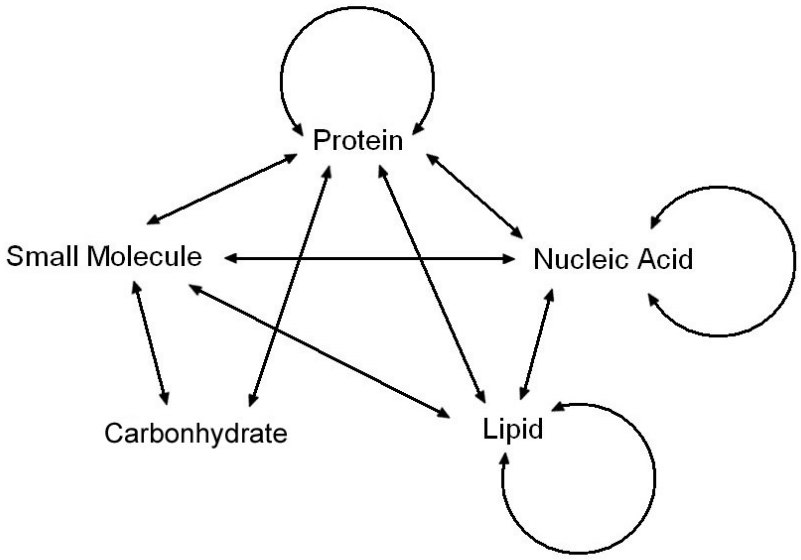

Protein – includes proteins, enzymes, and peptides
Small molecule – includes drugs, inhibitors, substrates, metals, and other small molecules.
Carbohydrate – includes sugars, starch, heparin, other simple and complex carbohydrates
Lipid – includes fatty acids, membranes, vesicles, and other lipids
Nucleic acid – includes DNA, RNA, PNA, and oligonucleotides

Figure 3-1. Biological interactions (shown as the arrows) between biomolecules.

There are many types of calorimeters that can be used in biological science. ITC, for example, measures the binding affinity, stoichiometry, and heat of interaction [3-10]. This data can be used to understand the driving forces and structural mechanism of biological interactions. DSC measures the thermal stability and the heat capacity of molecular structure [11-15].

Recent developments in calorimetry have largely focused on increasing the throughput with smaller sample volume. As mentioned in Chapter 1, miniaturized chip

calorimeters have shown the possibility of high-throughput measurement with nanoliter-scale sample volume. Miniaturization also gives many other benefits such as low cost, portability and integration with other sensor elements. However, the existing chip calorimeters are still limited by sensitivity and/or reliable sample handling.

In this chapter, we describe the fabrication and operation of chip-based conduction calorimeters that overcome these difficulties. An on-chip vacuum insulation greatly improves the sensitivity, and thin-film Parylene microfluidic systems combined with PDMS pneumatic microfluidic controls enable precise control of picoliter-scale samples.

3.2 Device Design

3.2.1 Overall Device Structure

The device consists of three main structures: The microfluidic system, the vacuum thermal insulation and the thermometer (Figure 3-2).

The microfluidic system consists of the structural Parylene microfluidic part and the PDMS microfluidic control part. The reaction chamber and injection channels are built with Parylene thin-film microfluidics to reduce the device heat capacity and enhance the thermal insulation. The PDMS microfluidic channels are connected to the Parylene channels to incorporate microfluidic pumps and valves. PDMS microfluidic chip and associated tubing is shown In Figure 3-3.

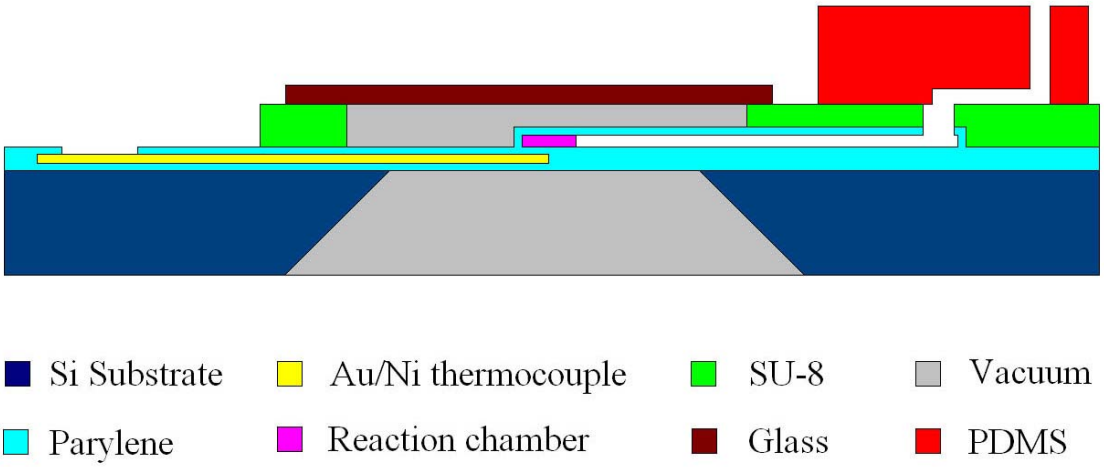

Figure 3-2. Cross-sectional view of the device.

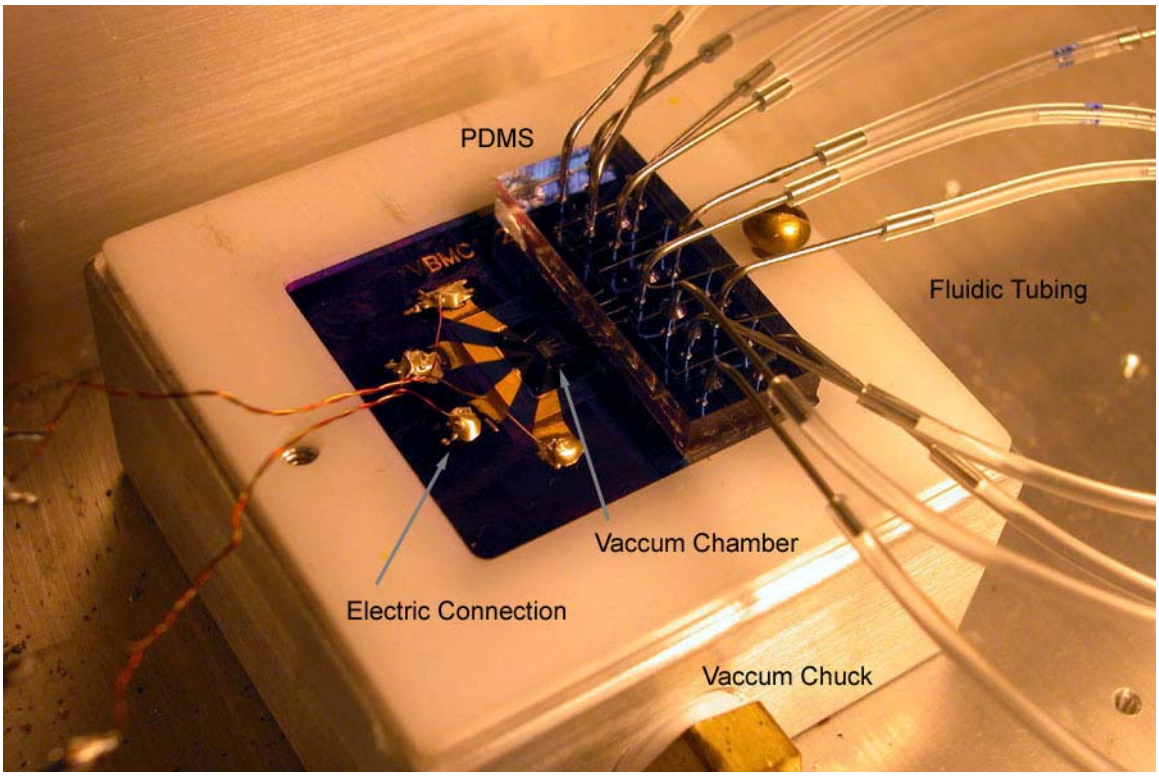

Figure 3-3. Device mounted on vacuum chuck.

The reaction chamber is surrounded with vacuum insulation. The on-chip vacuum chamber structure is built with SU-8, rather than placing the entire device into a vacuum chamber. The thermopile, encapsulated between Parylene layers, measures the temperature difference of the reaction chamber and the substrate, which serves as temperature reference. The device is put on the vacuum chuck, which is held inside a temperature controlled metal box to shield from electrical and thermal noise.

3.2.2 Microfluidic System

3.2.2.1 Parylene Microfluidic Channels and Chamber

The microfluidic structure, which consists of channels and a reaction chamber, is built on a suspended Parylene membrane to provide good thermal insulation (Figure 3-4). The reaction chamber is located at the center of the Parylene membrane and 4 fluidic channels are connected to the chamber to inject and purge sample. The chamber radius is 200 μm and the height is 15 μm. The channel width is 20 μm at narrowest region and 100 μm at widest region. The channel height is 15 μm.

The specific methods of operating the calorimeter, such as fluidic mixing scheme, may vary according to the measurement objective. In a typical operation, two different samples are injected into the reaction chamber along two separate channels. After the measurement, the reaction chamber is flushed with water or buffer solution in the third channel, and the fourth channel is used as an outlet.

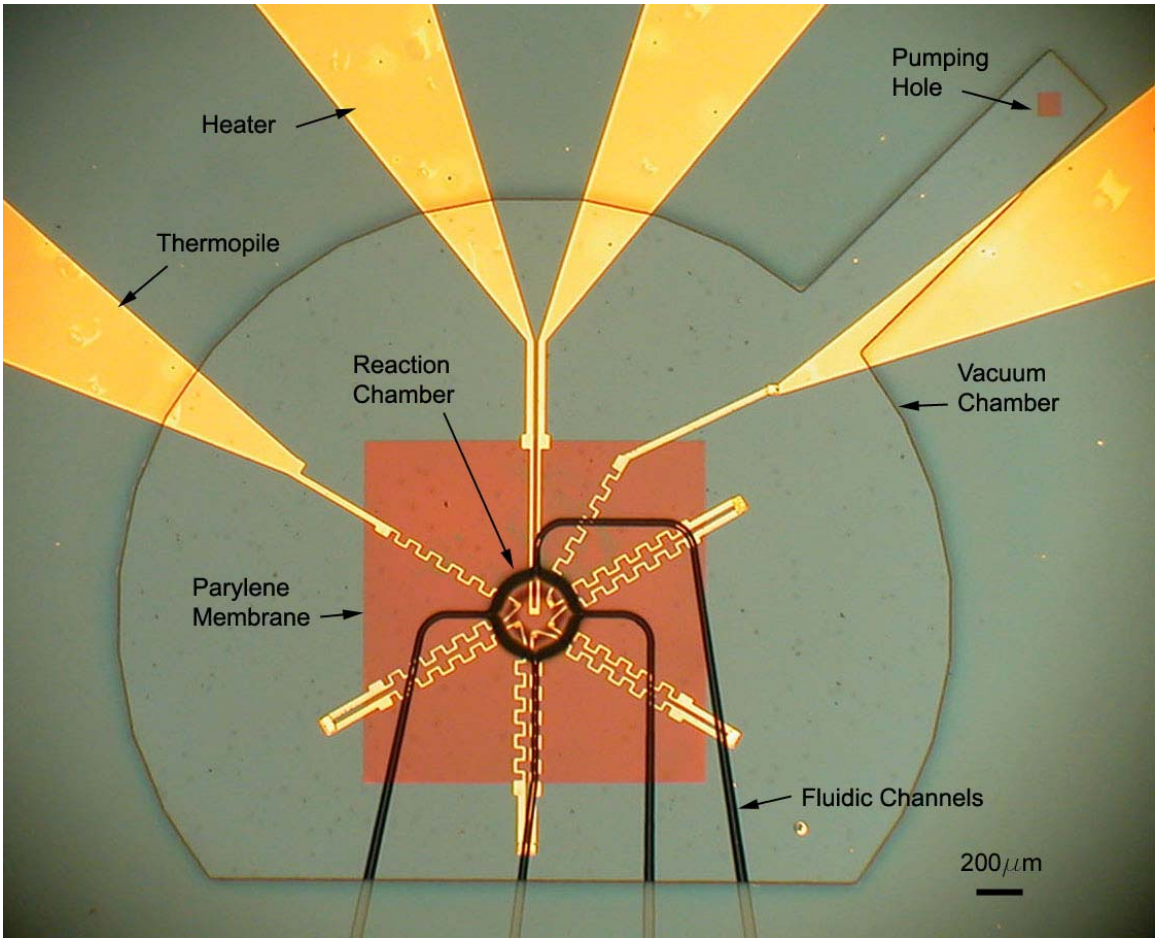

Figure 3-4. Reaction chamber on Parylene membrane.

In the process of developing a chip calorimeter, it is very challenging to scale the heat capacity of the device along with the sample volume, yet scaling is critical for sensitivity. In general, closed chamber chip calorimeters suffer not only from poor thermal insulation but also from large heat capacity due to large volume of microfluidic structures compared to the sample volume. Our device employs Parylene microfluidic systems that are ~2 μm thick, and this significantly reduces the device heat capacity. Furthermore, Parylene provides much lower thermal conductance than silicon nitride, which is most commonly used for chip calorimeters. Noteworthy is the fact that the

thermal conductivity of the SiN is ~300 times larger than that of Parylene. In addition, Parylene has many favorable properties such as chemical inertness and biocompatibility.

3.2.2.2 PDMS Microfluidic Control

In spite of all the benefits of Parylene's material properties, Parylene has not yet drawn as much attention as a microfluidic material. The principal reason is that Parylene is not as compliant as PDMS, thus, it is more difficult for realizing valves or pumps [16, 17]. Early microfluidic systems have been built on rigid substrates such as silicon wafers or glass. The difficulty of making a valve that seals well was the major hurdle in the field until this problem was solved by the development of the PDMS pneumatic valve. In this work, we have combined PDMS microfluidic valves and pumps with Parylene microfluidic channels (Figure 3-3 and 3-5). The PDMS microfluidic systems provide the fluidic control with ease and accuracy while the Parylene microfluidic systems serve as the main structure of the calorimeter. The PDMS microfluidic structure also makes it easy for "micro" channels to couple with "macro" tubing.

Since Parylene coatings are conformal, the surface of the device is not flat after the fluidic structure is made. To put the PDMS microfluidic channels on top of the Parylene channels, the device surface is, thus, planarized with thick SU-8 (Figure 3-2). The PDMS fluidic channels are then aligned on the Parylene channel openings and cured further for bonding to SU-8.

PDMS peristaltic pumps and valves are used to control the sample flow. Separate from the peristaltic pump, the injection pumps are built to inject set volume of samples into the chamber. These are basically the same as the large area valves that work by

displacing the specific amount of liquid in the channel. A conventional two-layer PDMS microfluidic system is used to build pumps and valves. In Figure 3-5, the control lines and the flow lines are shown. Different volumes of sample injections can be made by closing the four 700 pL volume injection pumps sequentially.

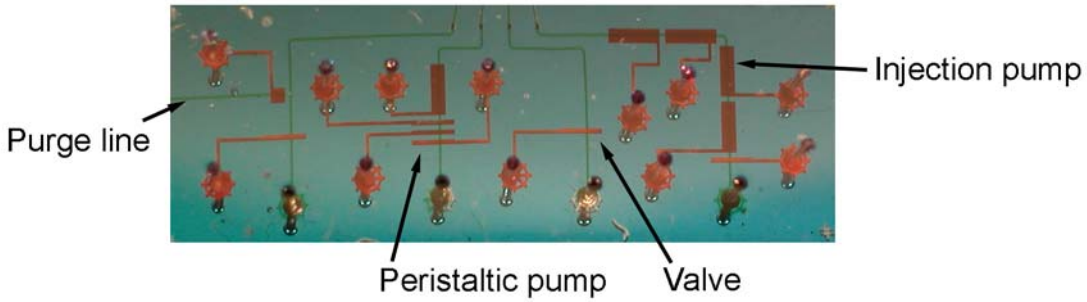

Figure 3-5. PDMS microfluidic flow channels and control channels

Combining Parylene with PDMS microfluidic systems provide other benefits. Calorimeter operations such as injection can be easily modified by replacing the PDMS fluidic control. Additional functions, such as sample dilution, can be added for on-chip sample preparation. More importantly, the calorimeter can be integrated with other microfluidic sensors to construct lab-on-a-chip devices capable of multiple microfluidic analysis of chemical and biological materials.

3.2.3 Vacuum Insulation

3.2.3.1 Structure

For picoliter- to nanoliter-scale sample volumes, the surface-to-volume ratio of the sample becomes significant and results in a large heat loss. In this situation even the surrounding air becomes a significant source of heat loss. Therefore, to improve the thermal isolation of chip calorimeters, it is necessary to employ vacuum insulation, which is never realized by the up-to-date chip calorimeters even though it is common for conventional calorimeters. We built an on-chip vacuum chamber surrounding the Parylene fluidic structure. Parylene has very low gas permeability and good mechanical strength, and these attributes enable us to apply vacuum across the thin-film microfluidic channel walls. We find that 2 μm thick Parylene layer provides enough mechanical strength and physical isolation of the sample under vacuum.

As shown in Figure 3-2, the on-chip vacuum chamber has two regions. The region above the Parylene membrane is defined by SU-8 on the side and a glass ceiling. The same SU-8 for the planarization of the device surface is used to build the vacuum chamber. The region below the membrane, formed by KOH etching for SiN membrane, is sealed with the vacuum chuck. The small membrane shown in the upper right corner of Figure 3-4 was removed to pump the upper region.

3.2.3.2 Reaction Chamber Volume: Calculation

The volume of the reaction chamber is ~1.9 nL without vacuum. Under measurement conditions, the chamber tends to inflate due to the pressure difference

generated by the vacuum and its total volume increases. Figure 3-6 clearly shows the difference of the chamber shape with and without the vacuum; under vacuum, the chamber is seem to balloon out and looks like a convex lens.

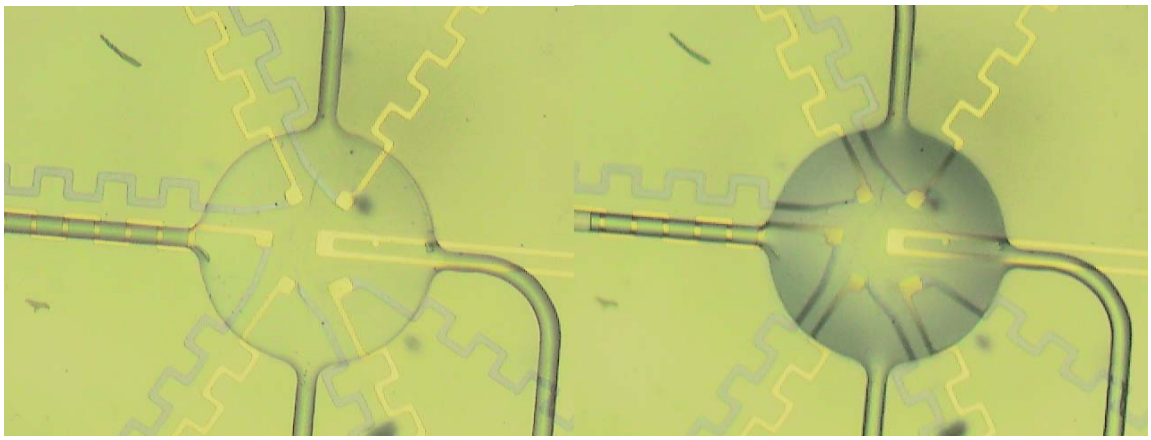

Figure 3-6. Chamber volume change without vacuum (left) and with vacuum (right).

We estimated volume change after vacuum pumping via theoretical calculations and computer simulations. The displacement (z direction) of circular membrane due to a constant force on its surface can be represented by

$$w(r) = \frac{q}{64D}(a^2 - r^2)^2 \tag{3-1}$$

where q is load of intensity, a is radius of membrane and $D = Eh^3/12(1-\nu^2)$ is the flexural rigidity. E is modulus of elasticity, h is thickness, and ν is Poisson ratio. The load of intensity q is similar to an even density of mass on top of the membrane as opposed to a static gas pressure which changes the total amount of force and direction when the membrane deflects.

For Parylene, E = 2.76 GPa, Poisson ratio = 0.4, a = 200 μm, and h = 2 μm. At 1 atm (= 101 kPa = 101325 N/m^2), the deflection at the center is ~1.1mm! Different source gives Young's modulus as big as 4.5 GPa [18]. In this case, the deflection will be reduced to ~0.79 mm. Either case, the deflection of membrane is much larger than we can take as reasonable.

We confirmed this result with finite element simulation of elastic material deformation. We used FEMLAB for the simulation. The chamber is modeled as in Figure 3-7. The wall thickness is 2 μm. The height of reaction chamber is 15 μm and the radius is 200 μm. Applying 1 atm pressure across the wall, we get maximum 1.28 mm displacement at the center (Figure 3-8).

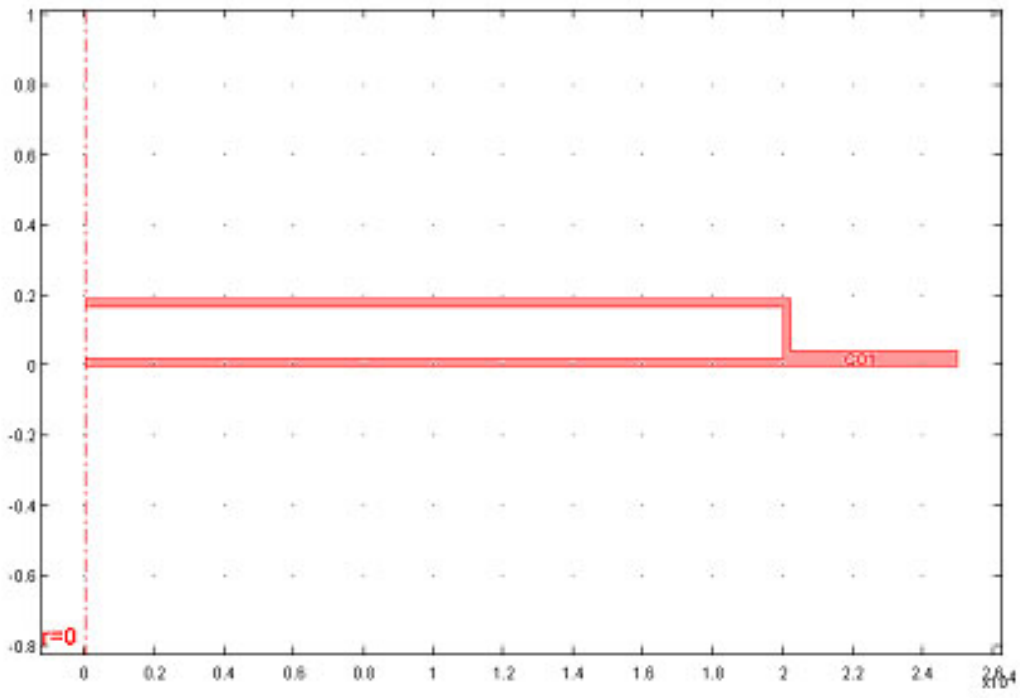

Figure 3-7. Cross-sectional view of the simulation model in cylindrical coordinate.

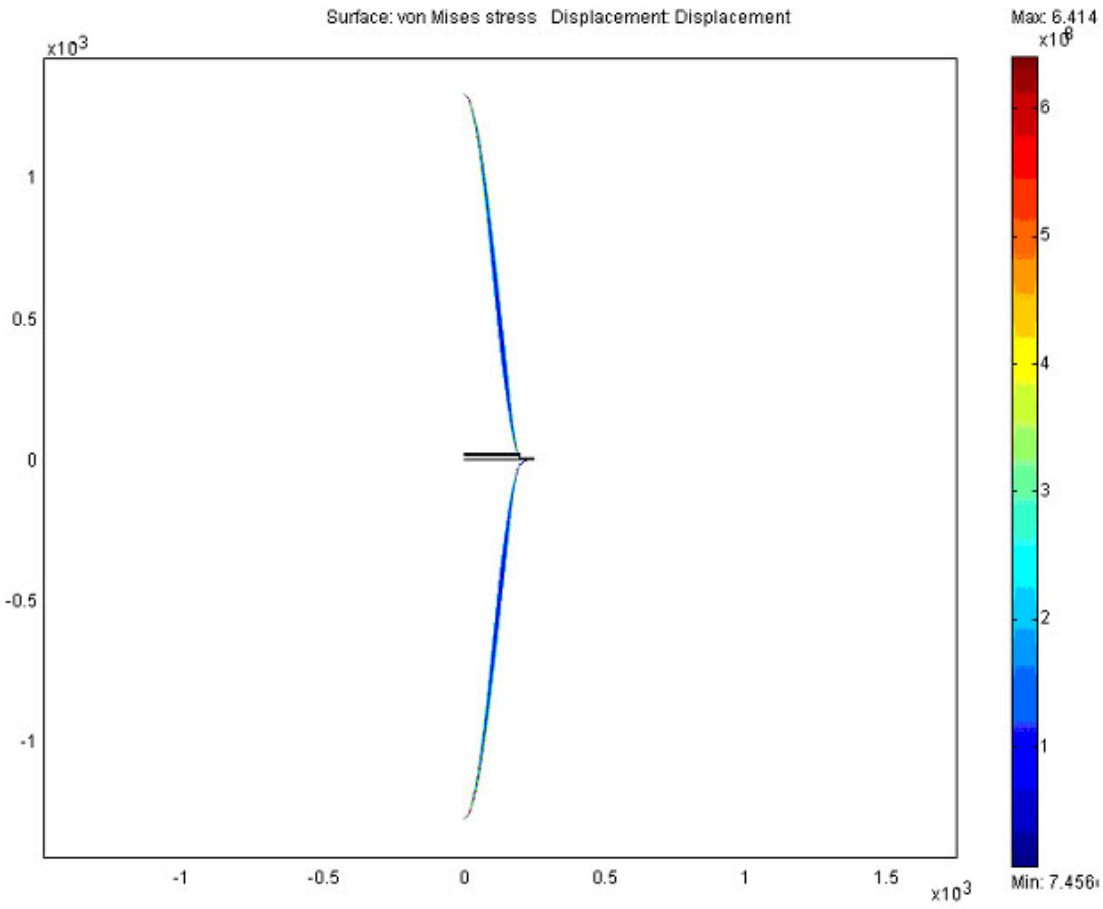

Figure 3-8. Membrane deflection simulation result. Deformed membrane is shown in color.

This result clearly does not agree with the real observation. The displacement at the center can be at most ~80 μm because of the glass ceiling. And we did not observe the chamber touching the ceiling. Moreover, the Parylene film will break before it stretches this far; Parylene's elongation-to-break value is ~200%. The chamber deformation is expected to be far beyond the elastic region. Thermoplastics, such as Parylene, have rather large plastic deformation range. Therefore, it can withstand the large loading without fracturing (Figure 3-9).

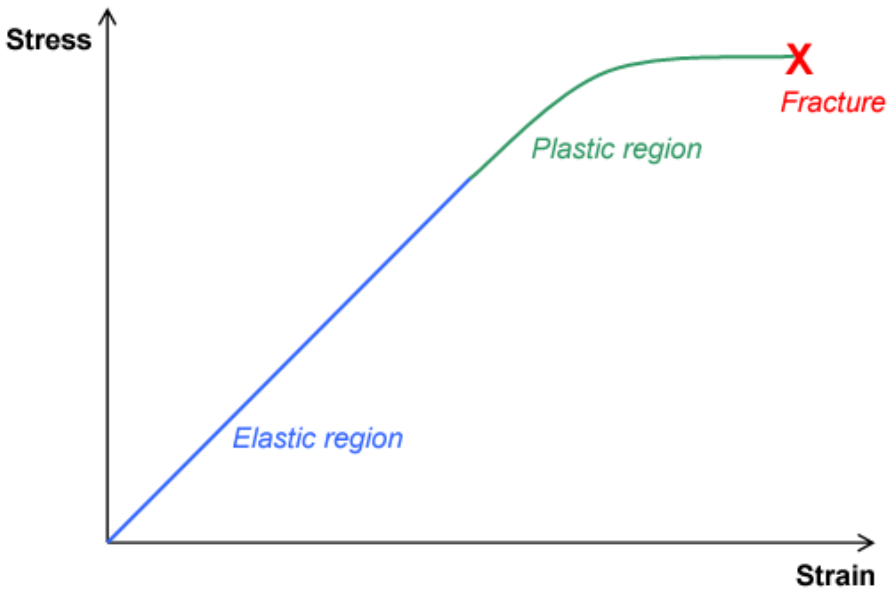

Figure 3-9. Stress–strain curve.

Parylene's properties are known to change with aging and annealing [19]. Because of the need for photoresist baking, the device goes through many heating/cooling cycles during the fabrication processes. The typical temperatures for photoresist baking (~100 ºC) exceed the glass transition temperature of Parylene (~80 ºC). Thermal cycling over the glass transition temperature is, in effect, equivalent to annealing Parylene. This results in an increased modulus and intrinsic stress of the Parylene layers. We believe this annealing effect is also part of the reason that we observe smaller deformation than expected.

It is worth noting that the deflection is proportional to area^4. When the chamber radius decreases the chamber expansion will decrease dramatically. For example, for 30 μm wide channel, no significant volume change was observed.

3.2.3.3 Reaction Chamber Volume: Measurement

The chamber volume was measured in following way. First, the chamber and part of channels are filled with water so that the water–air boundaries are located within the Parylene channels. When the chamber volume changes, the positions of these water–air boundaries also changes. The amount of water displaced along the channels is measured when the chamber expanded under vacuum (Figure 3-10). The channels have a much smaller cross-sectional area and their volume changes are neglected.

In Figure 3-11, the positions of the water–air boundaries in the channels are shown. The pictures taken before applying vacuum are cut and pasted over the pictures taken after applying vacuum. The black arrows indicate the locations of water–air boundaries before applying vacuum and the white arrows indicate the locations after applying vacuum. The volume of displaced water calculated from the channel volume was ~1.6 nL.

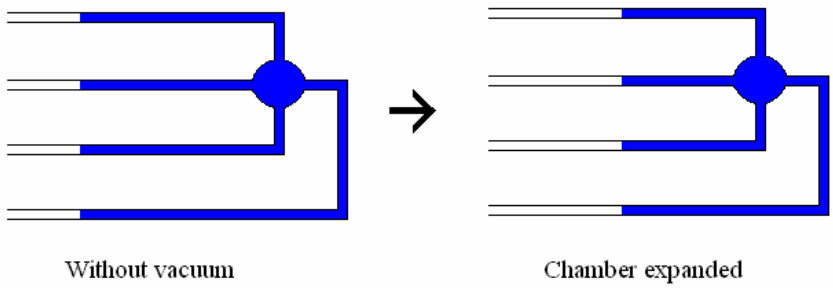

Figure 3-10. Chamber volume measurement schematic.

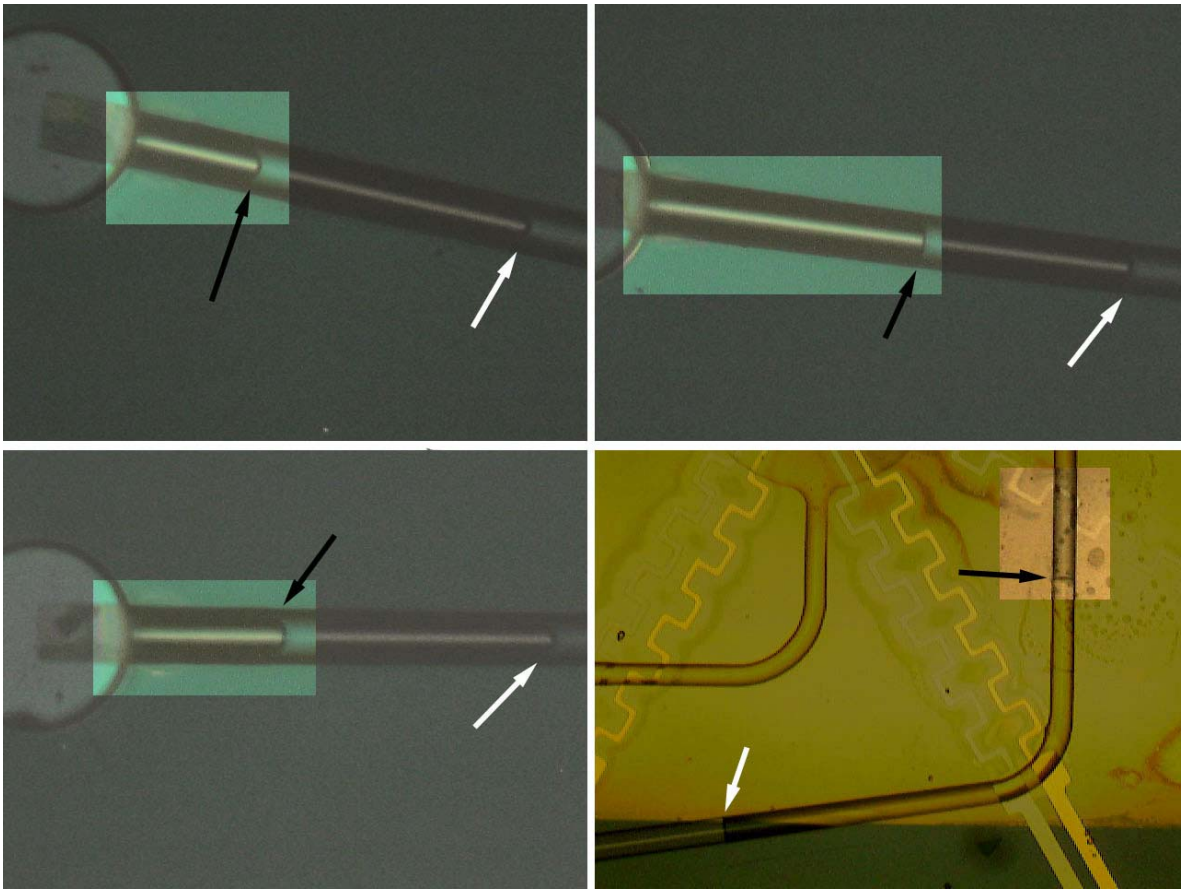

Figure 3-11. Water–air boundaries. Brighter region is the picture taken before applying vacuum.

The volume without vacuum is the same as the volume defined by sacrificial photoresist, which is 1.9 nL. The total volume after applying vacuum is ~3.5 nL. The chamber volume is slightly different from device to device due to variations in the fabrication steps.

3.2.4 Thermopile and Heater

The gold-nickel thin-film thermopile is fabricated on the Parylene membrane (Figure 3-4) to measure the temperature change associated with processes under study

within the microfluidic chamber. Five thermocouple junctions are connected in parallel to provide a ~110 μV/K temperature coefficient (total Seebeck coefficient). The gold-nickel metallic thermopile is chosen for fabrication convenience and low 1/f electrical noise. However, substitution of a thermopile with materials higher Seebeck coefficient can improve temperature sensitivity. For example, antimony and bismuth pair can substitute for the gold and nickel pair to provide ~6 times larger Seebeck coefficient. Seebeck coefficients of various metal and semiconductor elements are listed in table 3-1.

Table 3-1. Seebeck coefficient of materials [20]

Material	Seebeck Coefficient (μV/K)	Material	Seebeck Coefficient (μV/K)	Material	Seebeck Coefficient (μV/K)
Aluminum	3.5	Gold	6.5	Rhodium	6.5
Antimony	47	Iron	19	Selenium	900
Bismuth	-72	Lead	4.0	Silicon	440
Cadmium	7.5	Mercury	0.6	Silver	6.5
Carbon	3.5	Nichrome	25	Sodium	02.9
Constantan	-35	Nickel	-15	Tantalum	4.5
Copper	6.5	Platinum	0	Tellurium	500
Germanium	300	Potassium	-9.0	Tungsten	7.5

The total electrical noise (referred to input) with low-noise amplifier was ~10 nVrms/√Hz at 0.1 Hz. The measurement sensitivity with 1Hz bandwidth is 30 nV for a 3 to 1 signal-to-noise ratio. This corresponds to a temperature sensitivity of 0.27 mK. A

gold resistive heater is co-fabricated on the device to permit calibration of its thermal conductance. These electrical components are embedded within the Parylene layers and are isolated from the liquid samples.

3.3 Fabrication

Step by step details of the device fabrication processes are shown in Figure 3-12. The fabrication requires Parylene microfabrication as well as standard microfabrication techniques such as optical lithography.

First, a 1.5mm square SiN membrane is built from a double side polished SiN wafer to make a suspended Parylene membrane. On the back side of the wafer, SiN is patterned with photoresist and etched by RIE. Then SiN membrane is suspended on the front side with KOH silicon wet etching (Step 1). 1 μm thick Parylene is deposited on the SiN membrane with PDS 2010 LABCOTER 2, Parylene coater. An adhesion promoter, A-174 Silane, is applied to the wafer prior to the Parylene deposition (Step 2). The thermometer and resistive heater are made from 80 nm thick nickel and 60 nm thick gold, which are e-beam evaporated onto the Parylene layer. 4 nm thick titanium is evaporated as an adhesion underlayer for both nickel and gold. They are patterned by photolithography and chemical wet etching (Step 3). On top of the electrical components, the 1μm thick second Parylene layer is deposited to passivate the surface and to protect the electric circuit (Step 4).

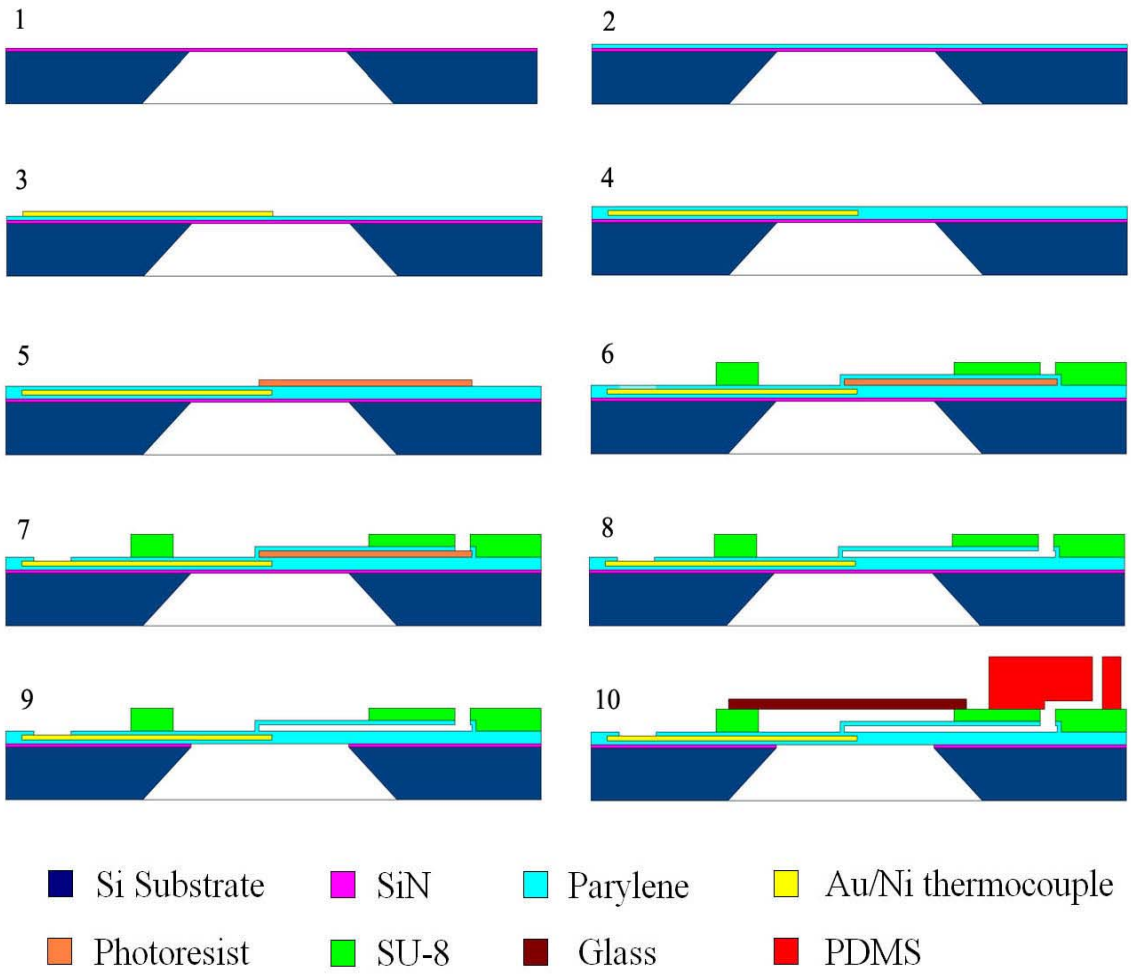

Figure 3-12. Fabrication steps. 1. SiN membrane, 2. first Parylene layer, 3. thermopile and heater, 4. second Parylene layer, 5. photoresist sacrificial layer, 6. third Parylene layer and SU-8, 7. parylene etching, 8. photoresist removal, 9. backside SiN removal, 10. glass seal and PDMS.

The Parylene microfluidic system is built in the conventional method. A thick sacrificial photoresist layer (AZ 9260) is spin coated for 15 μm thick structures. The photoresist layer is exposed to UV and developed to form the microfluidic structure (Step 5). The third Parylene layer, 2 μm thick, is deposited on the photoresist structure to build the Parylene microfluidic channel wall. The 80 μm thick SU-8 structure is built by

photolithography on top of the Parylene microfluidic structure. The purpose of the SU-8 structure is to planarize the device surface and to construct the vacuum chamber (Step 6). Sometimes, the SU-8 intrinsic stress breaks the parylene channel. To avoid this problem, SU-8 was cured at lower temperature (55 ºC).

Several etching steps follow the SU-8 patterning. First, the Parylene covering the electrical contact area is etched by oxygen RIE (150 mT, 140 W). Photoresist is used as mask for etching. In the same way, the microfluidic channel opening area is etched (Step 7). The photoresist filling inside the channel is removed using propylene glycol methyl ether acetate (PGMEA). This step typically takes about 36 hours with the solvent heated to ~40ºC (Step 8). Finally, the Parylene membrane is suspended alone by etching away SiN from backside with CF_4 plasma (120 mT, 140 W) (Step 9). The vacuum chamber region is sealed with a glass slide using UV curable glue. UV curable glue can be used to wet the small gap between glass and SU-8 by capillary force. It does not flow to the vacuum chamber area because the area has larger gap. Once the glue is applied to the area we want, it can be cured by exposed to UV light. This method is a very efficient way to apply glue to a selective region. Finally, the PDMS microfluidic control is built and put on the SU-8 region. It is baked (80 ºC) overnight to fully cure (Step 10).

3.4 Device Calibration

3.4.1 Thermometer Response to Joule Heating

The calorimeter response to applied power can be represented with the heat balance equation of a simple body, Equation (1-29).

$$C\frac{dT(t)}{dt}+G[T(t)-T_0(t)]=\frac{dQ(t)}{dt}$$

One can calculate the heat capacity and thermal conductance of the calorimeter from the material properties and geometry of the calorimeter. However, in reality this process is not simple and the calculation often gives large discrepancies from the measured value. For practical purposes, the heat capacity and the thermal conductance are usually measured directly by applying thermal power to the system.

There are many ways to apply heat to the system. The most often used method is applying Joule heat electrically. Electric heating can be easily controlled and is very accurate. We have calibrated the thermal conductance with the integrated gold resistive heater.

3.4.2 Thermal Conductance: Simulation

We estimate the device thermal conductance with finite element simulations. The model of the device was simplified for several reasons. First, the model has components with large aspect ratio. While the thickness of the metal layer is of order 10 nm, the width is order of 10 μm and the length is order of 1 mm. Calculations for this geometry require a large number of meshes, which then requires long simulation time and often ends up

generating errors due to insufficient memory. Secondly, some details of the device have little effect on the simulation results. For example, the silicon substrate has much larger thermal mass and conductance than the sample and Parylene. With this huge thermal mass and large conductance, it can be treated as a temperature reference. Setting the edge of Parylene membrane as temperature reference or setting the outer face of the silicon substrate gives practically the same result. In other words, the silicon substrate can be removed from simulation. Another example of simplification is the Parylene channel structure. Parylene channel is simplified as membrane structure with double thickness and the water was put on the surface of the Parylene membrane. The thermal conduction along the Parylene membrane is much larger than the conduction in the normal direction. As a consequence, Parylene channel that is contact with water is practically at the same temperature as the water inside. The total thickness of the Parylene layer is an important factor in determining the device thermal conductance, however, the position of layer has little influence on the results.

Only the heat transfer by conduction is considered, because the convection and radiation at this scale is much smaller than conduction.

The simplified model shown in Figure 3-13 has the following geometry: the Parylene membrane is 4μm thick, 1.5 mm square. Metal layer is 12.5 μm wide and 50 nm to 90 nm thick (5 Au-Ni thermocouples, 1 Au heater). The chamber has a radius of 200 μm and height of 30 μm. The channel width is 30 μm and the height is 15 μm. Both the channel and chamber are assumed to be filled with water. The boundaries are 0.1 mm above the membrane and 0.5 mm below the membrane, which are assigned for either air or vacuum. The outer boundary is set to constant temperature, since the surrounding has

to be the temperature reference. A uniform heat source is set in the reaction chamber and a total of 1 μW of power is applied to the chamber.

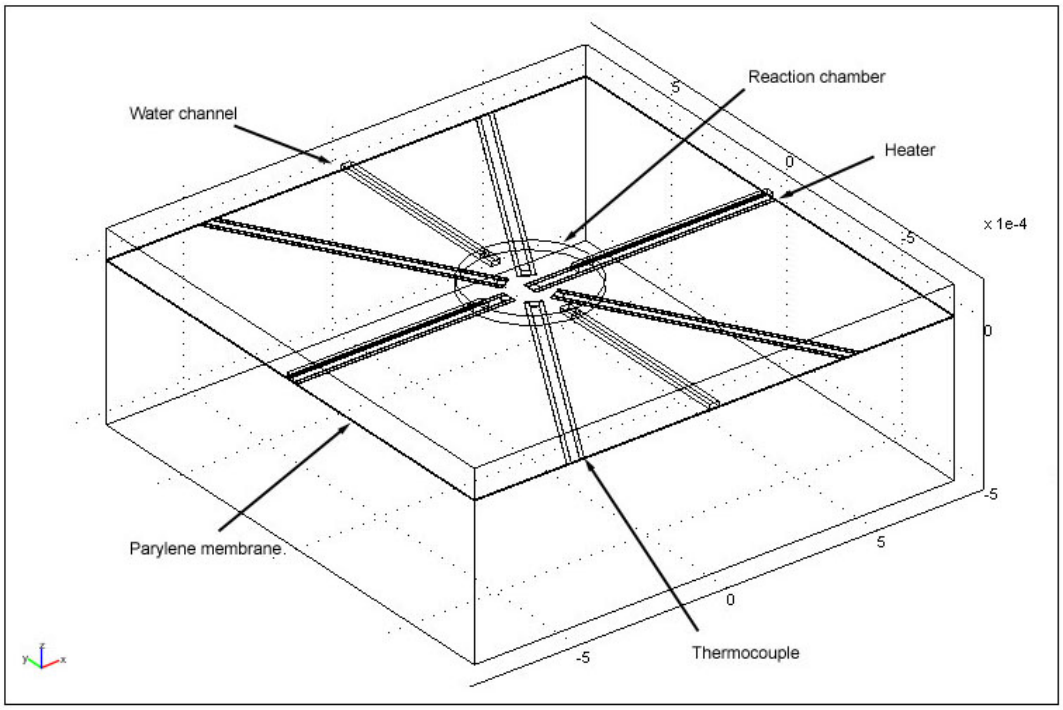

Figure 3-13. Thermal conductance simulation model.

The simulation results with vacuum and air insulation are shown in Figures 3-14 and 3-15. The temperature difference (ΔT) in the chamber gives the thermal conductance (G = 1 μW/ΔT). To make a fair comparison with experimental results, the temperatures at the thermocouple junctions are averaged. As can be seen in the figures, the presence of the air makes a huge difference for a microstructure, even though the air is a fairly good insulator. The maximum temperature change with equal power is ~20 times larger with the vacuum insulation. Though air has a small thermal conductivity, the majority of surface area of the chamber is in contact with air. As a consequence, the thermal

conductance of the surrounding air is much larger than that of the Parylene membrane or metal wires. It is clear that the temperature on the membrane is almost constant in the case of air insulation, which implies that membrane is not playing an important role in thermal transport.

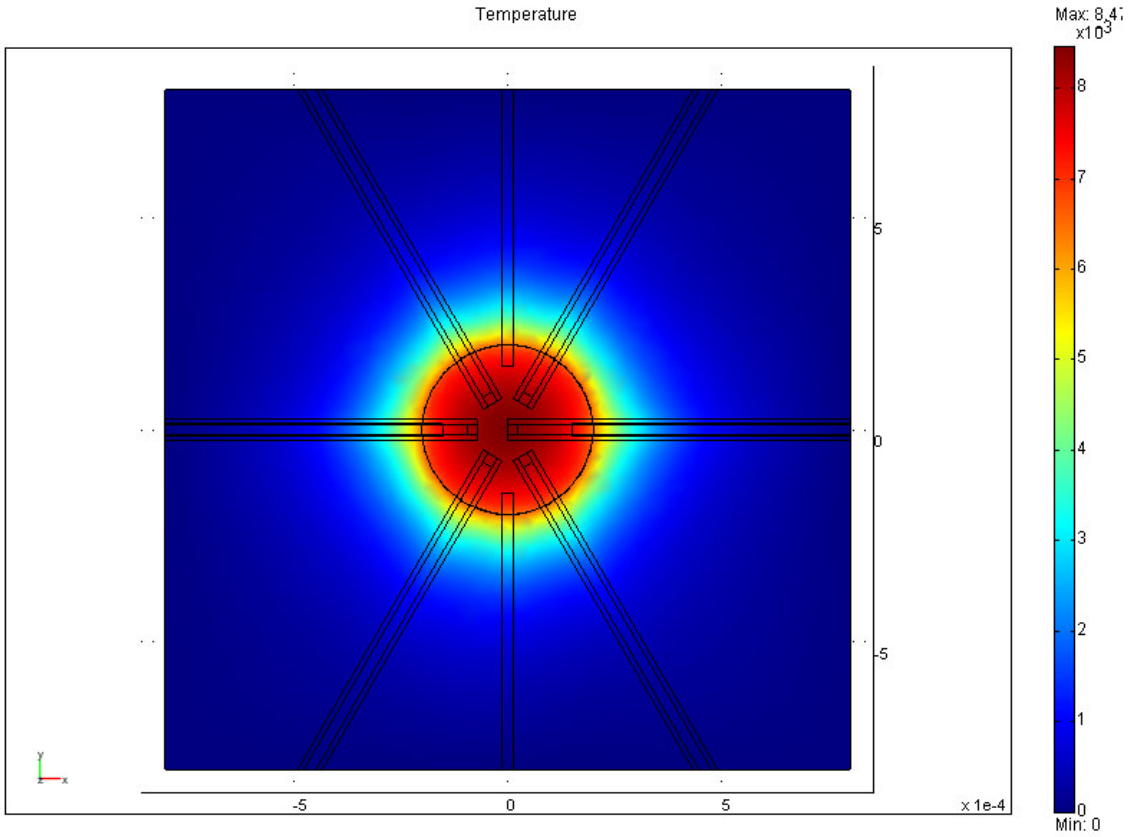

Figure 3-14. Temperature profile without vacuum.

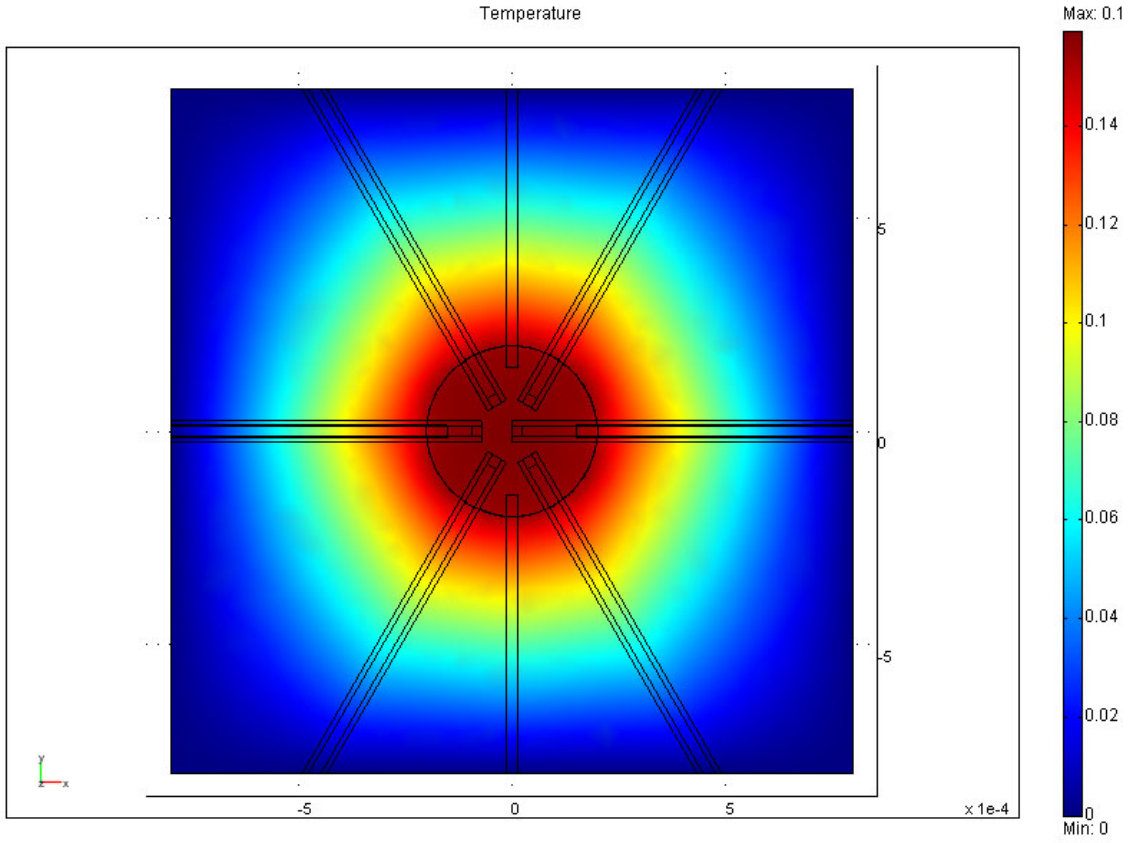

Figure 3-15. Temperature profile with vacuum.

From the results of the simulations, the thermal conductance of the each case is calculated and summarized in Table 3-2. Two different devices with different metal thicknesses are compared. Because gold is more conductive than nickel, the device with thinner gold has a slightly smaller thermal conductance. We can see the thermal conductance is about 20 times smaller with vacuum insulation than with air.

Table 3-2. Thermal conductance with finite element simulation

Thickness (Nickel / Gold)	Conductance (Vacuum)	Conductance (Air)
60 nm / 80 nm	7.25 μW/K	125 μW/K
90 nm / 50 nm	6.33 μW/K	123 μW/K

We have a couple of heat conduction paths, which are metal (gold and nickel), water, Parylene and air. Obviously, without vacuum, most of the contribution is from air. We can calculate the contribution of air from the difference between the two results; about 94% of the total conductance is from the air conduction. Thermal conductance of each part has been calculated to see the contributions of each part. To do this, the simulation is repeated with some parts removed and compared with the previous result. The simulations are done for 60nm thick nickel device with vacuum condition.

Table 3-3. Thermal conductance of each part

	Parylene	Metal	Water
Conductance	1.79 μW/K	3.88 μW/K	1.89 μW/K

Without air conduction, the metals (gold and nickel) contribute about half of the total conductance even though they are very thin. Parylene and water contribute about 25% of the total conductance each. In the actual device, metal wires are designed as serpentine shape to reduce the thermal conductance.

Listed in Table 3-4 are the thermal conductivity and specific heat of the materials used for the simulation. Some insulating materials are also listed for comparison.

Table 3-4. Thermal conductivity and specific heat of materials [21]

	Thermal conductivity (W/m·K)	**Specific heat (J/g· K)**
Gold	320	0.13
Nickel	90.7	0.44
Water	0.58	4.2
PMMA	0.21	1.5
PDMS	0.19	1.46
Polyimide	0.16	1.09
Parylene	0.089	0.71
Air	0.024	1.01
Stainless Steel	0.13	0.48
SiN	16~33	0.17
Si	130	0.71

3.4.3 Thermal Conductance: Measurement

To measure the thermal conductance, the thermoelectric voltage response was measured against the electric power applied by the heater. The calorimeter response to a step function heating is as follows. *T(t)* is the temperature difference between the reaction chamber and the substrate.

$$P(t) = 0, \quad \text{when } t < 0$$
$$= P_0, \quad \text{when } t \geq 0 \tag{3-2}$$

$$C\frac{dT(t)}{dt} + G \cdot T(t) = P(t) \tag{3-3}$$

$$T(t) = 0, \quad \text{when } t < 0$$
$$= \frac{P_0}{G}\left(1 - \exp\left(-\frac{t}{\tau}\right)\right), \quad \text{when } t \geq 0 \tag{3-4}$$

In Figure 3-16, we show the result of applying a square wave heating pulse of 4.04 μW. Before the measurement, the device was put under vacuum (2mTorr) and the reaction chamber was loaded with water.

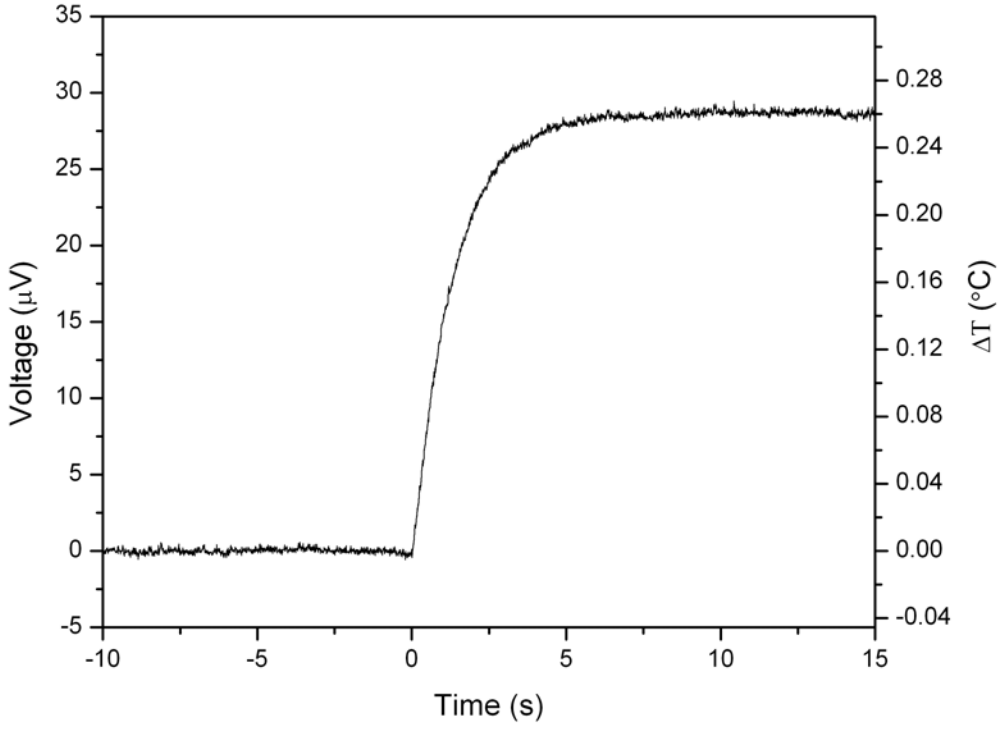

Figure 3-16. Thermometer response to a heating pulse.

Heat power sensitivity is defined as the voltage output over the applied power. In the measured response shown above, it is 7.10 V/W. Because we have ~30 nV voltage sensitivity, the corresponding power sensitivity is ~4.2 nW. The device thermal conductance, the applied power divided by the temperature change, was 15.5 μW/K. The microchip calorimeters developed by various other groups have thermal conductance of on the order of 100 μW/K to 1 mW/K. The deviation of the thermal conductance from one device to another was less than 2 μW/K. The deviation mainly comes from the Parylene thickness which can not be controlled precisely with the deposition process employed in this work.

The exponential increase can be linearized and fitted to give the thermal relaxation time constant. From Equation (3-4),

$$V(t) = S \cdot T(t) = S \cdot \frac{P_0}{G}\left(1 - \exp\left(-\frac{t}{\tau}\right)\right), \qquad \text{when } t \geq 0 \tag{3-5}$$

By subtracting $\frac{S \cdot P_0}{G}$ and multiplying by -1

$$\ln(V'(t)) = \ln\left(\exp\left(-\frac{t}{\tau}\right)\right) = -\frac{1}{\tau}t \tag{3-6}$$

In Figure 3-17, $\ln(V'(t))$ is plotted from 0 to 6.5 s. The slope of the line is equal to $-\frac{1}{\tau}$. The device thermal relaxation time constant from the fitting is 1.33s. Since $\tau = \frac{C}{G}$, the heat capacity of the device with water in the chamber can be calculated. By putting in the numbers, we get the heat capacity, 20.6 μJ/K. 3.5 nl of water has 14.7 μJ/K heat capacity. The difference, 5.9 μJ/K, is the device heat capacity.

The heat capacity of the Parylene membrane can be calculated from the volume and it is 8.24 μJ/K. Since not all the membrane is subject to the same temperature change, the measured device heat capacity is close to the calculated value.

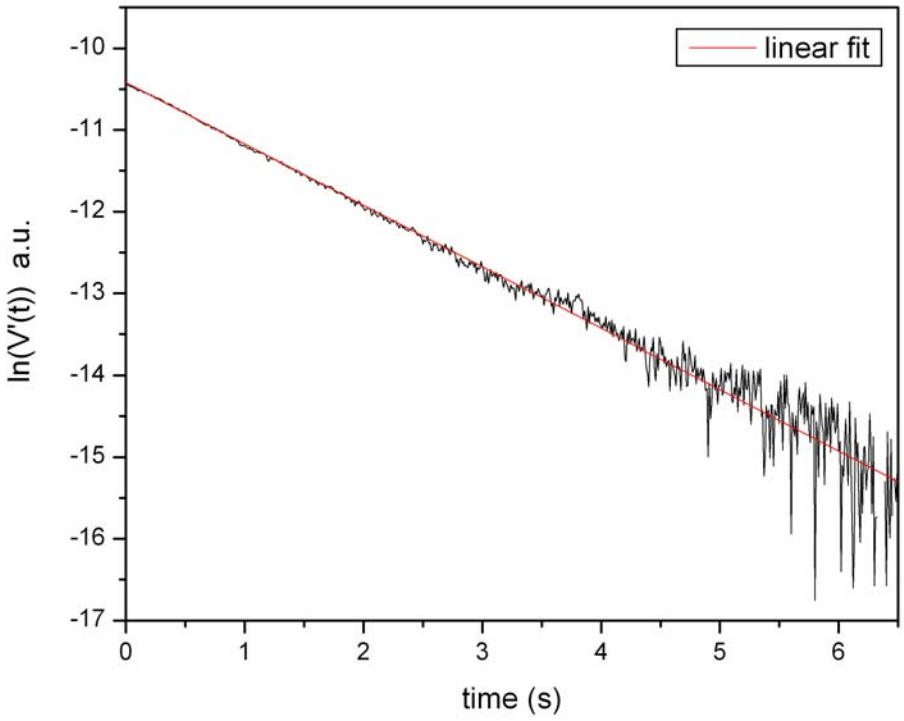

Figure 3-17. Linearized response.

We have measured the thermal conductance of the device at different pressure. Figure 3-18 shows the results. The thermal conductance of the device decreases with pressure and reaches its minimum around 1 mTorr. Below 1 mTorr, the thermal transport through air becomes negligible and only the Parylene structure and electrical leads participate in thermal transport. The air conductance contributes about 93% of total

conductance at atmospheric pressure, which agrees with the simulation result. In other words, removing air conductance with vacuum insulation gives 93% reduction in heat loss and ~15 time larger signal.

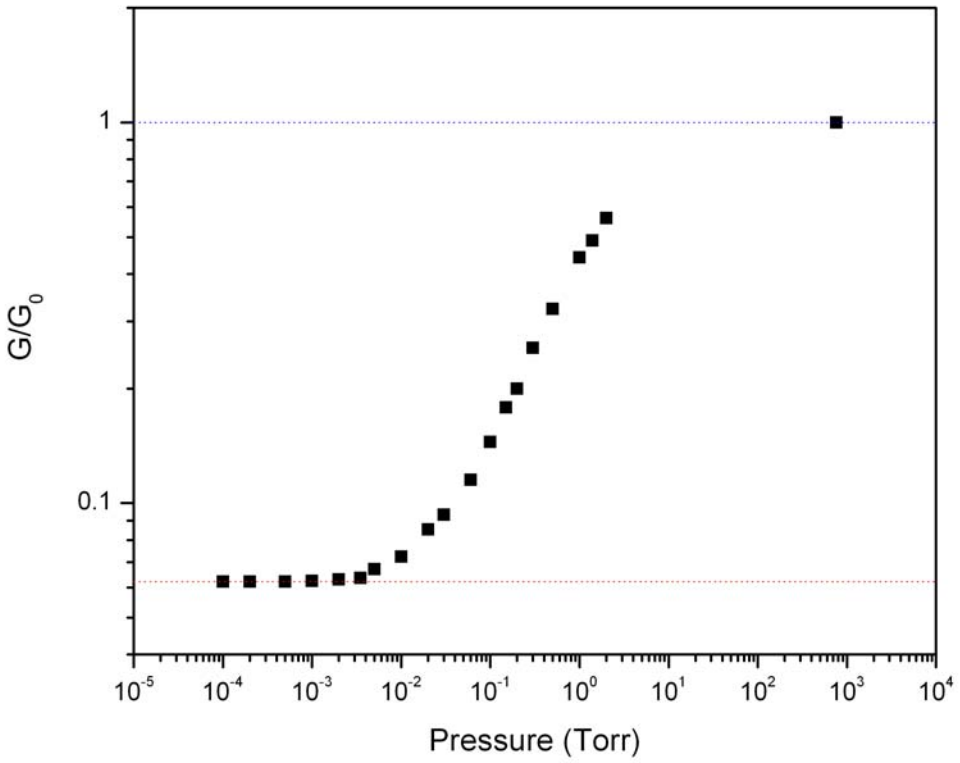

Figure 3-18. Thermal conductance vs. pressure

Finite element simulations estimated the device thermal conductance to be ~ 7 μW/K. Actual measurements returned a larger value, 15.5 μW/K. This mismatch is in part from the fact that we simplified the model to obtain a qualitative estimation of device

performance. We believe the main reason for the larger thermal conductance than the estimation is due to the change of Parylene properties arising in the fabrication process. The modulus and intrinsic stress of the Parylene appear to change significantly when annealed. Annealing also changes the thermal properties because they are closely related to its crystallinity. There seems to be a significant change in the thermal conductivity of the Parylene during the heat cycle involved in fabrication processes. Further investigation to verify this is required.

3.5 Measurements

To demonstrate the performance of calorimeter we performed measurements on two exothermic reactions: the mixing of methanol with water and the hydrolysis of urea with urease.

3.5.1 Calorimetric Measurement of Methanol Dilution

3.5.1.1 Background

When two different liquids are mixed, there is an accompanying change of total free energy, entropy, and enthalpy change. In a mechanical mixture, the free energy of the total mixture is simply the sum of its two components. In contrast to a mechanical mixture, a solution is considered as a mixture of atoms or molecules. In general there is enthalpy change associated with the change in near neighbor bonds, therefore mixing of two different liquids will either liberate, or absorb heat. This is called heat of mixing,

ΔH^M, which is defined as the change in enthalpy per mole of mixture when the pure components are mixed at constant temperature and pressure. Sometimes it is called excess enthalpy of mixing. Heat of mixing is identical to the excess enthalpy of mixing per mole of mixture, ΔH^E.

The heat of mixing of alcohol and water has been studied for long time. Measurements have been carried out [22, 23] and computer simulations of the mixing [24] have also been done recently. In Figure 3-19, value of the heat of mixing for three alcohols and water is shown. Methanol and ethanol give exothermic reactions only, while isopropanol can give both endothermic and exothermic reactions depending on the ratio of mixing. We employ methanol because its curve is the smoothest, so it is easy to interpolate the ΔH^M values.

Table I. Experimental Excess Enthalpy Values at 25° C.

Methanol-Water (1) (2)		Ethanol-Water (1) (2)		Propanol-2-Water (1) (2)	
x_1	ΔH^M, cal. per mole	x_1	ΔH^M, cal. per mole	x_1	ΔH^M, cal. per mole
0.0287	−46.0	0.0132	−29.5	0.0275	−78.0
0.0492	−76.8	0.0172	−38.4	0.0398	−104.8
0.0495	−77.3	0.0367	−78.5	0.0767	−152.4
0.0674	−98.1	0.0772	−141.4	0.1090	−155.9
0.0973	−130.6	0.1442	−181.9	0.1446	−144.4
0.1253	−155.3	0.2288	−172.0	0.2474	−99.8
0.1468	−169.4	0.2861	−155.9	0.3079	−72.8
0.1903	−189.6	0.3366	−138.3	0.4092	−25.9
0.2041	−193.7	0.3468	−138.2	0.4689	−2.75
0.2463	−202.9	0.4018	−123.6	0.5525	22.8
0.3562	−203.7	0.6008	−77.8	0.6074	35.1
0.3955	−201.9	0.7180	−59.6	0.6529	48.8
0.4689	−191.5	0.7314	−55.6	0.7224	50.7
0.5568	−175.4	0.8070	−49.6	0.7559	51.8
0.6598	−151.6	0.8684	−38.4	0.8988	29.6
0.7823	−114.7	0.8774	−38.0		
0.7990	−106.8	0.8807	−35.4		
0.9348	−40.8	0.9487	−18.1		
		0.9596	−14.8		

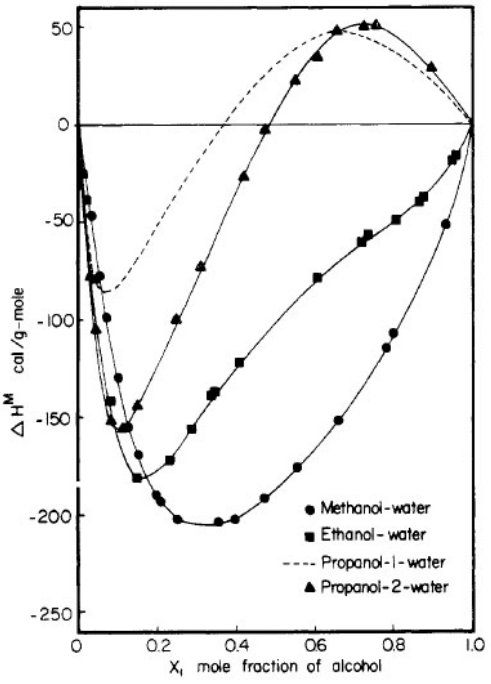

Figure 3-19. Heat of mixing of alcohol-water mixture [23].

3.5.1.2 Measurement

Our heat of mixing measurement is carried out in the following way. The calorimeter chamber is filled with water and 700 pL of 14.7% methanol-water mixture is injected into the chamber. The vacuum chamber was evacuated and stabilized for 30 minutes before the measurement to avoid any fluctuations from pumping the vacuum. The electrical measurements are done with a low-noise voltage amplifier and digital oscilloscope to acquire time records. Data points are taken with 1 kHz bandwidth filter and averaged later to represent 4 data points for every second.

The power output from the mixing process is shown in Figure 3-20. The total energy can be simply given by integration and found to be 9.4 μJ; this is slightly smaller than the expected value of 10 μJ [23]. For this particular measurement, the device conductance was 22 μW/K.

The signal increases quickly to its maximum and then decays exponentially with a time constant of 3.6 s. The time record of heat evolution can give us information about how the reaction rate changes with time. For example, the exponential decay may come from the exponential decrease in amount of mixing due to diffusion. However, it is hard to get the exact diffusion constant from this result because the enthalpy change from mixing is not linearly proportional to the amount of methanol mixed.

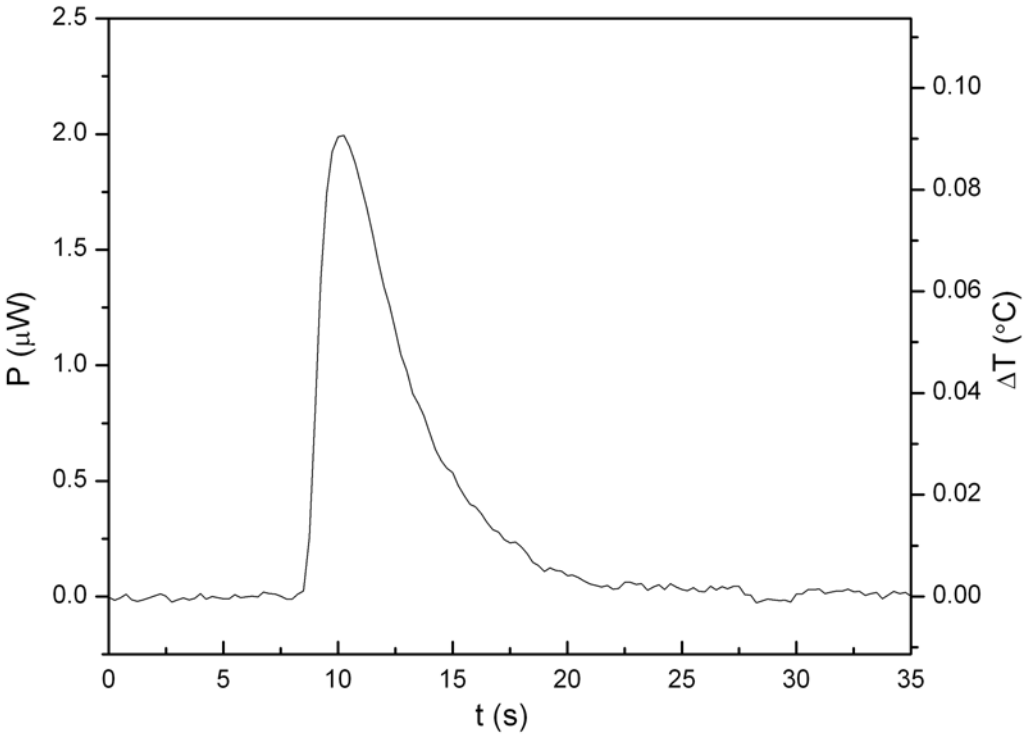

Figure 3-20. Heat of mixing from 700 pL methanol (14.7%) and 2.8 nL water.

3.5.2 Calorimetric Measurement of Urea Hydrolysis

3.5.2.1 Background

Enzymes are large protein molecules that function as catalysts and play a crucial role in nearly all biological processes. Enzymatic decomposition of a substrate can be described as,

$$E + S \underset{k_{-1}}{\overset{k_1}{\rightleftharpoons}} ES \xrightarrow{k_{cat}} E + P$$

The substrate S reversibly associates with the enzyme ***E*** in a first step with rate constant k_1 and k_{-1}, and some of the resulting complex ***ES*** is allowed to break down and yield the product ***P*** and the free enzyme back at rate of k_{cat}.

The initial velocity of the reaction, $V_0 (= \frac{d[P]}{d[t]})$, is given by

$$V_0 = k_{cat}[ES] \tag{3-6}$$

Conditions, [P] << [S] and [E] << [S] are assumed here.

The rate of formation of [ES] is k_1[E][S] and the rate of consumption of [ES] is k_{-1}[ES] + k_{cat} [ES]. So, in the steady state,

$$k_{-1}[\mathrm{ES}] + k_{cat}[\mathrm{ES}] = k_1[\mathrm{E}][\mathrm{S}] \tag{3-7}$$

$$(k_{-1} + k_{cat})[ES] = k_1[E][S] \tag{3-8}$$

and, the Michaelis constant, K_m is defined as

$$K_m = \frac{(k_{-1} + k_{cat})}{k_1} = \frac{[E][S]}{[ES]} \tag{3-9}$$

$$[\mathrm{E}] = [\mathrm{E}]_{\mathrm{total}} - [\mathrm{ES}] \tag{3-10}$$

Substituting these into the Equation (3-6) gives

$$V_0 = \frac{k_{cat}[E]_{total}[S]}{K_m + [S]} \tag{3-11}$$

The maximum velocity, V_{max}, occurs when the enzyme is saturated, that is, when all enzyme molecules are tied up with S, or $[\mathrm{ES}] = [\mathrm{E}]_{\mathrm{total}}$, thus,

$$V_{max} = k_{cat}\,[\mathrm{E}]_{\mathrm{total}} \tag{3-12}$$

Substituting V_{max} into Equation (3-11) gives

$$V_0 = \frac{V_{\max}[S]}{K_m + [S]} \tag{3-13}$$

This is called the Michaelis-Menten equation. The Michaelis-Menten equation has the form of rectangular hyperbola (Figure 3-21).

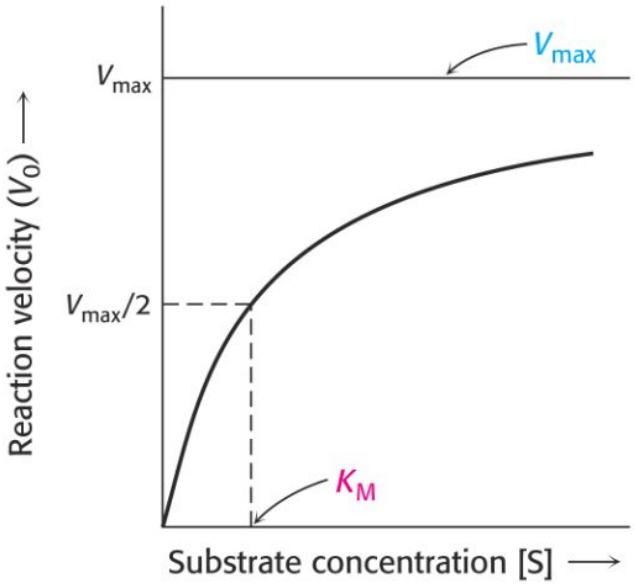

Figure 3-21 . Michaelis-Menten curve.

3.5.2.2 Measurement

Heat of reaction measurement has been demonstrated with enzyme activity of urease. Urease catalyzes the hydrolysis of urea and liberates heat:

$$(NH_2)_2CO + 3H_2O \xrightarrow{Urease} 2NH_4^+ + HCO_3^- + OH^-, \Delta H = -61 \text{kJ/mol}$$

The vacuum chamber was evacuated before the measurement. The microfluidic chamber was flushed with buffer solution to prevent any heat from wetting or nonspecific

binding on Parylene surface. Urease solution (0.5 mg/ml, type C-3, purchased from Sigma Aldrich, St. Louis) was filled in the chamber first. Urea (50 mM , purchased from USB corp., Cleveland) was injected into the chamber using PDMS pumps. Both urease and urea were prepared in the same buffer, 0.2 M sodium phosphate buffer with pH 7.0, to minimize the heat of mixing.

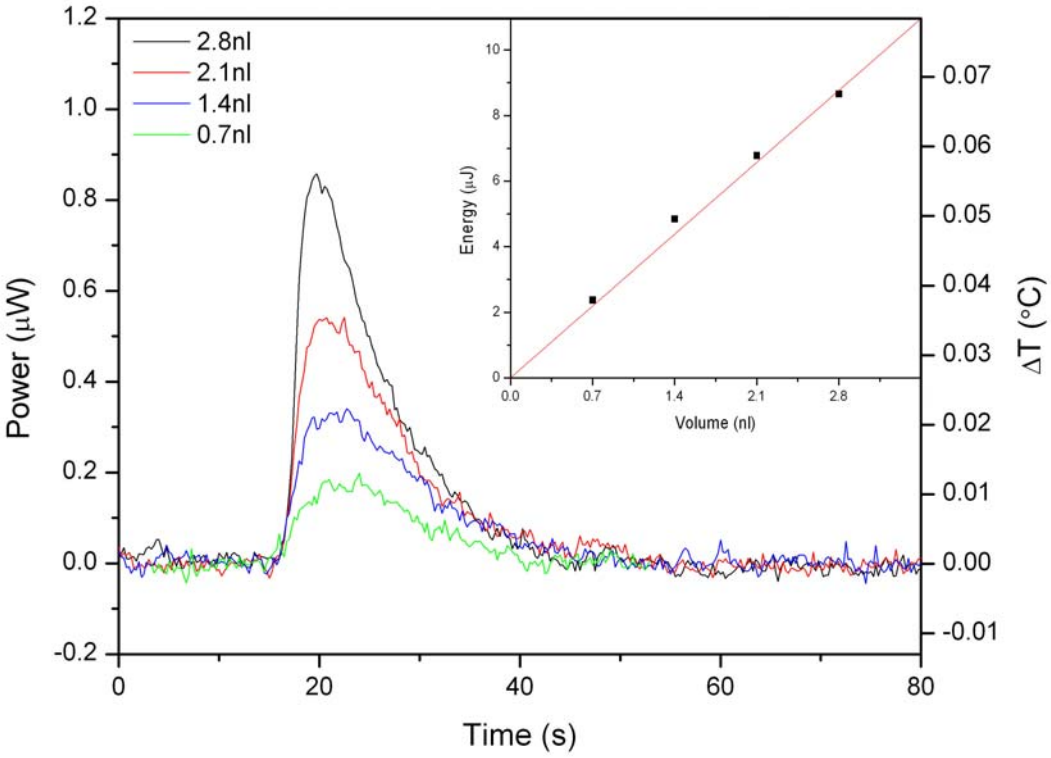

Figure 3-22. Urea hydrolysis by urease. Energy integration is shown in the inset.

Measurement results from 700 pL to 2.8 nL injections, which correspond to 35 pmol to 140 pmol of urea, are plotted in Figure 3-22. Existing chip calorimeters can scale the sample volume up to ~500 nL [25, 26] because evaporation prevents further scaling.

Thought the demonstrated concentration is rather high, this demonstration is the first heat of reaction measurement with nanoliter sample volume. Another chip calorimeter work has claimed the attainment of sensitivity as small as 1.5 nW [27]. However, these devices lack reliable sample handling and could only be used for demonstration measurements of the heat of evaporation. As shown in Figure 3-20 and 3-22, the signals obtained in our work are free of transients from artifacts such as sample injection or drift from evaporation. This is among the benefits of our chip calorimeter implementation using closed chambers and PDMS microfluidic control.

To compare the results we have obtained with those possible from a commercial calorimeter, separate measurements were carried out with a MicroCal VP-ITC calorimeter. Figure 3-23 shows the measurement of the heat of reaction from 2μl of 50mM urea with urease. The negative peak represents the exothermic reaction (the instrument uses the "heat compensation mode"). The enthalpy change (ΔH) of the urea hydrolysis was found to be 14.5 ± 0.6 kcal/mol. The straight line in the inset of Figure 3-22 represents the expected energy with ΔH=14.5 kcal/mol. We can see that the measurements with the chip calorimeter agree very well with those from the commercial colorimeter. Measurement errors of order a few hundred nJ are mainly from the deviation of the injection volume with the PDMS pneumatic pump (about ±30 pL). The error from the electrical measurements is much smaller (a few nJ), and those arising from thermal fluctuations of the system are even smaller (a few pJ).

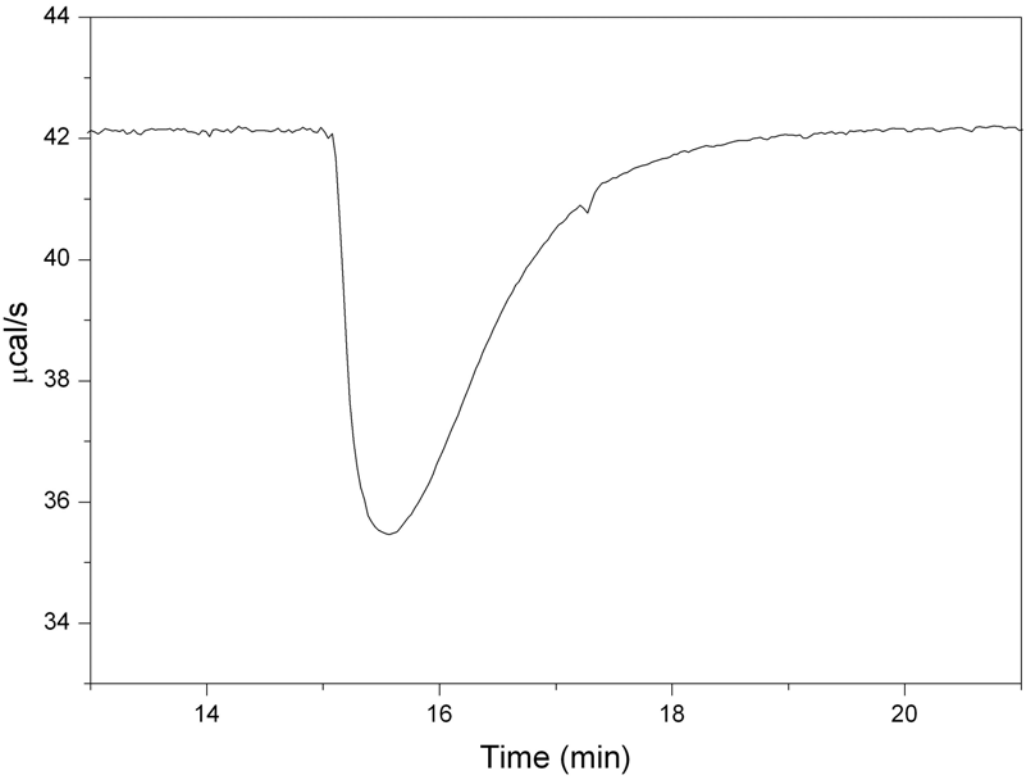

Figure 3-23. Measurement of urea hydrolysis with VP-ITC.

References

1. Cooper, M.A., *Label-free screening of bio-molecular interactions.* Analytical and Bioanalytical Chemistry, 2003. **377**(5): p. 834-842.
2. Blandamer, M.J., P.M. Cullis, and P.T. Gleeson, *Three important calorimetric applications of a classic thermodynamic equation.* Chemical Society Reviews, 2003. **32**(5): p. 264-267.
3. Bundle, D.R. and B.W. Sigurskjold, *Determination of accurate thermodynamics of binding by titration microcalorimetry*, in *neoglycoconjugates, Pt B*. 1994. p. 288-305.
4. Ababou, A. and J.E. Ladbury, *Survey of the year 2005: Literature on applications of isothermal titration calorimetry.* Journal of Molecular Recognition, 2007. **20**(1): p. 4-14.
5. Cooper, A., et al., *Heat does not come in different colours: entropy-enthalpy compensation, free energy windows, quantum confinement, pressure perturbation calorimetry, solvation and the multiple causes of heat capacity effects in biomolecular interactions.* Biophysical Chemistry, 2001. **93**(2-3): p. 215-230.
6. Doyle, M.L., *Characterization of binding interactions by isothermal titration calorimetry.* Current Opinion in Biotechnology, 1997. **8**(1): p. 31-35.
7. Freire, E., O.L. Mayorga, and M. Straume, *Isothermal Titration Calorimetry.* Analytical Chemistry, 1990. **62**(18): p. A950-A959.
8. Holdgate, G.A., *Making cool drugs hot: Isothermal titration calorimetry as a tool to study binding energetics.* Biotechniques, 2001. **31**(1): p. 164-184.

9. Ladbury, J.E., *Application of isothermal titration calorirnetry in the biological sciences: Things are heating up!* Biotechniques, 2004. **37**(6): p. 885-887.

10. Ladbury, J.E. and B.Z. Chowdhry, *Sensing the heat: The application of isothermal titration calorimetry to thermodynamic studies of biomolecular interactions.* Chemistry & Biology, 1996. **3**(10): p. 791-801.

11. Beezer, A.E., et al., *Pharmaceutical microcalorimetry: applications to long-term stability studies.* International Journal of Pharmaceutics, 1999. **179**(2): p. 159-165.

12. Bruylants, G., J. Wouters, and C. Michaux, *Differential scanning calorimetry in life science: Thermodynamics, stability, molecular recognition and application in drug design.* Current Medicinal Chemistry, 2005. **12**(17): p. 2011-2020.

13. Freire, E., *Differential scanning calorimetry.* Methods Molecular Biology, 1995. **40**: p. 191-218.

14. Johnson, C.M., A. Cooper, and P.G. Stockley, *Differential Scanning Calorimetry of Thermal Unfolding of the Methionine Repressor Protein (Metj) from Escherichia-Coli.* Biochemistry, 1992. **31**(40): p. 9717-9724.

15. Ladbury, J.E., *Counting the Calories to Stay in the Groove.* Structure, 1995. **3**(7): p. 635-639.

16. Feng, G.H. and E.S. Kim, *Micropump based on PZT unimorph and one-way Parylene valves.* Journal of Micromechanics and Microengineering, 2004. **14**(4): p. 429-435.

17. Xie, J., et al., *Surface micromachined electrostatically actuated micro peristaltic pump.* Lab on a Chip, 2004. **4**(5): p. 495-501.

18. Shih, C.Y., T.A. Harder, and Y.C. Tai, *Yield strength of thin-film Parylene C.* Microsystem Technologies-Micro-and Nanosystems-Information Storage and Processing Systems, 2004. **10**(5): p. 407-411.

19. Dabral, S., et al., *Stress in thermally annealed Parylene films.* Journal of Electronic Materials, 1992. **21**(10): p. 989-994.

20. *Seebeck coefficient*, efunda.com, http://www.efunda.com/DesignStandards/sensors/thermocouples/thmcple_theory.cfm.

21. Ladbury, J.E. and B.Z. Chowdhry, *Biocalorimetry- Applications of Calorimetry in the Biological Sciences*. 1998, Chichester: John Wiley & Sons.

22. Benjamin, L. and G.C. Benson, *A Deuterium Isotope Effect on Excess Enthalpy of Methanol-Water Solutions.* Journal of Physical Chemistry, 1963. **67**(4): p. 858-861.

23. Lama, R.F. and B.C.Y. Lu, *Excess thermodynamic properties of aqueous alcohol Solutions.* Journal of Chemical and Engineering Data, 1965. **10**(3): p. 216-219.

24. Wensink, E.J.W., et al., *Dynamic properties of water/alcohol mixtures studied by computer simulation.* Journal of Chemical Physics, 2003. **119**(14): p. 7308-7317.

25. Lerchner, J., A. Wolf, and G. Wolf, *Recent developments in integrated circuit calorimetry.* Journal of Thermal Analysis and Calorimetry, 1999. **57**(1): p. 241-251.

26. Torres, F.E., et al., *Enthalpy arrays.* Proceedings of the National Academy of Sciences of the United States of America, 2004. **101**(26): p. 9517-9522.

27. Chancellor, E.B., et al., *Heat conduction calorimeter for massively parallel high throughput measurements with picoliter sample volumes.* Applied Physics Letters, 2004. **85**(12): p. 2408-2410.

Chapter 4

Chip Calorimeters for Cellular metabolism

4.1 Introduction

4.1.1 Chip Calorimeters for Cellular Metabolism

Cells are the functional unit of living organisms and can be considered as self-sustaining, miniature chemical reactors. Cells grow continuously, reproduce, build structures and respond to the environment through a set of chemical reactions called metabolism. Metabolism is usually divided into catabolism and anabolism. Catabolism is breaking down large molecules to produce energy, while anabolism uses energy to construct components of cells. Through these processes cells maintain their complexity and increase the entropy of their surroundings. The metabolism of the cell is also accompanied by enthalpy change. Because heat generation is a reflection of the cellular metabolism, calorimetric measurements allows one to monitor the cellular metabolic rate and to study the associated kinetics [1-8].

There are several indicators of cellular metabolism other than heat generation. The most common indicators are substrate (e.g., glucose and O_2) consumption and the production of extracellular products (e.g., lactate and CO_2). However, the metabolic rate is not fully accounted for with these indicators and some prior knowledge of metabolism is required to quantify its rate. For example, high oxygen consumption may represent a fast metabolic rate, but it does not give information about anaerobic metabolism. Hence, the true metabolic rate remains unknown unless all other substrate consumptions are monitored. Only measurement of cellular heat flux provides direct quantitative measurement of metabolic rate in real-time. By the first law of thermodynamics, the total heat generation is equal to the sum of the enthalpy change of all metabolic reactions and chemical side reactions. It is possible to calculate the energy and material budget of metabolism with information on the substrate consumption, product formation and heat generation in hand. Therefore, metabolic energy balance measurement can reveal "hidden" metabolic pathways and the stoichiometry of the substrates.

Beyond their fundamental scientific purposes, calorimeters are increasingly being used by the pharmaceutical industry as a probe for cellular metabolic rate. Because the drugs (e.g., therapeutic proteins) produced by genetically engineered cells require precise control of cellular physiological conditions, real-time monitoring of metabolism with calorimeters can greatly help optimizing the cell culture growth conditions and predicting the changes to various stimuli [2, 3, 9]. Calorimeters can also be applied to perform cytological tests to screen new drugs [10]. Because cell-based assays require high-throughput parallel processing, the application of chip calorimeters is especially

promising; this approach should prove useful for testing the effect of libraries of synthetic drugs.

Scaling down of device size results in the simultaneous scaling of the physical and biological parameters. At cellular dimensions, some biological phenomena have very fast time scale, therefore ideal measurement tools also need to conform to a similar time scale [11]. In particular, the thermal relaxation time constant for chip calorimeters becomes small and enables fast response time. Other benefits of chip calorimeter include less consumption of precious analyte and low cost for the device.

We have developed chip-based flow calorimeters that can directly measure the heat evolved from cellular metabolism. The calorimetric chamber can accommodate the cell culture to measure the metabolic rate directly. The devices can also be used as chemical sensing if enzyme-coated beads are loaded inside its chamber.

4.1.2 Theory of Flow Calorimeters

Flow calorimetry has a unique property because its sample volume is not fixed. The differential equation governing a calorimeter with a time-varying heat capacity can be represented by

$$\frac{d(C(t)\cdot T(t))}{dt} + G\cdot T(t) = P(t) \tag{4.1}$$

where *C(t)* is heat capacity of sample, *G* is thermal conductance of calorimeter and *P(t)* is power generated from sample.

For most calorimeters, the heat capacity of the system is constant. Therefore, if the system is at steady state,

$$\frac{d(C(t)\cdot T(t))}{dt} = C\frac{dT(t)}{dt} = 0 \tag{4.2}$$

However, in case of flow calorimetry, the heat capacity of the system is a function of time because the sample is continuously refreshed.

We will consider a typical flow calorimeter geometry, namely, a pipe with liquid flowing inside (Figure 4-1). First, let us assume thermal resistance of the pipe is infinite so there is no heat flow across the wall. The liquid flowing inside generates heat, Q per unit volume. The area of cross-section of the pipe is A, the heat capacity of liquid is c and the density of liquid is ρ. The flow speed of the liquid is v.

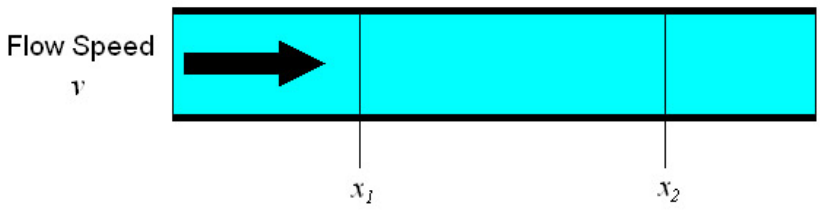

Figure 4-1. Flow calorimeter schematic.

The temperature difference at x_1 and x_2 is

$$\Delta T(x_1, x_2) = T(x_1) - T(x_2) \tag{4.3}$$

The volume element dV flowing past a given point per unit time is

$$dV = A \cdot v \cdot dt \tag{4.4}$$

This volume transports heat,

$$dQ = dV \cdot \rho \cdot c \cdot T \tag{4.5}$$

Therefore,

$$\dot{Q} = A \cdot v \cdot c \cdot T \tag{4.6}$$

Let $T(x_1)$ be the temperature at substrate, $T(x_2)$ the temperature at calorimetric cell. Then,

$$\dot{Q}(x_1) = A \cdot v \cdot c \cdot T(x_1) = 0 \tag{4.7}$$

$$\dot{Q}(x_2) = A \cdot v \cdot c \cdot T(x_2) \tag{4.8}$$

$$\begin{aligned} \dot{Q}(x_2) &= A \cdot v \cdot \rho \cdot c \cdot T(x_2) \\ &= A \cdot v \cdot \rho \cdot c \cdot \left(T(x_2) - T(x_1)\right) \\ &= K(v) \cdot \Delta T(x_2, x_1) \end{aligned} \tag{4.9}$$

where,

$$K(v) = A \cdot v \cdot \rho \cdot c \tag{4.10}$$

$K(v)$ can be considered as an equivalent thermal conductance, representing the cooling effect from flow. In other words, even under perfectly adiabatic conditions, the system would work as a conduction calorimeter with this equivalent thermal conduction.

In reality, we cannot assume that perfectly adiabatic condition ever holds. Therefore, we write $K(v) > A \cdot v \cdot \rho \cdot c$.

$$K(v) = A \cdot v \cdot \rho \cdot c + \frac{1}{R_{th}} \tag{4.11}$$

$$R_{th} = \frac{1}{G} \tag{4.12}$$

It is not easy to calculate exact value of R_{th} for most calorimeters, thus $K(v)$ is usually measured by means of electric heating:

$$K(v) = Q_{elec} / \Delta T_{meas} \tag{4.13}$$

where Q_{elec} is the applied electric heating and ΔT_{meas} is the measured temperature difference.

4.2 Device Design

The structure of the chip-based flow calorimeter is very similar to the chip based conduction calorimeter described in Chapter 3. The main structure is built in the same way as the conduction calorimeter; the Parylene microfluidic system is surrounded by the vacuum chamber and the thermometer is buried in the Parylene layers. The major change is that made in the design of the microfluidic structure and the shape of the Parylene membrane (Figure 4-2).

Cutting down the unnecessary material helps reduce the total thermal conductance and the device heat capacity, and these results in better sensitivity. The Parylene membrane is etched on the side to make a 3 mm long bridge structure. The reaction chamber is located at the center of the suspended bridge structure. Because the heat generated inside the chamber is conducted away mainly by the bridge, the device thermal conductance can be reduced compared to the membrane structure. The number of thermocouple junctions is also reduced. By doing so, we get less thermal conduction through the electrical leads. However, this also results in the development of smaller

thermoelectric voltages for a given heat gradient. The geometry of thermopile and the number of junctions are related to the thermal conductance, the total Seebeck coefficient and the electrical noise. Therefore, they have to be optimized for each specific system. This will be discussed at the end of this chapter.

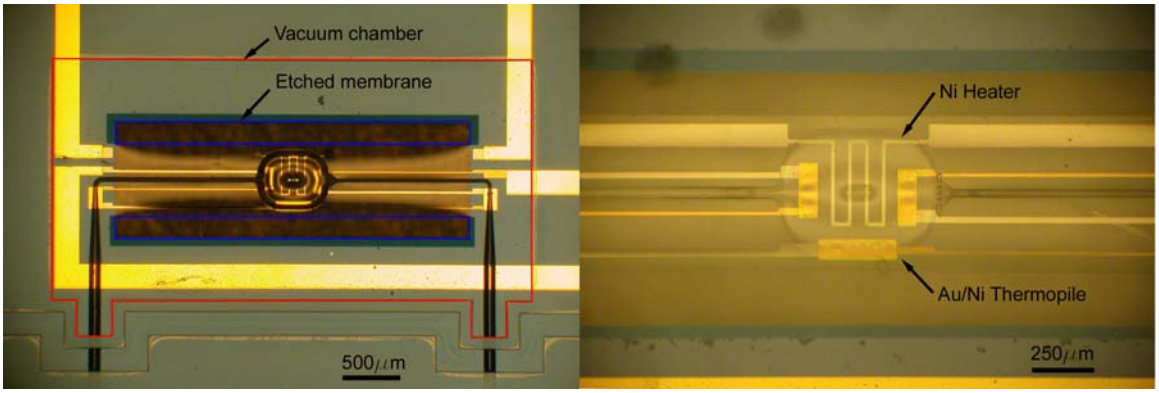

Figure 4-2. Suspended Parylene bridge structure (left) and the reaction chamber (right).

Two microfluidic channels are connected to the reaction chamber, which is built to accommodate biological samples (e.g., cells) or enzyme-coated beads. Growth media for cell culture or analyte can be flowed through the chamber. A post was fabricated at the center of the reaction chamber to minimize chamber expansion under vacuum, and to divert the flow within the chamber. This particular device is designed to accommodate a large number of cells or beads, each with diameter 4–8μm. The chamber is 500 μm wide and 600 μm long. All the Parylene fluidic structures have about the same 10 μm height. The chamber and channel size can be adjusted according to the sample size and the purpose of measurement.

The device can be utilized as a chemical sensor by embedding enzyme-coated beads within the reaction chamber. For this purpose, the beads must be kept from flowing out of

the chamber. For this an obstruction was incorporated in the outlet channel. Beads or cells bigger than ~4 μm in diameter can be collected in the chamber with the structure (Figure 4-3).

Because the Parylene channel geometry is defined by photolithography with thick resist, making narrow channels require high aspect ratio lithography. The obstruction was made by reducing the channel height rather than narrowing the channel width. The reduction of the channel height at the outlet was achieved by building a SU-8 "weir" structure, which is shown in Figure 4-3 and 4-4. The SU-8 weir structure bocks the parylene channel partially trapping the particles at the weir.

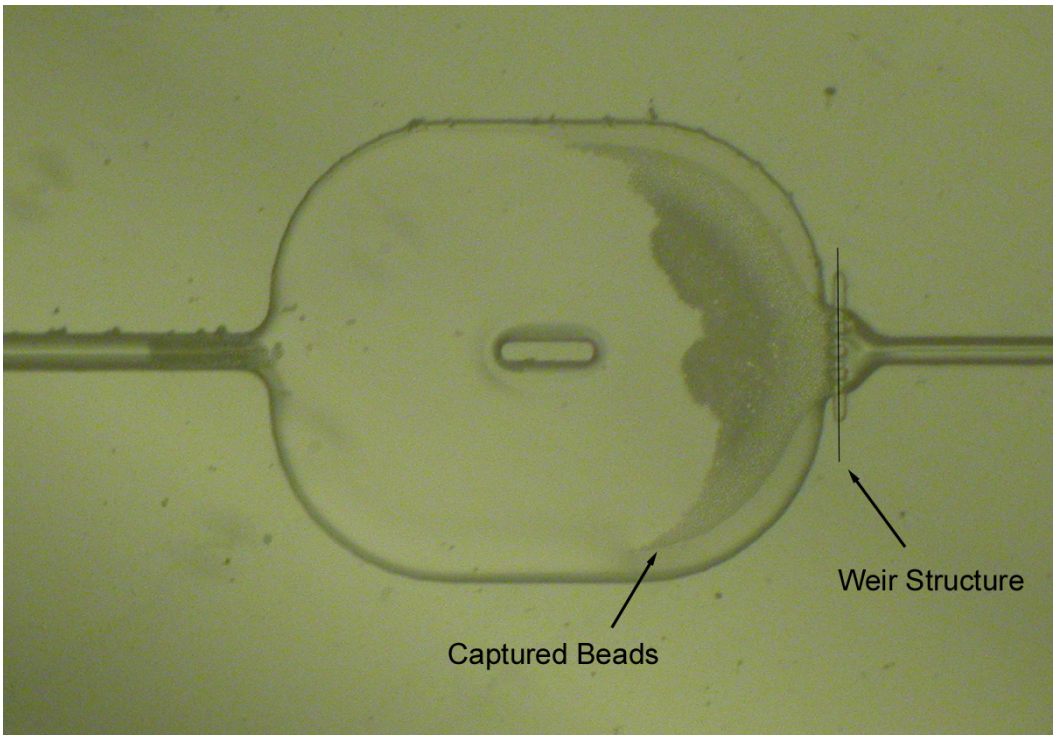

Figure 4-3. Bead capture test.

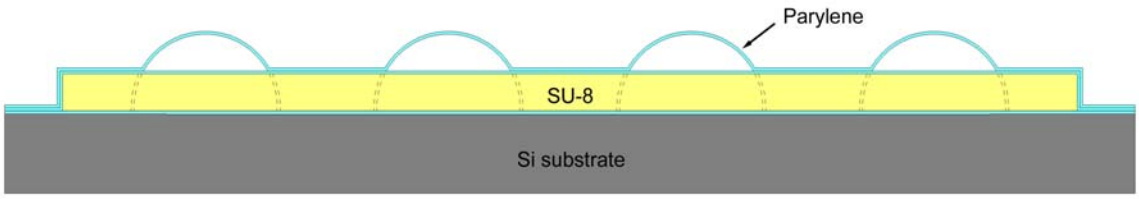

Figure 4-4. SU-8 weir structure. Cross-sectional view.

To reduce measurement noise, a differential measurement scheme is adopted. As shown in Figure 4-5, the device has two identical reaction chambers: one for measurement of the metabolism (or reaction) and one for reference. A buffer solution with analyte, whose heat evolution is of interest, is fed thorough the measurement chamber, while only buffer solution is fed thorough the reference chamber. This way all other effects will be subtracted, improving the signal-to-noise ratio for measurements.

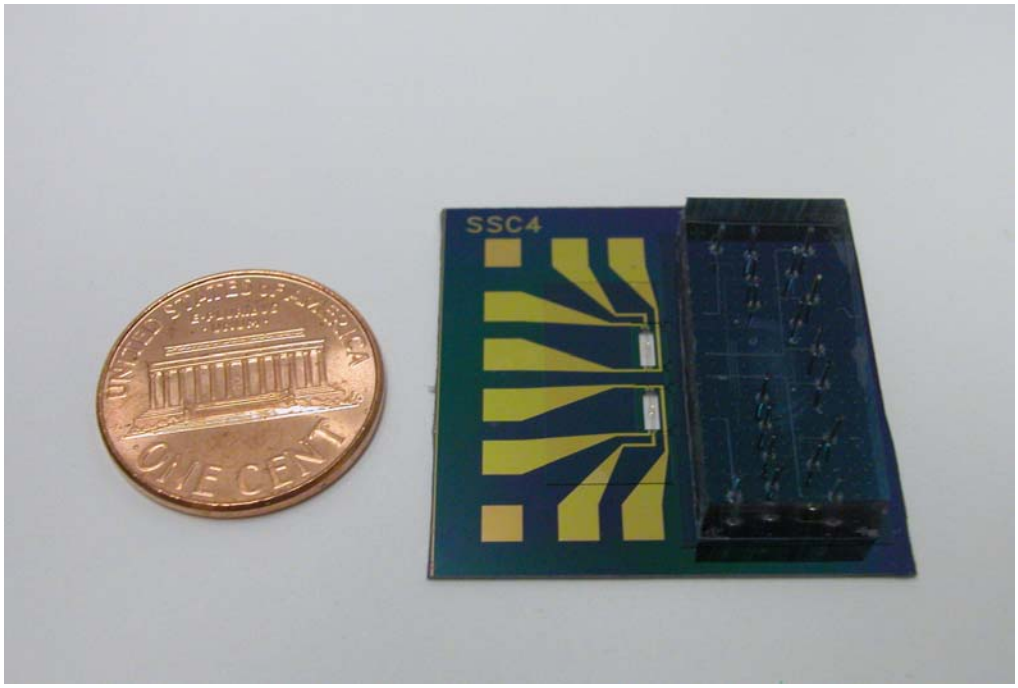

Figure 4-5. Flow calorimeter with twin calorimetric chamber.

PDMS microfluidic control is also designed to support this differential measurement. In Figure 4-6, the flow channel is shown in blue and the control channel is shown in red. Two identical sets of flow channels are connected to the Parylene microfluidic channels. They provide 3 inlets (1–3 in Figure 4-6) and 1 outlet (4 in Figure 4-6) for each calorimeter. The inlets can be used for different analytes and growth media. The PDMS peristaltic pump in the middle allows the same amount of flow into the chambers. A syringe pump can be used as an alternative way of making same rate of flow into the chambers. A syringe pump can make injection rates as small as ~2 pL/min.

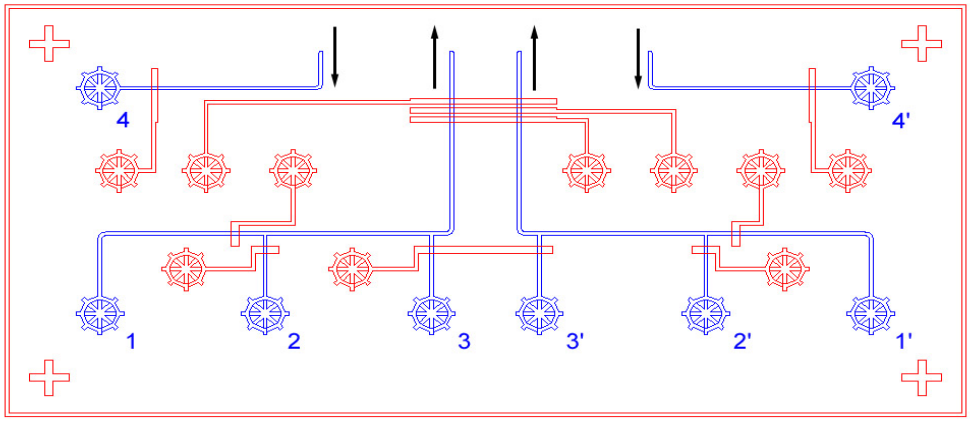

Figure 4-6. PDMS microfluidic flow channels (blue) and control channels (red).

4.3 Device Fabrication

Fabrication steps are similar to the steps described in Chapter 3. More fabrication steps are added for the weir structure and the membrane etching. The first Parylene layer

(1 μm thick) is deposited on the SiN membrane and the thermocouple and heater are built on the Parylene layer. The thickness of gold is 40 nm and nickel is 60 nm. The heater is built with nickel to reduce the thermal conductance.

The SU-8 weir structure is built with SU-8 5 negative resist. SU-8 weir structure has 6 μm height. The second Parylene layer (1 μm thick) is deposited to cover the electrical components and weir structure. 10 μm thick sacrificial layer is spin-coated with AZ 9260 photoresist. Because thick resists have high viscosity, the thickness of the resist on top of the weir structure is still close to ~10 μm after coating. It is required to rest the resist before baking. The wafer is placed in a sealed container to prevent the solvent evaporation, and left for 30 minutes so that the resist flows to flatten the surface. Then the resist is baked and patterned to shape the microfluidic structure. The third Parylene layer (2μm thick) is deposited on the sacrificial photoresist for the microfluidic channel wall.

The Parylene membrane is etched to a bridge structure for better sensitivity. 100 nm thick gold layer is used as an etching mask. A 4 nm thick titanium adhesion underlayer is used to ensure good adhesion of the etching mask. The etching mask is patterned by photolithography and chemical wet etching. Then the Parylene layers are etched through with RIE (O_2 150 mTorr, 140 W). The SiN membrane is intact during this step because oxygen RIE has great selectivity between polymers and inorganic substrates. The gold mask is removed by chemical wet etching after the Parylene etching. The rest of the steps are the same as described in Chapter 3.

4.4 Device Calibration

We estimated the device thermal conductance using finite element simulation. The model geometry for the simulation is shown in Figure 4-7. It has 4μm thick Parylene membrane, 40 nm thick gold and 60 nm thick nickel layers. The chamber has 500 μm width, 600 μm length and 15 μm height. The channel is 30 μm wide and 15 μm high, connecting the chamber and substrate. The substrate is not included in the model; instead, the ends of the Parylene bridge are set to be at constant temperature. The vacuum condition is assumed to be good enough for the top and bottom surface to be treated as adiabatic.

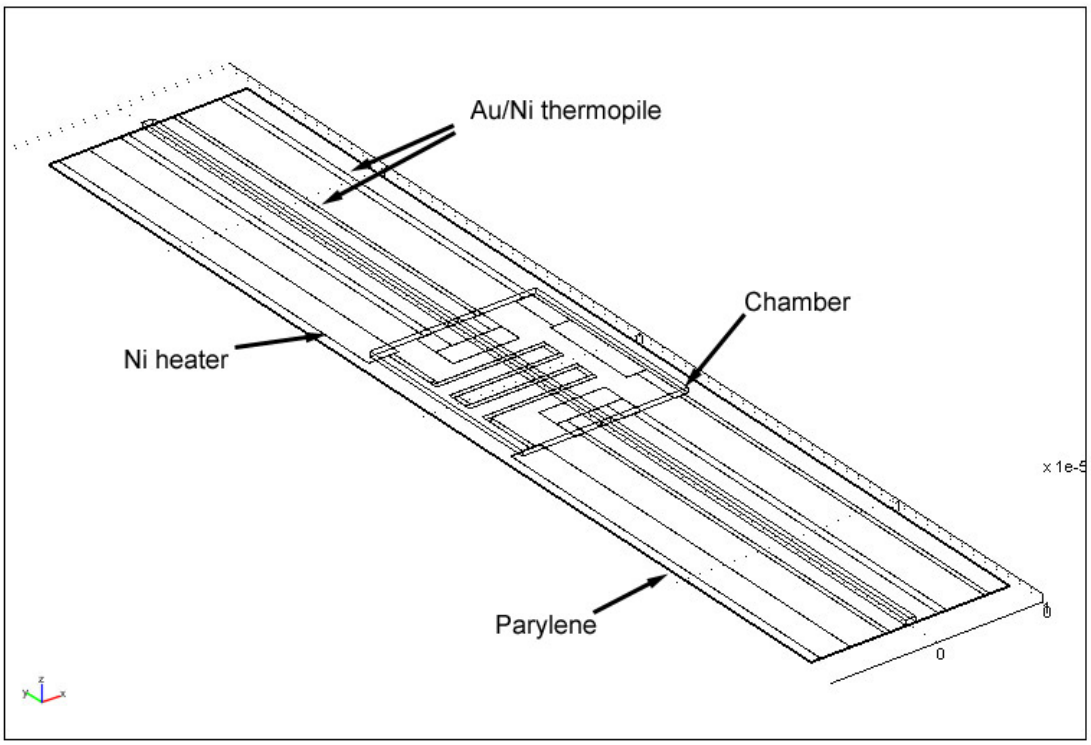

Figure 4-7. The model geometry for thermal conductance simulation.

Thermal conductance was calculated by applying 1 μW of power at the chamber. The temperature rise in the chamber was 0.44 K and the thermal conductance was 2.3 μW/K (Figure 4-8). To calibrate the heater efficiency, uniform heating was applied to the heater. With 1 μW power applied, the temperature in the chamber increased by 0.35 K (Figure 4-9). This factor needs to be considered when the thermal conductance of the device is calibrated by heating with the electric heater. In other words, 80% of the total power applied to the heater is considered as being used to heating the chamber.

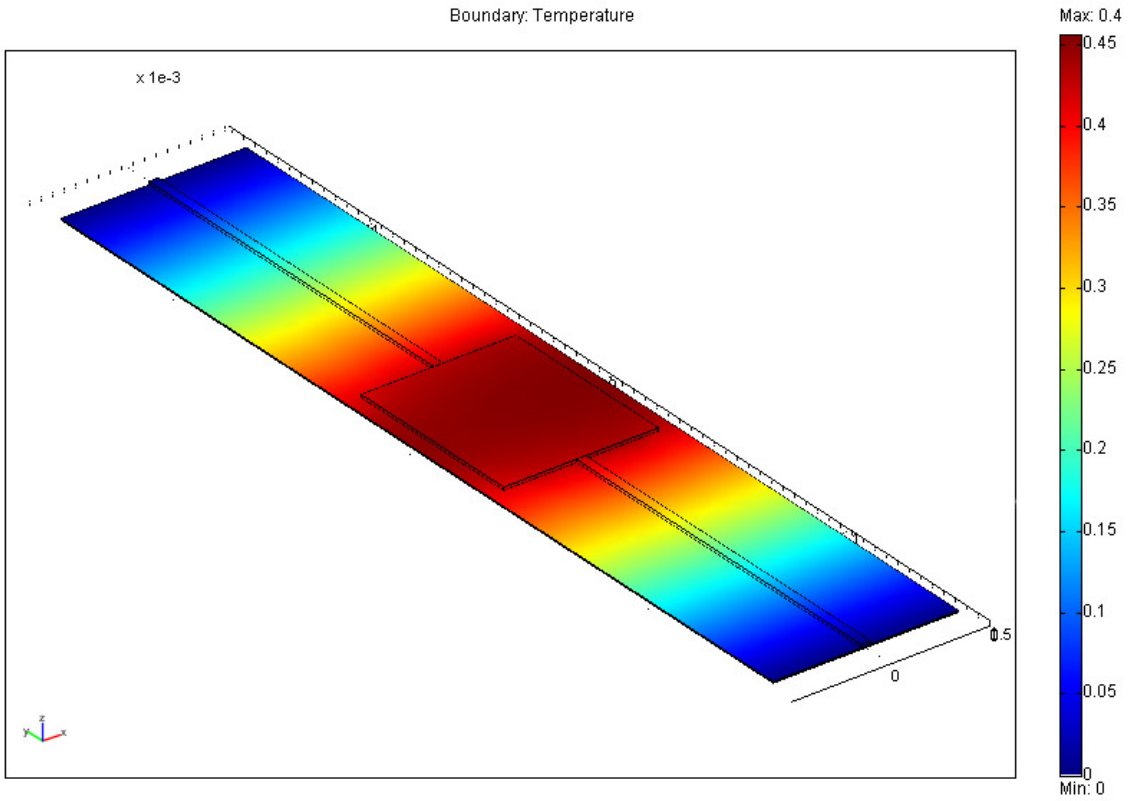

Figure 4-8. Temperature profile with heating at the chamber.

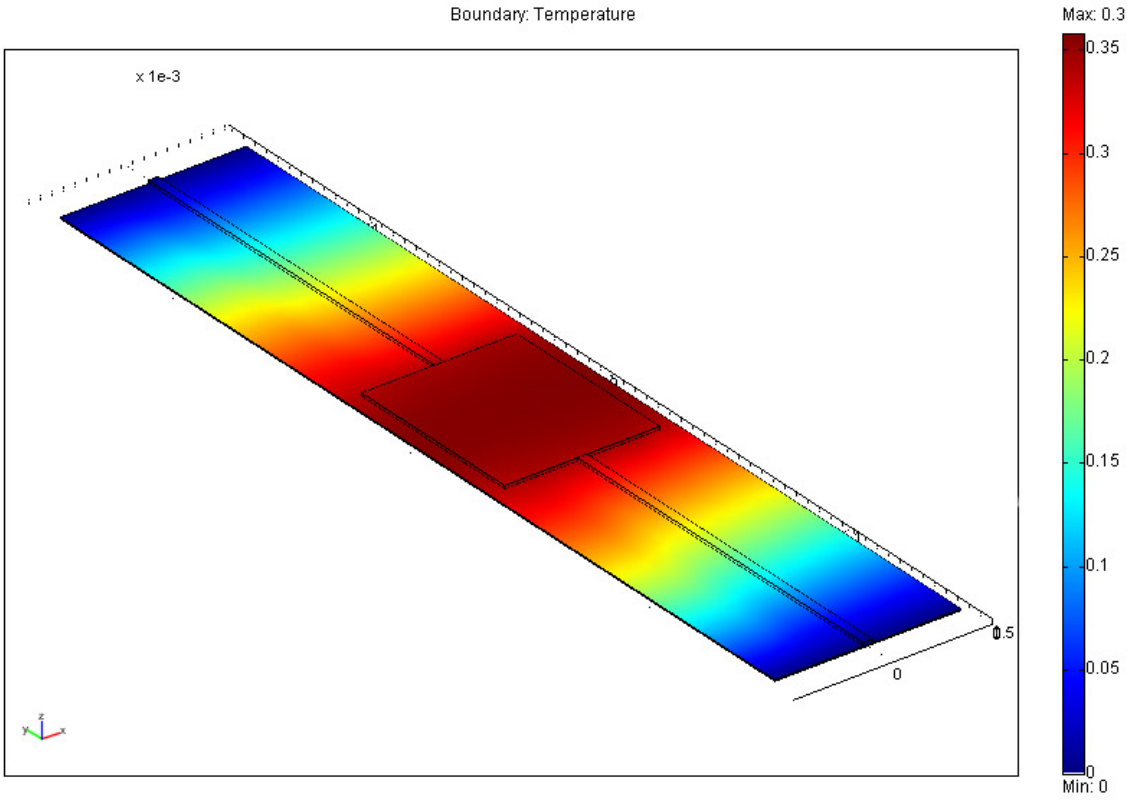

Figure 4-9. Temperature profile with heating at the heater.

We have measured the thermal response of the device by applying electric heating. (Figure 4-10). The measurement was done without sample in the chamber and the vacuum chamber was evacuated before the measurement. We applied 46mV pulse on the heater with 826 Ω resistance, which makes pulse of 2.56 μW power. Considering the efficiency of the heater (80%), the actual power that is heating the chamber is 2.05 μW. With the power and the voltage response (29 μV), we get the heat power sensitivity of the device, which is 14 V/W. This is about twice larger value, compared to that of the chip-based conduction calorimeters described in Chapter 3.

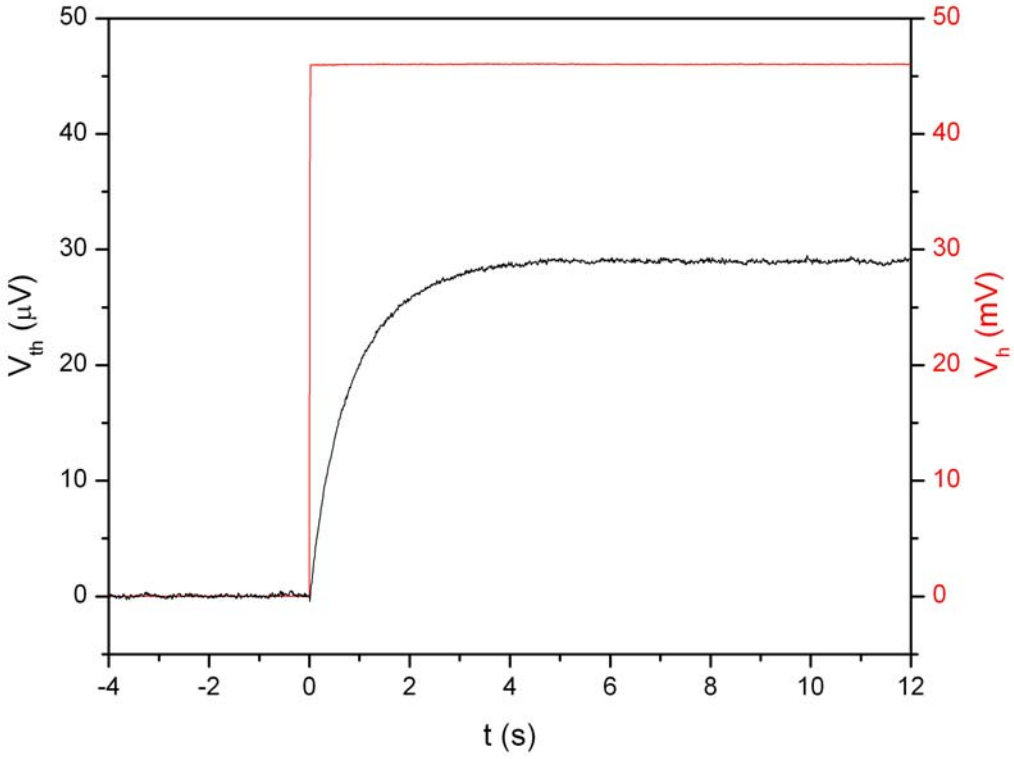

Figure 4-10. Thermometer response to a heating pulse.

The thermopile has 66 μV/K total Seebeck coefficient and the corresponding temperature change to 29 μV is 0.44 K. Together with applied power we get the device thermal conductance: 4.7 μW/K. This is about 3 times smaller than that of the chip-based conduction calorimeters, which is the result of the design changes.

The measured thermal conductance did not agree with the simulation result; the measured thermal conductance was about twice the value expected from simulations. We have fairly simple geometry and expected the simulation results to give a precise estimation. As we discussed earlier in Chapter 3, it is believed that the disagreement is

originated from the Parylene thermal conductivity increase due to thermal cycling in the fabrication steps.

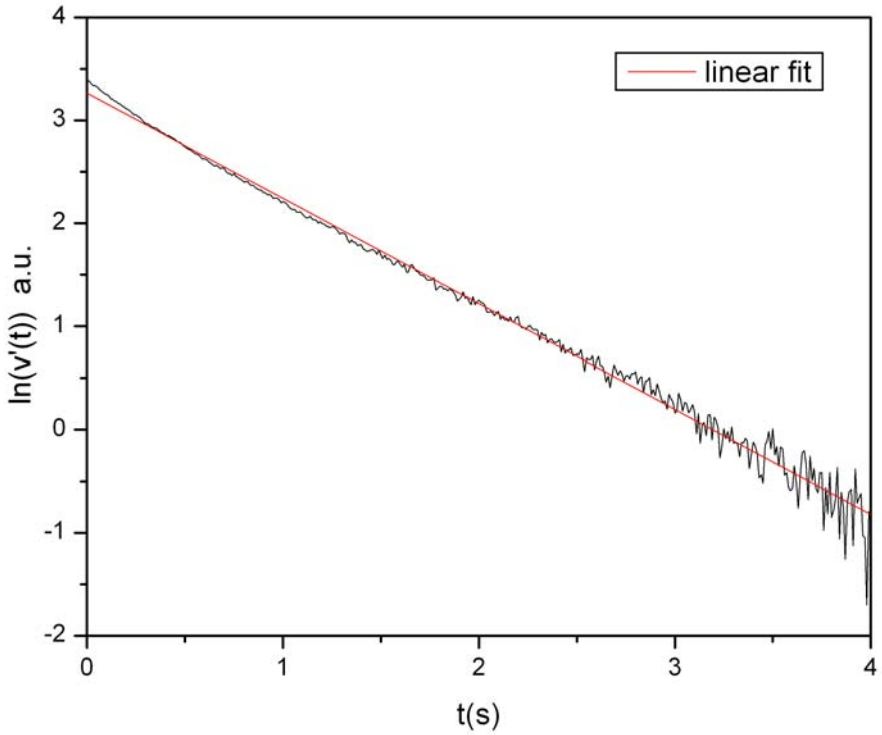

Figure 4-11. Thermal relaxation time constant.

The thermal relaxation time constant was determined by fitting to the exponential increase (Figure 4-11). The time constant was 0.98 s. The device heat capacity is calculated from the conductance and the time constant. 4.56 μJ/K was the device heat capacity. If we assume the linear temperature change along the Parylene bridge, the effective heat capacity of the Parylene bridge is approximately 3.3 μJ/K, which is close to the measurement. The heat capacity of the metal electrodes is negligible.

The electrical noise of the measurement comes from the Johnson noise of the thermopile and amplifier. The voltage noise referred-to-input is ~7 nV with 1Hz bandwidth. The temperature sensitivity is ~0.33 mK with 3 : 1 signal-to-noise ratio. This corresponds to a power sensitivity of ~1.5 nW.

4.5 Projection to Single Cell Metabolism Measurements

Traditional methods of studying cellular metabolism heavily depend on measuring the average value from many cells or extracts. The resulting averaged value may be misleading because it often does not represent the individual cellular behavior. Moreover, the concentration step results in a delay in measurement. Real-time analysis of biological phenomena at the single cell level can provide new insight into biological systems [12]. However, measurement at the single cell level still has many challenges in sensor technology, cell handling and system integration. For example, calorimetric measurement lacks the sensitivity required for measurement of single cell metabolism, even though it has great potential as a nondestructive, real-time analysis tool.

As shown in Figure 4-12, an average mammalian cell has a metabolic rate of about 30 pW [13]. To study the metabolism of a single cell, 1–10 pW sensitivity will be required, while the most sensitive calorimeters have ~10 nW sensitivity [14]. One of the chip calorimeters has shown proof-of-concept demonstration of measuring a single cell metabolism with very energetic reaction [15]. However, the device sensitivity (~15 nW) was not good enough for general cellular metabolism. Our vacuum insulated microfluidic calorimeters have great potential to achieve the sensitivity for general cellular

metabolism. In this section, we estimates the achievable sensitivity of the microfluidic chip calorimeters.

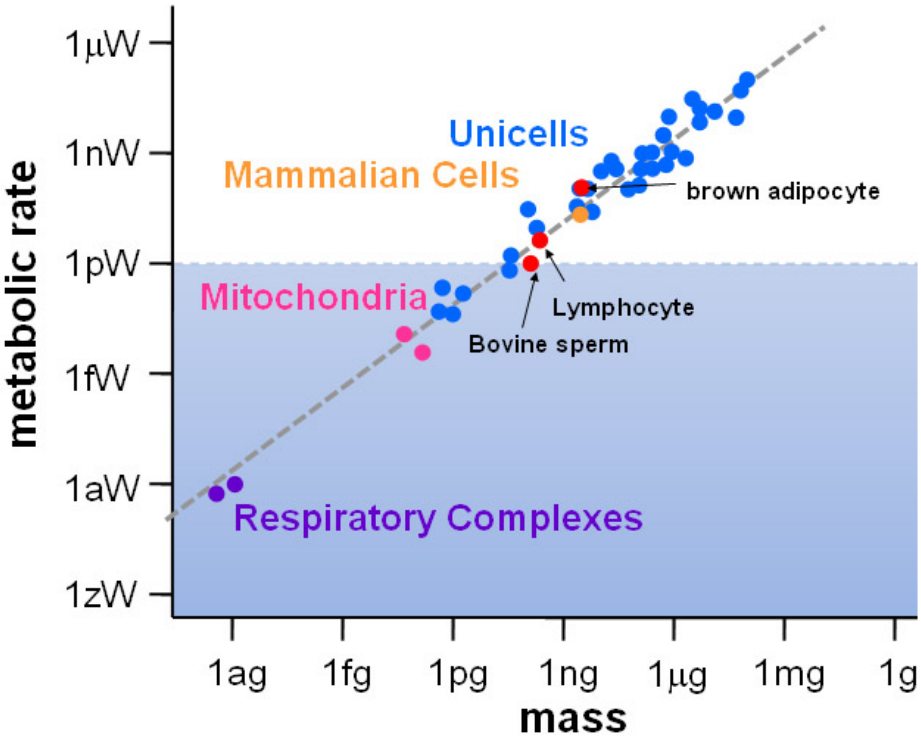

Figure 4-12. Basal metabolic rate as a function of cell mass.

4.5.1 Thermal Conductance Engineering

Device thermal conductance is directly related to the sensitivity of the calorimeter. Reduction of device thermal conductance can be achieved by reducing the heat transfer path. In figure 4-13 the schematic device design is shown. The chamber and channel size are based on the typical mammalian cell size. The Parylene microfluidic structure is built on the 2 mm long Parylene bridge. The cell loading channel has a width of 15 μm and

height of 10 μm. The supply channel is 3 μm wide and 2 μm high. The cell loading channel will be filled with air after loading a cell in the chamber. The Parylene microfluidic channel has 1 μm thick walls.

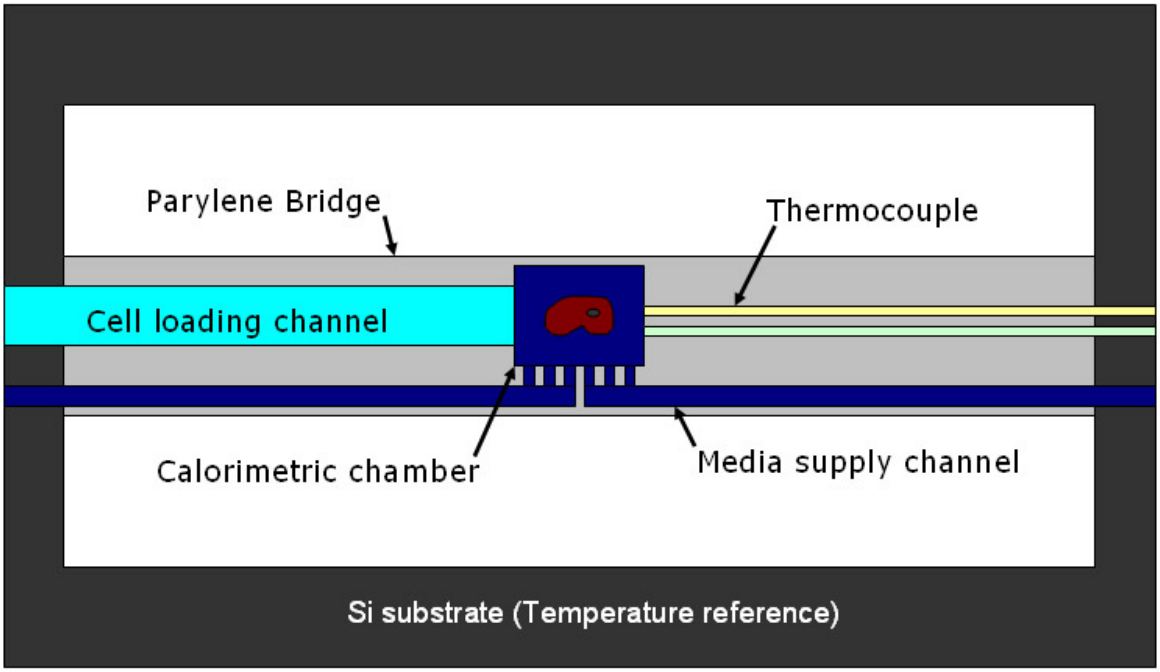

Figure 4-13. Schematic view of a calorimeter for single cell measurement (Top view).

The thermal conductance of the device without the thermometer is calculated as follows. First the Parylene bridge and the channels together are considered as two layers of thin films.

$$G_{pa} = k_{pa}\frac{t \cdot w}{l} \times 2 \times 2 = 0.089\frac{1\times10^{-6} \cdot 20\times10^{-6}}{1\times10^{-3}} \times 2 \times 2\, W/K = 7.12nW/K \qquad (4.14)$$

The thermal conductance of the air in the cell loading channel is

$$G_{Air} = k_{Air}\frac{t \cdot w}{l} = 0.025\frac{10\times10^{-6} \cdot 15\times10^{-6}}{1\times10^{-3}} W/K = 3.75nW/K \qquad (4\text{-}15)$$

The media supply channel is assumed to be filled with water. Then the thermal conductance of the media supply channel is

$$G_{Wa} = k_{Wa}\frac{t \cdot w}{l} \times 2 = 0.606\frac{2\times10^{-6} \cdot 3\times10^{-6}}{1\times10^{-3}} \times 2\,W/K = 7.2nW/K \tag{4.16}$$

The total thermal conductance without the thermocouple (G_{Sum}) can be as small as 18.1 nW/K. The effective heat capacity of the device with this geometry can also be simply calculated. The temperature change in the Parylene bridge and supply channel is approximately linear at steady state, thus they contribute half of their heat capacity to the device heat capacity. Together with water in the chamber and Parylene the effective device heat capacity is ~63.1 nJ/K.

4.5.2 Thermometer

The thermometer can be built in many different ways. For example, infrared imaging can be a convenient way to measure the temperature without contact, but the temperature sensitivity is not very good (~1 mK). Thermocouples are widely used for calorimeters because they are self-referencing and have no heat dissipation for measurement. In this section, we will discuss the sensitivity of calorimeters with thermocouples as the thermometer.

The thermoelectric voltage from a thermopile with *n* thermocouples is

$$V_{Sig} = n\alpha\Delta T \tag{4.17}$$

where, α is the Seebeck coefficient of one thermocouple.

The temperature change (ΔT) is equal to the applied power divided by thermal conductance. Therefore,

$$\Delta T = \frac{P}{G} = \frac{P}{nk\frac{tw}{l} + G_{Sum}} \tag{4.18}$$

where, k is the thermal conductivity of the thermocouple, t is the thickness, w is the width and l is the length of thermocouple.

Assuming the noise of the thermocouple is dominated by Johnson noise, the signal to noise ratio is

$$SNR = \frac{n\alpha\Delta T}{\sqrt{4k_B TR\Delta f}} = \frac{P}{\sqrt{4k_B T\Delta f}} \frac{n\alpha}{\left(nk\frac{tw}{l} + G_{Sum}\right)\sqrt{n\rho\frac{l}{tw}}} \tag{4.19}$$

where, ρ is the electrical resistivity of thermocouple.

If we consider Equation (4.19) as function of purely geometric term, $\frac{ntw}{l} = x$, then

$$\frac{\alpha}{\left(kx + G_{rest}\right)\sqrt{\rho\frac{1}{x}}} = \frac{\alpha}{\sqrt{\rho}\left(k\sqrt{x} + G_{rest}\sqrt{\frac{1}{x}}\right)} \tag{4.20}$$

Equation (4.20) has maximum, when $k\sqrt{x} = G_{Sum}\sqrt{\frac{1}{x}}$, i.e.

$$k\frac{ntw}{l} = G_{rest} \tag{4.21}$$

Putting the into Equation (4.19), we have

$$SNR \le \frac{P}{\sqrt{4k_B T\Delta f}} \frac{1}{2\sqrt{\frac{ntw}{l}}} \frac{\alpha}{k\sqrt{\rho}} \tag{4.22}$$

In the Equation (4.22), the maximum SNR is expressed in terms of material properties (k, ρ and α) and geometry (n, t, t and l) of the thermocouple. When the thermal conductance of the thermopile is a negligible factor in the total thermal conductance, $nk\frac{tw}{l} + G_{Sum} \cong G_{Sum}$, SNR is proportional to $\sqrt{n}$ (Equation 4-6); increase in the number of parallel junction has the same effect as averaging. Therefore, an increase in the number of thermocouples gives better sensitivity, which is true for many chip calorimeters with large thermal conductance. However, when the thermal conductance of the thermocouple is not negligible, it is necessary to optimize the geometry to match the thermal conductance.

The factor $\frac{\alpha}{\kappa\sqrt{\rho}}$ in Equation (4.22) is very similar to the thermoelectric figure of merit, $Z = \frac{\alpha^2}{k\rho}$. Therefore the figure of merit can be a guideline to find a good thermoelectric material to maximize the sensitivity. For example, bismuth telluride compound is well known for its high figure of merit (close to 1) [16, 17].

Table 4-1. Thermoelectric properties of the *p*-type $(Bi_{0.25}Sb_{0.75})_2Te_3$ and *n*-type $Bi_2(Te_{0.94}Se_{0.06})_3$ [17]

		p-type		*n*-type	
		As grown	Annealed	As grown	Annealed
Electrical resistivity	ρ ($\mu\Omega$ m)	8.71	11.7	10.7	8.23
Seebeck coefficient	α (μV/K)	+221	+221	−227	−223
Thermal conductivity	κ (W/mK)	1.48	1.36	1.57	1.65
Figure of merit	ZT	1.13	0.91	0.91	1.09

The room temperature properties of the compound are summarized in Table 4-1. Adjusting the thermal conductance of each thermocouple element to 9 nW/K determines the geometry ratio thus the resistance of them. For p-type compound, the resistance becomes 1.4 kΩ, and for n-type compound, the resistance becomes 1.9 kΩ. Johnson noise from the sum of these two resistances is 7.3 nV/√Hz. Let's assume ~5 nV voltage noise from DC to 0.5 Hz measurement bandwidth. We took the bandwidth of 0.5 Hz because it is the approximately the fastest measurement we can have; the device thermal relaxation time constant is ~2 s. Together with Seebeck coefficient, 450 μV/K, we get ~33 μK temperature sensitivity (3:1 SNR). Finally, combining with the total thermal conductance (36 nW/K), we get ~1.2 pW sensitivity.

This estimation may have some error from noise estimation. Estimation of the low frequency noise (1/f noise) is not a trivial problem and there is also an amplifier issue. The SNR may improve with the smaller bandwidth, but it will degrade temporal resolution of measurement. The bandwidth of the measurement should be chosen properly according to the system under test.

To conclude, the theoretical estimation shows that the microfluidic chip calorimeter with vacuum insulation can achieve sensitivity of order 1 pW. With this level of sensitivity the calorimeter can be used as general analytical tool for most mammalian cells.

References

1. Guan, Y., P.M. Evans, and R.B. Kemp, *Specific heat flow rate: An on-line monitor and potential control variable of specific metabolic rate in animal cell culture that combines microcalorimetry with dielectric spectroscopy.* Biotechnology and Bioengineering, 1998. **58**(5): p. 464-477.
2. Guan, Y.H. and R.B. Kemp, *On-line heat flux measurements improve the culture medium for the growth and productivity of genetically engineered CHO cells.* Cytotechnology, 1999. **30**(1-3): p. 107-120.
3. Kemp, R.B., *The application of heat conduction microcalorimetry to study the metabolism and pharmaceutical modulation of cultured mammalian cells.* Thermochimica Acta, 2001. **380**(2): p. 229-244.
4. Hardewig, I., et al., *Metabolic rates at different oxygen levels determined by direct and indirect calorimetry in the oxyconformer Sipunculus-Nudus.* Journal of Experimental Biology, 1991. **157**: p. 143-160.
5. Kemp, R.B., *Studies of enthalpy balance and adenosine-triphosphate turnover in aultured animal cells.* Pure and Applied Chemistry, 1994. **66**(3): p. 479-484.
6. Liu, J.S., I.W. Marison, and U. von Stockar, *Microbial growth by a net heat up-take: A calorimetric and thermodynamic study on acetotrophic methanogenesis by Methanosarcina barkeri.* Biotechnology and Bioengineering, 2001. **75**(2): p. 170-180.
7. Maskow, T., et al., *Flow calorimetry and dielectric spectroscopy to control the bacterial conversion of toxic substrates into polyhydroxyalcanoates.* Biotechnology and Bioengineering, 2004. **85**(5): p. 547-552.

8. Paulik, M.A., et al., *Development of infrared imaging to measure thermogenesis in cell culture: Thermogenic effects of uncoupling protein-2, troglitazone, and beta-adrenoceptor agonists.* Pharmaceutical Research, 1998. **15**(6): p. 944-949.

9. Voisard, D., et al., *Development of a large-scale biocalorimeter to monitor and control bioprocesses.* Biotechnology and Bioengineering, 2002. **80**(2): p. 125-138.

10. Slater, K., *Cytotoxicity tests for high-throughput drug discovery.* Current Opinion in Biotechnology, 2001. **12**(1): p. 70-74.

11. Prokop, A., et al., *NanoLiterBioReactor: Long-term mammalian cell culture at nanofabricated scale.* Biomedical Microdevices, 2004. **6**(4): p. 325-339.

12. Lidstrom, M.E. and D.R. Meldrum, *Life-on-a-chip.* Nature Reviews Microbiology, 2003. **1**(2): p. 158-164.

13. West, G.B., W.H. Woodruff, and J.H. Brown, *Allometric scaling of metabolic rate from molecules and mitochondria to cells and mammals.* Proceedings of the National Academy of Sciences of the United States of America, 2002. **99**: p. 2473-2478.

14. *ITC specification*, Microcal, http://www.microcal.com/index.php?id=383.

15. Johannessen, E.A., et al., *Heat conduction nanocalorimeter for pl-scale single cell measurements.* Applied Physics Letters, 2002. **80**(11): p. 2029-2031.

16. Yamashita, O., S. Tomiyoshi, and K. Makita, *Bismuth telluride compounds with high thermoelectric figures of merit.* Journal of Applied Physics, 2003. **93**(1): p. 368-374.

17. Yamashita, O. and S. Sugihara, *High-performance bismuth-telluride compounds with highly stable thermoelectric figure of merit.* Journal of Materials Science, 2005. **40**(24): p. 6439-6444.

Chapter 5

Conclusion and Future Work

5.1 Conclusion

Miniaturization is one of the important directions for biosensor research. It conveys many advantages, which include high throughput, better sensitivity, and low cost. Development of chip calorimeters will allow the fast measurements with small sample volume. However, the existing chip calorimeters cannot take full advantage of miniaturization due to their poor sensitivity and sample handling. We have developed microfluidic chip calorimeters with high sensitivity and reliable sample handling. The sensitivity was improved remarkably through reduction of the thermal conductance with optimized geometry, materials, and on-chip vacuum insulation. We have utilized Parylene microfluidic systems to enhance the thermal insulation, physical strength and chemical resistance of the device. PDMS microfluidic control, combined with Parylene microfluidic system, provides precise control of picoliter-scale samples. To achieve

decent device yield and stability, many Parylene microfabrication issues, such as adhesion and etching, were studied.

The chip-based conduction calorimeters for chemical reaction were designed to perform measurement of enthalpy change with 3.5 nL sample volume. The sample was manipulated inside the Parylene microfluidic system with PDMS microfluidic control. Thermal insulation was enhanced with vacuum insulation to give 15.5 μW/K thermal conductance. The calorimeter performance was demonstrated with measurements of the heat of mixing and the enzyme activity. The temperature sensitivity was ~0.27 mK and the power sensitivity was ~4.2nW. This type of device can be built as a calorimetric array to give high-throughput heat of reaction measurement.

The chip-based flow calorimeters were designed for sensor application and cellular metabolism monitoring. The device thermal conductance was 4.7μW/K and the sensitivity was 1.5nW. Further reduction of thermal conductance and the change of thermocouple material can give ~1pW order sensitivity, enabling real-time single cell metabolic rate measurements without the limitations of labeling or knowledge of specific metabolic pathway.

5.2 Recommendations for Future Work

We have shown in Chapter 4, that the device concept has lots of room for further improvement of sensitivity. In addition, there are a couple of very potential research topics to pursue in parallel with sensitivity improvement. These future works are briefly stated in this section.

5.2.1 DSC

Differential scanning calorimetry (DSC) is a tool for investigating protein stability. Combined with other biophysical methods, DSC can provide the linkage between the thermodynamics, structure, and function [1, 2]. There have been a few reports of development of miniaturized DSC [3-5], however, they were not suitable for nanoliter-scale biological samples. The technique described in this thesis can be applied to a DSC device. The closed fluidic system will prevent sample evaporation and provide easy sample handling. The small device heat capacity will greatly help to reduce the amount of sample needed for each measurement and measurement time.

Potential technical difficulties may lie in the thermal stability of the device because the chamber needs be heated up to ~100ºC with pressure applied to it. Parylene N can replace Parylene C for better thermal stability.

5.2.2 Calorimeter Array

In principle, all the chip calorimeters can be built as arrays to give high-throughput measurement, however, not many of the chip calorimeters are actually built as calorimeter arrays [6, 7]. These calorimeters use micropipettes and inkjets to dispense samples. Therefore, many dispensing units are required for different samples and the sample will be wasted in the dispensing unit. Our microfluidic chip calorimeter does not require separate dispensing unit and the PDMS microfluidic system can be used for the preparation of the sample; samples can be diluted or mixed with other samples on chip.

Multiplexing the measurement will require the design of microfluidic and electric circuits to support multiple calorimeters and developing automated microfluidic sample handling.

5.2.3 Cell on Chips

El-Ali et al. [8] described a lab-on-a-chip device capable of cell-based assay covering all the steps from cell culture, through treatment and selection, to biochemical analysis. Calorimetric sensors can play important role in this picture. It can be used in the treatment stage to see the real-time change of the metabolism or used for selecting cells with different metabolic rates. Because the measurement is nondestructive, cells are still in good shape for further analysis. We can also integrate chip calorimeters with other sensors, such as an oxygen sensor, to provide complete analysis of the specific metabolic rate [9].

References

1. Bruylants, G., J. Wouters, and C. Michaux, *Differential scanning calorimetry in life science: Thermodynamics, stability, molecular recognition and application in drug design.* Current Medicinal Chemistry, 2005. **12**(17): p. 2011-2020.
2. Freire, E., *Differential scanning calorimetry.* Methods Mol Biol, 1995. **40**: p. 191-218.
3. Zhang, S., et al., *Nanoscale calorimetry using a suspended bridge configuration.* Journal of Microelectromechanical Systems, 2007. **16**(4): p. 861-871.
4. Olson, E.A., et al., *Scanning calorimeter for nanoliter-scale liquid samples.* Applied Physics Letters, 2000. **77**(17): p. 2671-2673.
5. Garden, J.L., E. Chateau, and J. Chaussy, *Highly sensitive ac nanocalorimeter for microliter-scale liquids or biological samples.* Applied Physics Letters, 2004. **84**(18): p. 3597-3599.
6. Torres, F.E., et al., *Enthalpy arrays.* Proceedings of the National Academy of Sciences of the United States of America, 2004. **101**(26): p. 9517-9522.
7. Verhaegen, K., et al., *A high-throughput silicon microphysiometer.* Sensors and Actuators A-Physical, 2000. **82**(1-3): p. 186-190.
8. El-Ali, J., P.K. Sorger, and K.F. Jensen, *Cells on chips.* Nature, 2006. **442**(7101): p. 403-411.
9. Kemp, R.B., *Studies of enthalpy balance and adenosine-triphosphate turnover in cultured animal cells.* Pure and Applied Chemistry, 1994. **66**(3): p. 479-484.